

AN ABSTRACT OF THE THESIS OF

Zachary D. Colton for the degree of Master of Science in Material Science presented on June 12, 2018.

Title: Development of Temperature Stable Dielectric Materials Based on Lead Bismuth Perovskite Solid Solutions.

Abstract approved:

David P. Cann

High energy density ceramic capacitors with temperature stable permittivity across -150°C to 300°C are desired for a wide variety of electronic devices. Traditional dielectrics such as barium titanate provide a high permittivity but that permittivity is strongly temperature dependent over this specified temperature range. The goal of this work is to create a perovskite material that has a high levels of B site cation disorder to take advantage of a relaxor dielectric mechanism that helps realize temperature stable dielectric properties. Perovskite ceramic solid solutions were synthesized from oxide and carbonate precursors and calcined in air at temperatures ranging from 900 to 1050°C and sintered in air at temperatures ranging from 1050 to 1200°C. Initial results focus on the $\text{BaTiO}_3\text{-Bi}(\text{Zn}_{1/2}\text{Ti}_{1/2})\text{O}_3\text{-La}(\text{Mg}_{1/2}\text{Ti}_{1/2})\text{O}_3$ ternary system and show a minimal temperature dependence with a temperature coefficient of permittivity ($\text{TC}\epsilon$) as low as -136.5 ppm/°C. However, the low permittivity values for these compounds motivated the inclusion of $\text{Pb}(\text{Ni}_{1/3}\text{Nb}_{2/3})\text{O}_3$, a perovskite with high relative permittivity and a low temperature of maximum permittivity (T_{max}). The phase structure and dielectric properties of compositions based on the compound $\text{BaTiO}_3\text{-Bi}(\text{Zn}_{1/2}\text{Ti}_{1/2})\text{O}_3$

along with additives $\text{La}(\text{Zn}_{1/2}\text{Ti}_{1/2})\text{O}_3$ and $\text{Pb}(\text{Ni}_{1/3}\text{Nb}_{2/3})\text{O}_3$ were investigated by X-ray diffraction and dielectric measurements. Results of this quaternary system show a sufficient maximum permittivity but a large $\text{TC}\epsilon=1417 \text{ ppm}/^\circ\text{C}$. Future work involves compositional modifications aimed at increasing the relative permittivity while optimizing compositional end members that enable the $\text{TC}\epsilon$ to be near zero.

©Copyright by Zachary D. Colton
June 12, 2018
All Rights Reserved

Development of Temperature Stable Dielectric Materials Based on Lead Bismuth
Perovskite Solid Solutions

by
Zachary D. Colton

A THESIS

submitted to

Oregon State University

in partial fulfillment of
the requirements for the
degree of

Master of Science

Presented June 12, 2018
Commencement June 2018

Master of Science thesis of Zachary D. Colton presented on June 12, 2018

APPROVED:

Major Professor, representing Materials Science

Director of the Materials Science Program

Dean of the Graduate School

I understand that my thesis will become part of the permanent collection of Oregon State University libraries. My signature below authorizes release of my thesis to any reader upon request.

Zachary D. Colton, Author

ACKNOWLEDGEMENTS

I would like to thank my major Professor Dr. David Cann for his incredible patience and support throughout my entire Master of Science. Dr. Cann's acknowledgement and willingness to work around my emotional and health issues is a major reason I am able to defend this research today. I would also like to thank my graduate committee Dr. Brady Gibbons, Dr. Liney Arnadottir, Dr. Laurence Schimleck, and Dr. Michelle Dolgos for their insightful comments and questions throughout my time at Oregon State.

To my friends and lab mates, your constant encouragement and comradery has helped me along my entire journey. The bonds we have made make my time at Oregon State invaluable and I hope to always maintain our friendships throughout the rest of our lives.

Finally, I would like to thank my family. My Mom and Dad for always showing their love and support, your weekly phone calls and care packages always left me feeling loved and cared for. To my sister and brother, you inspire me to take risks and to never let the preconceived judgement of others dictate the path I take in life.

Funding for this work was provided by TRS Technologies, Inc.

TABLE OF CONTENTS

	<u>Page</u>
1. Introduction	1
2. Literature Review.....	3
2.1 Capacitors	3
2.2 Perovskites	4
2.3 Ferroelectricity	6
2.4 Dielectric Properties	8
2.5 Temperature of Maximum Permittivity.....	10
2.6 Temperature Coefficient of Capacitance	10
2.7 X-ray Diffraction.....	13
2.8 Polarization Mechanisms.....	16
2.9 Relaxors	19
2.10 Competitive Materials	23
2.11 Research Objective.....	24
3. Materials and Methods.....	25
3.1 Synthesis of $BaTiO_3 - BiZn_{12}Ti_{12}O_3 - ABO_3$ Compositions	25
3.2 Synthesis of $PbNi_{13}Nb_{23}O_3$ Based Compositions	27
3.3 Electronic Characterization.....	29
3.4 Physical Characterization.....	30
4. Results	34
4.1 $BaTiO_3 - BiZn_{12}Ti_{12}O_3 - SrTiO_3$ System	35
4.2 $BaTiO_3 - BiZn_{12}Ti_{12}O_3 - LaMg_{12}Ti_{12}O_3$ System.....	38
4.3 $BaTiO_3 - BiZn_{12}Ti_{12}O_3 - LaZn_{12}Ti_{12}O_3 - PbNi_{13}Nb_{23}O_3$	44
4.3.1 30% PNN System	45
4.3.2 25% PNN System	51
4.3.3 20% PNN System	61
4.6 $BaTiO_3 - BiZn_{12}Ti_{12}O_3 - LaZn_{12}Ti_{12}O_3 - SrTiO_3$	84
5. Discussion.....	89
6. Future Work.....	94

TABLE OF CONTENTS (Continued)

	<u>Page</u>
Works Cited.....	96
Appendix A.....	99

LIST OF FIGURES

<u>Figure</u>	<u>Page</u>
1: The ABX_3 perovskite structure.	5
2: Hysteresis loop of a typical ferroelectric	7
3: Dielectric loss and its effect on P vs E loops	9
4: Temperature coefficient of capacitance vs permittivity.....	12
5: Capacitance vs Temperature plot for a ferroelectric material.....	13
6: Derivation of Bragg's law	14
7: The diffraction pattern for a cubic composition.	16
8: The relative permittivity and its dependence on frequency	18
9: Oppositely oriented 180° and 90° domain structures	19
10: Temperature vs Permittivity of PMN	20
11: Relationship between the tolerance factor and diffuseness parameter in $BT - BZT - ABO_3$ compositions	23
12: The ternary diagram for BT-BZT-ST compositions.....	35
13: X-ray diffraction data for the compositions in the BT-BZT-ST system.....	36
14: (a) Relative permittivity and (b) dielectric loss versus high temperature of 25BT-50BZT-25ST	37
15: (a) The relative permittivity and (b) dielectric loss versus temperature for 50BT-25BZT-25ST	37
16: Ternary compositions characterized within the BT-BZT-LMT system.	38
17: X-ray diffraction data shows single phase perovskite structure for 25BT-25BZT-50LMT and 50BT-25BZT-25LMT compositions.....	39
18: (a) The relative permittivity versus temperature and (b) dielectric loss vs temperature for 25BT-25BZT-50LMT	40
19: (a) Relative permittivity and (b) dielectric loss versus low temperature of 25BT-25BZT-50LMT	40
20: Polarization versus electric field measurement of 25BT-25BZT-50LMT.....	41

LIST OF FIGURES (Continued)

<u>Figure</u>	<u>Page</u>
21: (a) Relative permittivity and (b) dielectric loss versus high temperature of 50BT-25BZT-25LMT shows a low $TC\epsilon$ and low $\tan\delta$ at low frequencies.	42
22: (a) Low temperature relative permittivity and (b) dielectric loss versus temperature of 50BT-25BZT-25LMT	42
23: Polarization versus electric field measurement 50BT-25BZT-25LMT	43
24: Ternary diagram for compositions within the BT-BZT-LZT-PNN system with 30% PNN.	44
25: X-ray diffraction data for the BT-BZT-LZT-PNN system	45
26: (a) Relative permittivity measurements of 45BT-20BZT-5LZT-30PNN.....	46
27: (a) The relative permittivity and (b) dielectric loss show a hysteresis and and large $TC\epsilon$ for the 45BT-22BZT-3LZT-30PNN composition.	47
28: (a) Low temperature measurements for 45BT-22BZT-3LZT-30PNN	47
29: (a) Relative permittivity versus high temperature of 45BT-24BZT-1LZT-30PNN	48
30: (a) Low temperature permittivity versus temperature measurements of 45BT-24BZT-1LZT-30PNN.	48
31: Polarization versus electric field measurements confirm that 45BT-24BZT-1LZT-30PNN is a viable linear dielectric relaxor.	49
32: (a) Relative permittivity and (b) dielectric loss versus temperature measurements for 45BT-24BZT-1LZT-30PNN with 3% extra La.....	50
33: Polarization versus electric field measurements of 45BT-24BZT-1LZT-30PNN with extra La.....	50
34 X-ray diffraction data for compositions containing 25% PNN	51
35: (a) While the 50BT-15BZT-10LZT-25PNN composition has a low $TC\epsilon$ the maximum relative permittivity is reduced as well. (b) dielectric loss versus temperature shows large increases in the loss at temperatures above 150°C.	52
36: The low temperature measurements for the (a) relative permittivity and (b) dielectric loss of 50BT-15BZT-10LZT-25PNN.....	52

LIST OF FIGURES (Continued)

<u>Figure</u>	<u>Page</u>
37: Polarization versus electric field measurements of 50BT-15BZT-10LZT-25PNN	53
38: (a) Relative permittivity and (b) dielectric loss versus temperature for 50BT- 20BZT-5LZT-25PNN at high temperatures.....	54
39: (a) Low temperature relative permittivity and (b) dielectric loss measurements of 50BT-20BZT-5LZT-25PNN.....	54
40: Polarization versus electric field measurements of 50BT-20BZT-5LZT-25PNN show a linear dielectric response.....	55
41: (a) Relative permittivity versus high temperature measurements of 50BT-24BZT- 1LZT-25PNN	56
42: Low temperature (a) relative permittivity measurements of 50BT-24BZT-1LZT- 25PNN.....	56
43: Polarization versus electric field measurements of 50BT-23BZT-3LZT-25PNN.....	57
44: (a) Relative permittivity versus temperature and (b) dielectric loss versus temperature of 50BT-24BZT-1LZT-25PNN	57
45: Low temperature permittivity and (b) dielectric loss measurements of 50BT- 24BZT-1LZT-25PNN.....	58
46: The polarization versus electric field measurement shows 50BT-24BZT-1LZT- 25PNN has a linear dielectric response.	58
47: (a) Relative permittivity and (b) dielectric loss versus temperature of 50BT- 24BZT-1LZT-25PNN.....	59
48: Low temperature measurements for (a) relative permittivity and (b) dielectric loss of 50BT-24BZT-1LZT-25PNN.....	59
49: Polarization versus electric field measurements of 50BT-24BZT-1LZT-25PNN	60
50: X-ray diffraction data for compositions containing 20% PNN.....	61
51: The high temperature (a) permittivity and (b) dielectric loss measurements of 53BT-20BZT-7LZT-20PNN.....	62
52: The (a) relative permittivity versus temperature measurement of 53BT-20BZT- 7LZT-20PNN.	62

LIST OF FIGURES (Continued)

<u>Figure</u>	<u>Page</u>
53: Polarization versus electric field measurements of 53BT-20BZT-7LZT-20PNN confirm a linear dielectric response.....	63
54: High temperature measurements of 55BT-20BZT-5LZT-20PNN.....	63
55: Low temperature measurements of 55BT-20BZT-5LZT-20PNN.....	64
56: Polarization versus electric field measurements of 55BT-20BZT-5LZT-20PNN.....	64
57: X-ray diffraction data for the PT-PNN-BZT-NN.....	66
58: (a) Relative permittivity and (b) dielectric loss versus temperature plots of 40PT-50PNN-5BZT-5NN	68
59: Low temperature data confirms of the 40PT-50PNN-1BZT-9NN.....	68
60: The polarization versus electric field measurement 40PT-50PNN-1BZT-9NN ...	69
61: The (a) relative permittivity versus temperature data of 40PT-50PNN-5BZT-5NN	69
62: Low temperature measurements of 40PT-50PNN-5BZT-5NN	70
63: Polarization versus electric field measurements of 40PT-50PNN-5BZT-5NN show another ferroelectric response.	70
64: (a) Relative permittivity and (b) dielectric loss plots of 40PT-50PNN-9BZT-1NN.	71
65: (a) Low temperature permittivity measurements of 40PT-50PNN-9BZT-1NN ...	71
66: The polarization versus electric field measurement of 40PT-50PNN-9BZT-1NN confirms this material is a ferroelectric.	72
67: (a) Relative permittivity and (b) dielectric loss plots for 45PT-45PNN-1BZT-9NN from 25 – 300°C.....	73
68: (a) Low temperature permittivity and (b) dielectric loss for 45PT-45PNN-1BZT-9NN.....	73
69: Polarization versus electric field measurement of 45PT-45PNN-1BZT-9NN.....	74
70: (a) The relative permittivity and (b) dielectric loss of 45PT-45PNN-5BZT-5NN.....	74
71: The polarization versus electric field measurements of 45PT-45PNN-5BZT-5NN	75

LIST OF FIGURES (Continued)

<u>Figure</u>	<u>Page</u>
72: (a) Relative permittivity and (b) dielectric loss of 45PT-45PNN-9BZT-1NN from 25 – 300°C.	75
73: The polarization versus electric field measurement of 45PT-45PNN-9BZT-1NN shows a deteriorated ferroelectric hysteresis loop.	76
74: X-ray diffraction data for the PT-PNN-NN system shows some slight peak splitting on the (100) and (200) planes.	77
75: (a) Relative permittivity and (b) dielectric loss of 15PT-25PNN-60NN	78
76: (a) The low temperature permittivity data of 15PT-25PNN-60NN	78
77: Polarization versus electric field data of 15PT-25PNN-60NN	79
78: (a) The relative permittivity and dielectric loss of 20PT-30PNN-50NN.....	80
79: (a) Low temperature relative permittivity and (b) dielectric loss of 20PT-30PNN-50NN.....	80
80: The polarization versus electric field of 20PT-30PNN-50NN.....	81
81: (a) Relative permittivity and (b) dielectric loss measurements of 25PT-25PNN-50NN shows undesirable levels across nearly all temperatures.....	82
82: (a) Low temperature relative permittivity measurements of 25PT-25PNN-50NN	82
83: Polarization versus electric field measurement of 25PT-25PNN-50NN	83
84: The X-ray diffraction data shows the perovskite structure with a minor additional peak around 30°	84
85: (a) High temperature relative permittivity measurements of 50BT-25BZT-10LZT-15ST	85
86: (a) The low temperature permittivity measurements of 50BT-25BZT-10LZT-15ST.....	85
87: Polarization versus electric field measurements of 50BT-25BZT-10LZT-15ST show a linear dielectric that can withstand an electric field up to 40kV/cm.	86
88: (a) The relative permittivity of 50BT-25BZT-15LZT-10ST	87

LIST OF FIGURES (Continued)

<u>Figure</u>	<u>Page</u>
89: (a) The low temperature permittivity measurement of 50BT-25BZT-15LZT-10ST	87
90: Polarization versus electric field for 50BT-25BZT-15LZT-10ST.	88
91: The relationship between the tolerance factor and $TC\epsilon$ for BT-BZT-LZT-ABO3 compositions.....	92

LIST OF TABLES

<u>Table</u>	<u>Page</u>
1: Precursor, purity, and supplier for compositions synthesized in this work.	28
2: Physical properties of the perovskite materials in the BT-BZT-LMT system.....	39
3: Dielectric properties for the BT-BZT-LMT system.	43
4: Physical characteristics of compositions within the BT-BZT-LZT-PNN system...	46
5: Dielectric properties of the BT-BZT-LZT-PNN system.....	65
6: Physical property measurements of the PT-PNN-BZT-NN system.	66
7: Dielectric properties of the PT-PNN-BZT-NN system.	76
8: Physical properties of the PT-PNN-NN sytem.....	77
9: Dielectric properties of the PT-PNN-NN system.....	83
10: The physical properties of the BT-BZT-LZT-ST system.	84

1. Introduction

Ceramic capacitors with a low temperature dependency are needed in automotive, aviation and weapon systems that can operate under extreme high and low temperature applications. The operating temperature of a circuit plays an important factor when selecting capacitors as it can cause a large effect on the function and performance of the device regardless of application. Proper selection of the dielectric material for a specific operating temperature is important because higher temperatures can cause a decrease in capacitance as the dielectric passes the Curie temperature.

The Curie temperature is the temperature where a ferroelectric material makes a phase transition and is associated with a sharp and narrow peak in the relative permittivity. Material composition modifications can tune the Curie temperature to occur at a specific temperature. However, when an electronic device needs to operate over a wide temperature range relaxor materials are typically employed due to the diffuseness of the permittivity peak. Relaxors contain polar nano-regions below their transition temperature which are regions of randomly distributed dipole moments. While the cause of the formation of polar nano-regions is not fully understood, their contribution to the dispersion of the relative permittivity with respect to temperature is imperative to this research.

The objective of this work is to synthesize relaxor dielectric materials with a relative permittivity above 1000, a temperature coefficient of permittivity close to $0^\circ\text{C}/\text{ppm}$, low dielectric loss, a maximum permittivity below 0°C and a high dielectric strength.

The lead free compositions $\text{BaTiO}_3 - \text{Bi}\left(\text{Zn}_{\frac{1}{2}}\text{Ti}_{\frac{1}{2}}\right)\text{O}_3 - \text{La}\left(\text{Mg}_{\frac{1}{2}}\text{Ti}_{\frac{1}{2}}\right)\text{O}_3$, $\text{BaTiO}_3 - \text{Bi}\left(\text{Zn}_{\frac{1}{2}}\text{Ti}_{\frac{1}{2}}\right)\text{O}_3 -$

$SrTiO_3$, and $BaTiO_3 - Bi\left(\frac{Zn_1}{2}Ti_{\frac{1}{2}}\right)O_3 - La\left(\frac{Zn_1}{2}Ti_{\frac{1}{2}}\right)O_3 - SrTiO_3$ are created through solid state synthesis techniques and characterize their dielectric properties with respect to temperature. Lead based compositions $BaTiO_3 - Bi\left(\frac{Zn_1}{2}Ti_{\frac{1}{2}}\right)O_3 - La\left(\frac{Zn_1}{2}Ti_{\frac{1}{2}}\right)O_3 - Pb\left(\frac{Ni_1}{3}Nb_{\frac{2}{3}}\right)O_3$, $PbTiO_3 - Pb\left(\frac{Ni_1}{3}Nb_{\frac{2}{3}}\right)O_3 - NaNbO_3$, and $PbTiO_3 - Pb\left(\frac{Ni_1}{3}Nb_{\frac{2}{3}}\right)O_3 - Bi\left(\frac{Zn_1}{2}Ti_{\frac{1}{2}}\right)O_3 - NaNbO_3$ are also synthesized this time using the columbite precursor method to avoid pyrochlore impurities.

After characterization is complete the lead free compositions within the $BaTiO_3 - Bi\left(\frac{Zn_1}{2}Ti_{\frac{1}{2}}\right)O_3 - La\left(\frac{Zn_1}{2}Ti_{\frac{1}{2}}\right)O_3 - SrTiO_3$ family were found to have the best combination of electronic properties and future work should be aimed at further exploring this quaternary system.

2. Literature Review

2.1 Capacitors

The capacitor is a device made of a dielectric material that is used to store electrical charge. Each capacitor is made up of an insulating material of uniform thickness surrounded by two electrode plates that easily conduct current. When voltage is applied across the capacitor the dielectric material is polarized causing one electrode to be positively charged and the other negatively charged [1]. The equation used to calculate the capacitance of a material is presented in equation 1 [1].

$$C = \epsilon_r \epsilon_0 \frac{A}{h} \quad (1)$$

Where ϵ_r is the relative permittivity of the dielectric (unit-less), ϵ_0 is the permittivity of a vacuum ($8.85 * 10^{-12} F/m$), A is the area of the capacitor (m^2), and h is the distance between the electrode plates (m). The SI unit of capacitance is known as the farad which originates from the physicist Michael Faraday. One farad is equivalent to a one coulomb charge across an electric potential difference of one volt [1]. Achieving one farad on a regular one-millimeter capacitor requires either a very high permittivity dielectric, or an extremely large surface area. Typically, capacitance is reported in nano-farads or pico-farads.

A capacitor can fulfill various functions within a circuit but is primarily used to store a fixed amount of static electricity. It can also serve as a mechanism to separate alternating current (AC) and direct current (DC) as it blocks the path of DC but allows AC to flow through [1]. Direct current is a constant directional stream of electrons which create an electric current, while AC is a flow of charge that will periodically

change directions defined by the frequency f (Hz). As a DC bias is applied to a capacitor, charge starts to accumulate over time. The time it takes to fully charge a capacitor depends on the resistance within the circuit and the total capacitance of the capacitor [1].

Another important parameter that helps improve capacitor performance is the volumetric efficiency. Volumetric efficiency is what allows device miniaturization as it is directly proportional to the relative permittivity of the capacitor [2]. The volumetric efficiency is simply the capacitance divided by the volume as seen in equation 2 .

$$\frac{C}{V} = \frac{\epsilon_r \epsilon_0}{h^2} \quad (2)$$

where V is the volume of the capacitor and h is the separation between electrodes [2].

2.2 Perovskites

A perovskite is a primitive cubic crystal structure with the form ABO_3 where the A site is located at the body center $(\frac{1}{2}, \frac{1}{2}, \frac{1}{2})$ and is in twelve-fold coordination. While the B site is located at the structure corners $(0, 0, 0)$ and is in six-fold coordination [4]. The perovskite is an interesting structure because it provides materials with a wide array of desirable properties that can be tweaked by changing either distorting the structure or manipulating the composition. Materials such as $BaTiO_3$, which was the first ceramic material where ferroelectricity was observed, to $Pb(Zr_{1-x}Ti_x)O_3$, which is a widely utilized piezoelectric ceramic material, to superconductors like $(Y_{\frac{1}{3}}Ba_{\frac{2}{3}})CuO_{3-x}$, all share the perovskite structure which lends them their unique properties [5].

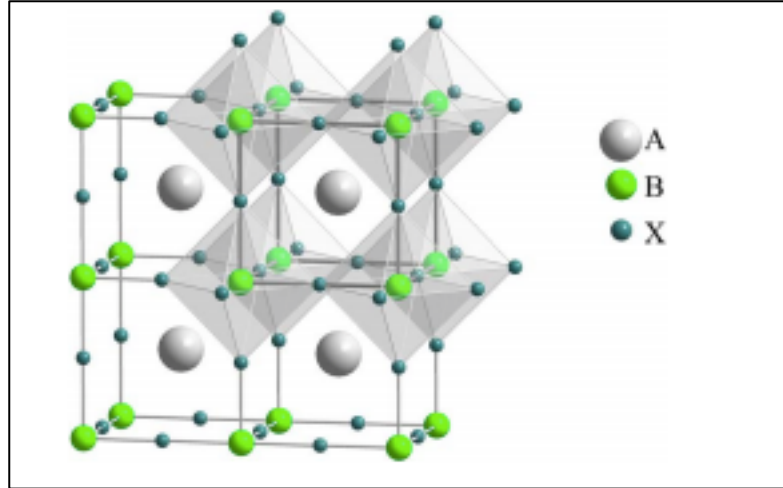


Figure 1: The ABX_3 perovskite structure where the A site is a cation selected to neutralize charge, the B site is a metal cation and X is the anion [6].

Structural distortions often occur within the perovskite structure due to the A site or B site atom not fitting perfectly in the lattice site generated. To determine how well an atom fits within each site the tolerance factor (t) is used to quantify the level of distortion in the structure from an ideal cubic perovskite [5]. The equation for the tolerance factor is found in equation 3 below

$$t = \frac{R_A + R_O}{\sqrt{2}(R_B + R_O)} \quad (3)$$

where R_A , R_B are the ionic radii of the A and B site cations and R_O is the ionic radii of the oxygen ion [7]. The tolerance factor can then be used to determine if the structure can remain cubic. If t is close to $t \sim 1.0$, the structure retains cubic symmetry. With $t > 1$ the octahedral space surrounding the B site of the structure is larger than is required for the B cation and so the structure distorts into tetragonal symmetry which is the case with barium titanate where $t = 1.06$ [5]. Hexagonal distortions are also possible for perovskites with $t > 1$. If the tolerance factor varies significantly from 1, the structure will distort beyond the capacity of the perovskite structure and the

coordination number of each atom must change into a new crystal structure. This is the case for $MgTiO_3$ which has a $t = 0.81$ causing the material to adopt the ilmenite structure [7].

2.3 Ferroelectricity

Ferroelectric materials are dielectrics that have large permittivity values and may retain some polarization after the electric field is removed. As the electric potential on a ferroelectric is increased it will eventually reach a maximum polarizability known as the saturation polarization (P_s) [4]. Figure 2 shows that as the electric potential is reduced to zero after reaching P_s , some polarization remains in the material and is called the remanent polarization P_R . To remove the remanent polarization, a reverse electric potential must be applied to reduce the overall polarization in the material. The value of the electric field required to reduce the polarization to zero is known as the coercive field (E_c) [4]. The non-linear process by which ferroelectrics polarize and depolarize is known as a hysteresis loop which is found in Figure 2 below.

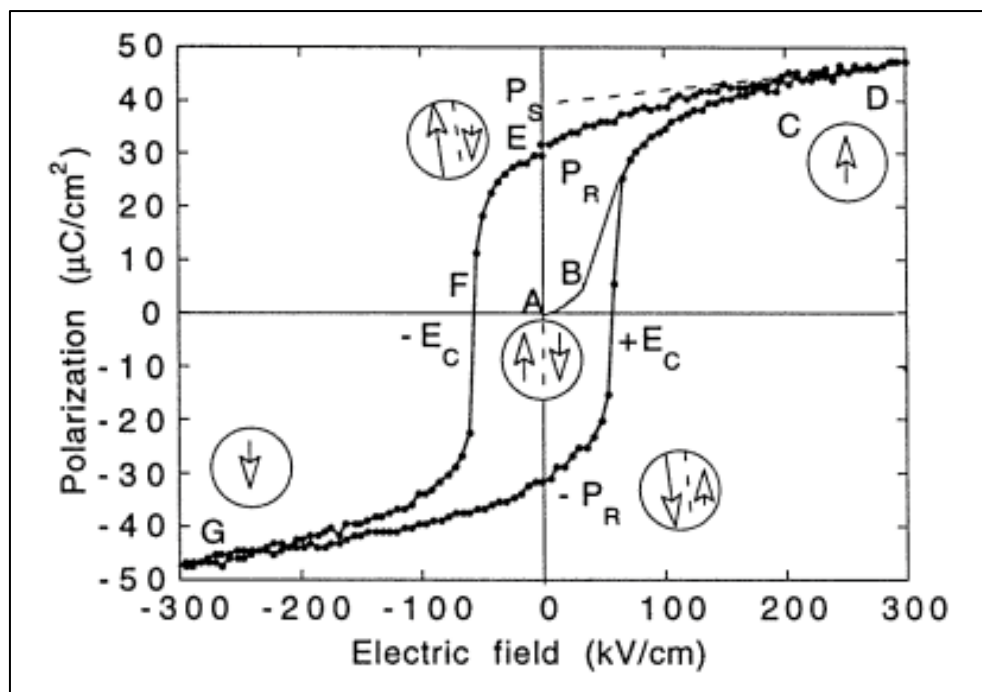


Figure 2: Hysteresis loop of a typical ferroelectric that has remanent polarization when after an electric field is applied and then reduced back to zero. The polarization can be reduced to zero by applying a coercive electric field in the reverse direction [8].

When the ferroelectric material is under an electric field it causes the cation on the B site to displace within its octahedron. This charge displacement is on the order of 0.1 \AA but it is what causes an increase in the number of dipoles within the material which causes an increase in the permittivity.

The structure of the material can be a determining factor whether or not the material behaves like a ferroelectric or a dielectric. Barium titanate, which exists in a cubic structure above 123°C [9], has no net dipole moment due to the charge being centered within the TiO_6 octahedron. When cooled below 123°C the structure becomes tetragonal which allows for a dipole moment within each octahedron and spontaneous

polarization can occur due to the offset *Ti* atom. When an electric field is applied to *BaTiO₃* in its ferroelectric form it causes all of the dipoles to align until the saturation polarization is reached [4].

2.4 Dielectric Properties

The dielectric constant (κ) otherwise known as the relative permittivity (ϵ_r) is a ratio of the permittivity of a material over the permittivity of free space shown in equation 4.

$$\kappa = \epsilon_r = \frac{\epsilon_{ij}}{\epsilon_0} \quad (4)$$

There is also the complex relative permittivity which is a quantity with a real and imaginary part that describes the energy storage and loss of a material [10]. The complex relative permittivity is seen in equation 5 below

$$\epsilon_r^* = \epsilon_r' - i\epsilon_r'' \quad (5)$$

where ϵ_r' is the real part of the relative permittivity and $i\epsilon_r''$ is the dielectric loss. The real part of the complex permittivity (ϵ_r') is attributed to how much electrical energy storage occurs when molecules align with an electrical field. The imaginary part is known as the dielectric loss which is the loss of energy due to conduction losses and heat [10]. The dielectric loss is often given in terms of $\tan \delta$ which is a ratio of the imaginary permittivity over the real permittivity shown in equation 6.

$$\tan \delta = \frac{\epsilon_r''}{\epsilon_r'} \quad (6)$$

Dielectric loss is a frequency dependent property. As molecules try to align with a changing electric field at some point they can no longer keep up, the molecules then

relax and energy is released as heat [10]. Figure 3 also shows why low loss capacitors are needed in electrical circuits.

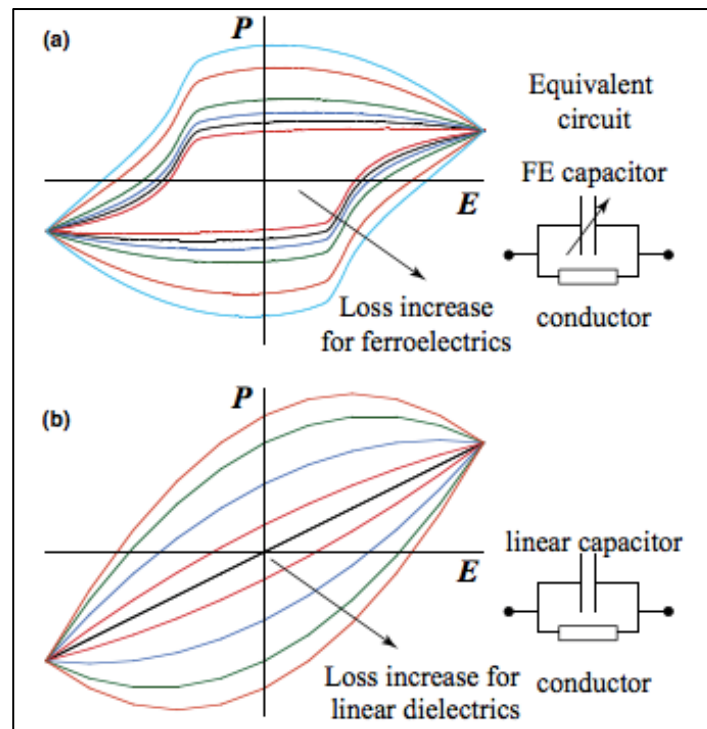


Figure 3: Dielectric loss and its effect on P vs E loops. (a) Ferroelectric sample with increasing conductivity shows a deterioration of the hysteresis loops (b) Linear capacitor also shows deterioration of P vs E with increased conductivity. Low loss capacitors are desired so that the remanent polarization and coercive field remain constant throughout the devices lifetime [11].

As conductivity increases in the capacitor there is an increase in the dielectric loss which causes the polarization vs electric field loops to round and shift P_R and E_C values [11]. This can cause issues with device reliability and heat management especially when temperature stability is a concern.

2.5 Temperature of Maximum Permittivity

The temperature of maximum permittivity (T_m or T_{max}) is known as the Curie temperature (T_c) for traditional ferroelectrics. This is the peak in the real part of the permittivity that occurs when a material like barium titanate makes a phase change from cubic to tetragonal with decreasing temperature. The distortion in the perovskite structure that occurs with this phase change is what allows the Ti^{4+} atoms to displace within their octahedra and cause an increase in the number of polarizable dipoles in the lattice. While relaxors can also have a Curie temperature, the diffuseness of its phase transition over a large temperature range can make it difficult to establish a single temperature at which it occurs. For this reason, the temperature of maximum permittivity is used in place of the Curie temperature which is frequency dependent as seen in figure 10.

2.6 Temperature Coefficient of Capacitance

Dielectrics with small temperature coefficient of permittivity (TC_ϵ) and high permittivity (ϵ_r) are sought after to improve the volumetric efficiency of capacitors. The temperature coefficient of permittivity can be derived by differentiating the Clausius-Mosotti equation with respect to temperature. The Clausius-Mosotti equation found in equation 7 below is derived based on the assumption that the permittivity of a material is caused by the polarizability of the constituent atoms or molecules [3].

$$\frac{\epsilon_r - 1}{\epsilon_r + 2} = \frac{N\alpha}{3\epsilon_0} \quad (7)$$

where N is the number of atoms or molecules per \AA^3 , ϵ_r is the relative permittivity, α is the polarizability and ϵ_0 is the permittivity of free space. Differentiation of the

Clausius-Mosotti equation gives the temperature coefficient of capacitance and highlights the components of material design that influence the TCC. As the temperature increases and the overall material volume increases there is a decrease in the number of polarizable ions and electrons per unit volume [3]. The linear expansion coefficient combined with the change in polarizability of the dielectric with temperature are the two main sources of variation in the TCC [12].

$$TCC = \frac{1}{C} \left(\frac{\partial C}{\partial T} \right) = \frac{(\epsilon-1)(\epsilon+2)}{\epsilon} \left(\frac{1}{3\alpha} \left(\frac{\partial \alpha}{\partial T} \right) - \alpha_l \right) + \alpha_l \quad (8)$$

where TCC is the temperature coefficient, C is the capacitance, ϵ is the permittivity, α is the polarizability, V is the volume, and α_l is the linear expansion coefficient [13]. The TCC relates to the temperature coefficient of permittivity by equation 9 [3].

$$TCC = TC_\epsilon + \alpha_L \quad (9)$$

Work by Harrop revealed how the TCC varies with each class of material. Low loss polymers which possess permittivity values around two were found to have a TCC that is negative and entirely dependent on the thermal expansion coefficient [13]. Glasses were classified into low, medium, and high permittivity categories and each category was found to have either a zero or positive TCC. The positive TCC was attributed to glass materials polarizability due to the presence of heavy deformable ions [13]. Through a separate study, paraelectrics (which are polarizable materials that return to zero polarization upon the removal of the electric field), were studied to find the temperature dependent contributions to the TCC [14]. Paraelectrics were found to have negative TCCs that could be predicted based off the equation $TCC = -\alpha_l \epsilon$ [13]. This

equation was found to match experimental data of various paraelectrics which can have TCC that range between $-200 \text{ ppm}/^\circ\text{C}$ to $-100,000 \frac{\text{ppm}}{^\circ\text{C}}$ [14].

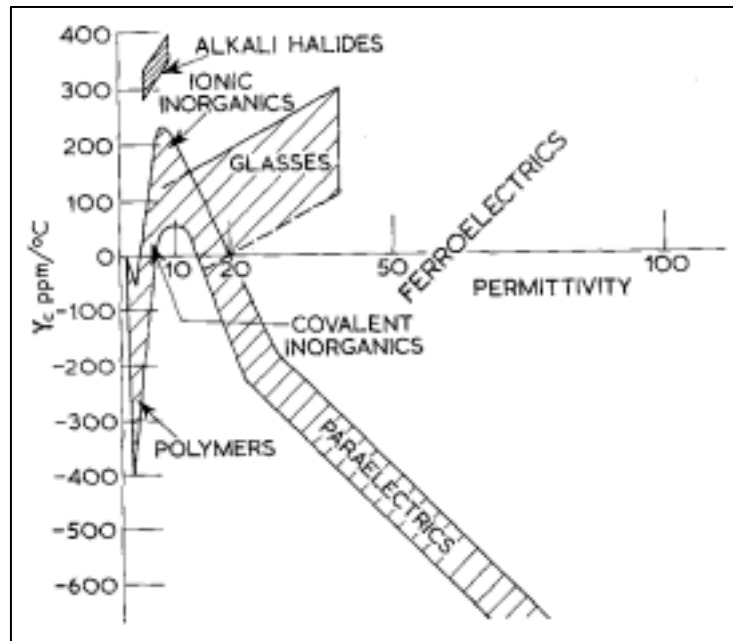


Figure 4: Temperature coefficient of capacitance vs permittivity for different classifications of materials [13].

Ferroelectrics vary their capacitance with temperature according to figure 5. As the figure shows, the TCC of ferroelectrics can be positive, negative or even zero if the material has passed through two transition temperatures [13]. This study shows that a material with high permittivity and a TCC close to zero will most likely display some form of ferroelectricity. While this study helps narrow the scope of this project, ferroelectricity can cause an increase in the dielectric loss of a material which will make it difficult to create a low loss material with a large enough permittivity and have a TCC equal to zero [13].

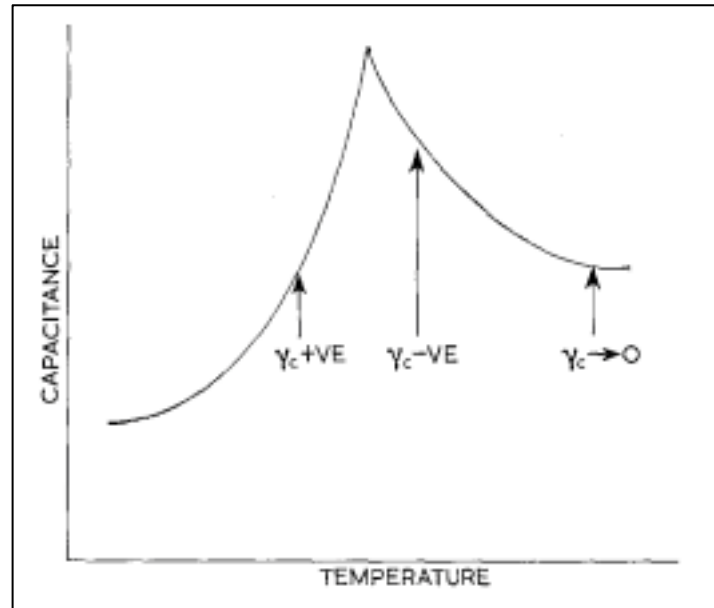


Figure 5: Capacitance vs Temperature plot for a ferroelectric material. TCC can vary from positive to negative values and can approach zero after two transition temperatures [13].

2.7 X-ray Diffraction

X-ray diffraction is a physical characterization technique that gives critical information used to determine a material's crystal structure. X-rays are generated by accelerating a charged particle (usually electrons) across an electrical potential of approximately 30 kV [4]. When the accelerated electron impacts a metal target it produces a wide spectrum of wavelengths of varying intensity referred to as white radiation along with a few wavelengths that have large peaks of intensity. When the electron impacts the Cu target (Cr, Fe, Mo, and Ag also used) and ionizes an electron from the 1s shell. As electrons drop from the 2p or 3p orbital into the 1s orbital, some of the energy is released in the form of X-rays. When electrons shift in the Cu target from the 2p to the 1s orbital, $K\alpha$ X-rays are emitted which have a wavelength of 1.5418 \AA [4]. The second monochromatic wavelength emitted is $K\beta$ which has a wavelength equal to 1.3922 \AA

and is produced when the electron from the 3p orbital shifts to the 1s orbital [4]. The $K\alpha$ radiation is most commonly used because the transition from 2p to 1s occurs more frequently which causes a greater intensity at that wavelength. After the electron impacts the Cu target and produces a spectrum of wavelengths those wavelengths are sent through a nickel filter which is able to absorb all white radiation, Cu $K\beta$ leaving only Cu $K\alpha$. Copper $K\alpha$ radiation is the most desirable because its wavelength is similar to interatomic spacing's which is around 2-3 Å [4].

As shown by Figure 6, when Cu $K\alpha$ radiation passes through a material it reflects some of the X-rays off of planes at an angle of reflection which is equal to the angle of incidence.

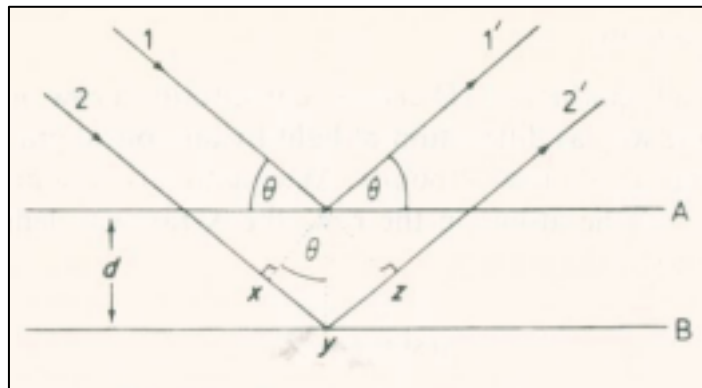


Figure 6: Derivation of Bragg's law, diffracted X-rays are measured based off of the Bragg angle and measured intensity. The d-spacing is the distance between adjacent planes and is reliant on the dimensions of the unit cell [4].

Other X-rays pass through the first plane but are later reflected by a parallel plane. The distance between adjacent planes is known as the d-spacing, and the angle of incidence is the Bragg angle θ . This gives Bragg's law which is used to interpret the diffraction pattern to find the d-spacing of a material [15].

$$n\lambda = 2d\sin\theta \quad (10)$$

Where n is an integer and λ is the radiation wavelength. The diffraction pattern can then be used to connect the patterned scattering of X-rays to individual planes and crystal structures [15].

The intensity of the reflected radiation (I) is known to be proportional to the square of the structure factor.

$$I(hkl) \propto |F(hkl)|^2 \quad (11)$$

Where $I(hkl)$ is the intensity of radiation reflected off of the plane (hkl) and $F(hkl)$ is the structure factor for plane (hkl) [15]. While the magnitude of the intensity depends on factors such as crystal size, crystal condition and thermal vibrations, the structure factor contains all of the key information to determine the atomic positions within a crystal structure [15]. The equation for the structure factor can be seen in equation 12 below.

$$F(hkl) = \sum f_j \exp 2\pi i(hx_j + ky_j + lz_j) \quad (12)$$

Where f_j is the atomic scattering factor, and h, k, l are integers known as the Miller indices [15]. The atomic scattering factor depends on the type of atom and the Bragg angle θ that the incident wave strikes the plane. The structure factor is used to tell how well a crystal structure agrees with magnitudes present in a diffraction pattern. After a diffraction pattern is generated Bragg angle of each peak of intensity is used to determine the materials structure and composition. For this project, the main use of X-ray diffraction is to check for the formation of a secondary phase which could cause an undesirable change in the material properties. The diffraction pattern for a $BaTiO_3$ –

$Bi\left(Zn_{\frac{1}{2}}Ti_{\frac{1}{2}}\right)O_3 - La\left(Zn_{\frac{1}{2}}Ti_{\frac{1}{2}}\right)O_3 - Pb\left(Ni_{\frac{1}{3}}Nb_{\frac{2}{3}}\right)O_3$ is shown in figure 7 as an example, where each peak position is determined by the size and shape of the unit cell.

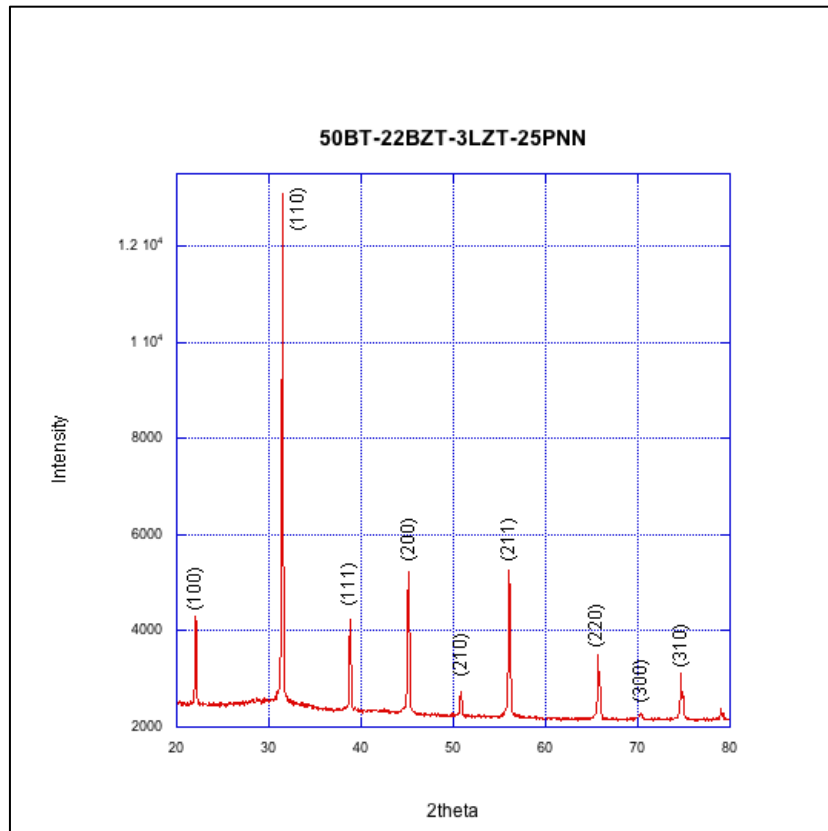


Figure 7: The diffraction pattern for a cubic composition with each peak labeled by the planes associated miller indices.

The peak positions found from a diffraction pattern are then indexed and can be used later to help determine future material crystal structures and compositions.

2.8 Polarization Mechanisms

Dielectrics have five different mechanisms through which they are polarized. The five mechanisms are split into two subgroups called intrinsic and extrinsic polarization.

Intrinsic polarization refers to polarization mechanisms which contribute through the materials lattice including the electronic polarization and ionic polarization [16]. The electronic polarization refers to how the electron cloud displaces away from the nucleus of an atom under an electric field. Ionic polarization occurs when a material that contains both cations and anions shift from their equilibrium position to form a net dipole moment under an electric field [16].

Extrinsic polarization refers to all other mechanisms which do not contribute to the polarization directly through the lattice of a material. Interface polarization, otherwise known as space charge polarization, occurs when mobile charge carriers collect around a defect in the material. This defect could be the electrode-material interface or simply a grain boundary in the material [16]. Dipolar polarization is another method of extrinsic polarization, it occurs due to molecules having permanent dipoles in polar covalent solids. The permanent dipoles which are randomly oriented align with the applied electric field [16]. The contribution to the permittivity from these extrinsic effects is one of the first to fall off with increasing frequency which is seen in figure 8 [16].

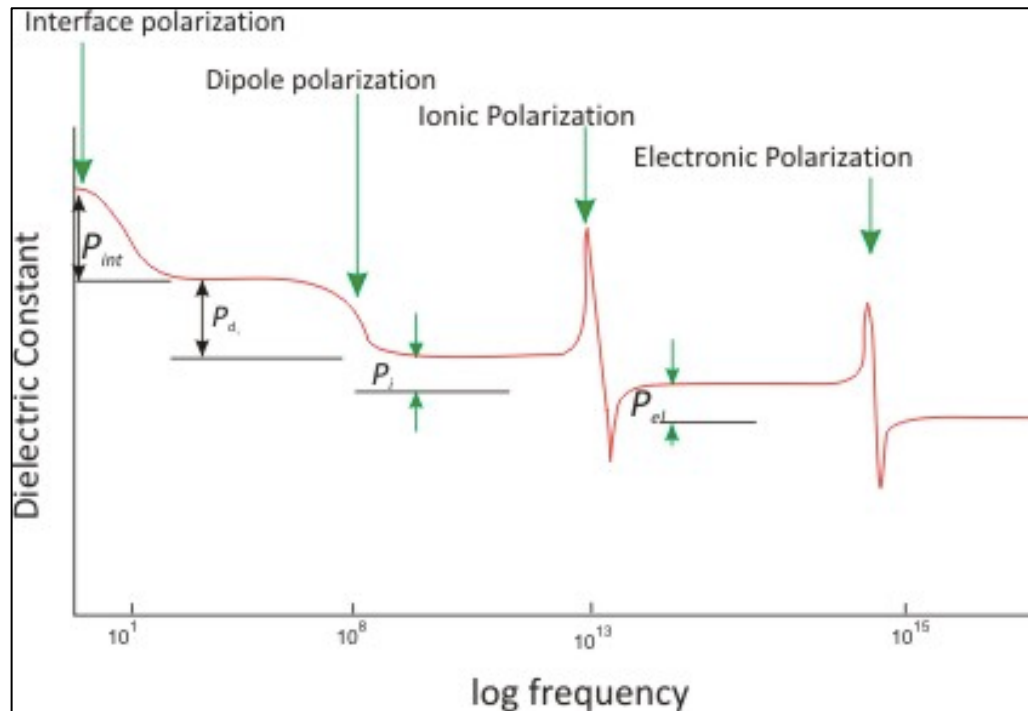


Figure 8: The relative permittivity (dielectric constant) and its dependence on frequency. The heavier each individual mechanism is makes it harder for it to keep up with a alternating electric field. Re-orienting entire molecules takes time so its contribution falls off at around $10^8 - 10^9$ Hz [17].

The last extrinsic polarization mechanism is known as domain wall polarization and is only a factor in ferroelectric materials. However, domain wall polarization can be a major contributing factor to the permittivity of a material at low electric fields [18]. Domains are regions within the ferroelectric material which contain homogenous orientation of dipoles. For tetragonal ferroelectrics, the domains can be in either 180° or 90° orientation to each other as seen in figure 9 [18].

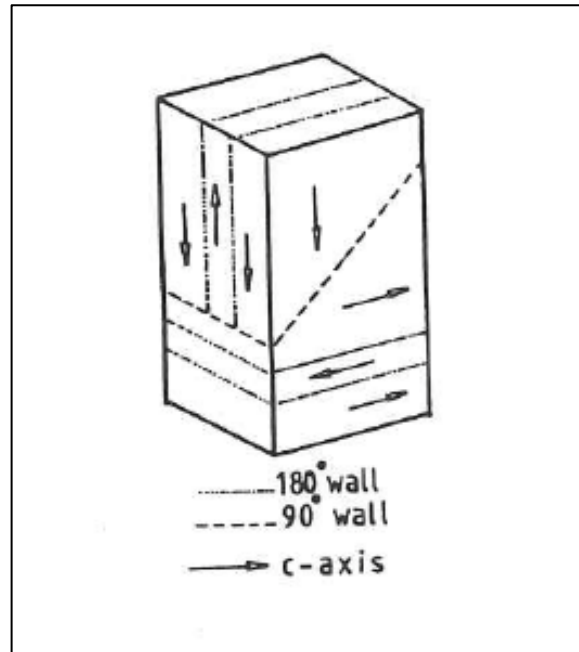


Figure 9: Oppositely oriented 180° and 90° domain structures contribute to the net polarization of a ferroelectric [18].

As an electric field is applied, it can cause the direction of polarization within a domain to change, or it can cause a domain wall migration to occur so that one domain orientation grows in size [4].

2.9 Relaxors

Relaxors are a class of disordered crystals which allow for unique structure property relationships. When these crystal structures are taken to high temperatures they reside within a non-polar paraelectric phase, while at lower temperatures they begin to form polar nanoregions (PNR) which have randomly partitioned dipole moments [19]. The temperature at which the relaxor switches from the paraelectric state to the formation of PNRs is known as the Burns temperature [19]. These polar nanoregions cause a dramatic shift in material properties which makes them desirable for further research within many disciplines. Relaxor ferroelectrics play an important part in temperature

stable dielectrics because as the temperature is further decreased well below the Burns temperature a large broad peak in the relative permittivity is observed. This peak is similar in magnitude to the peak that occurs at the Curie temperature in traditional dielectrics but its diffuseness in the temperature dependence of the relative permittivity is why it is considered to be a ferroelectric with a diffuse phase transition [19].

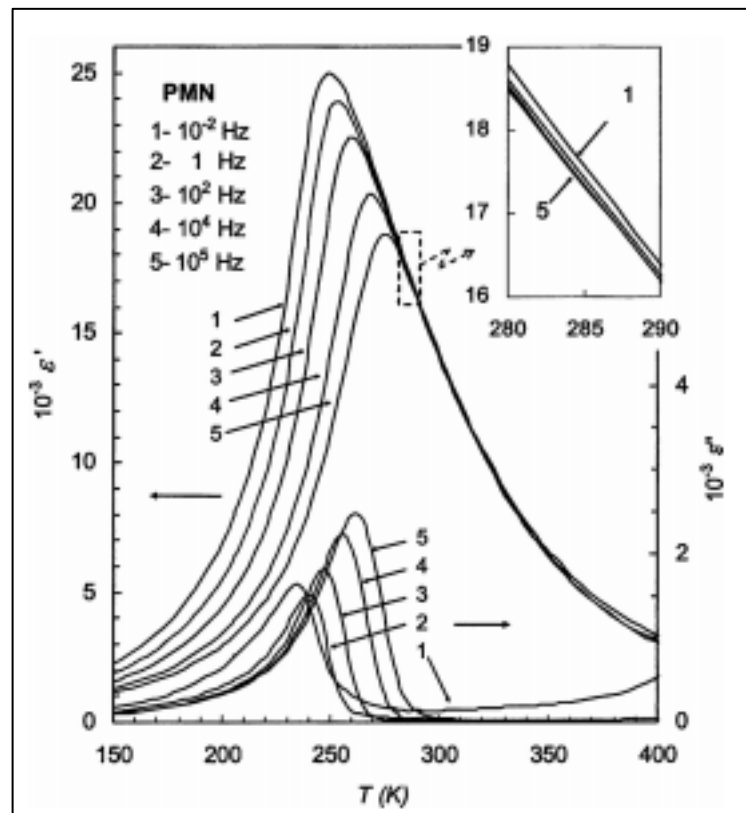


Figure 10: Temperature vs Permittivity of PMN shows the dependency of permittivity on frequency in both the real and imaginary parts after cooling below the Burns temperature at around 620 K [19, 20]

An important factor that plays into the physical properties of relaxor ferroelectrics is the compositional disorder within the crystal structure. This is where different size and valence ions are located on the same site throughout the structure. For example, in the

relaxor perovskite $Pb\left(Mg_{\frac{1}{3}}Nb_{\frac{2}{3}}\right)O_3$, the Mg^{2+} and Nb^{5+} ions are fully distributed throughout the B-site of the perovskite structure [19]. In some relaxors, the B-site sees complete translational symmetry where there is a superstructure that can contain either 1:1 or 1:2 ratios of each type of cation along the $\langle 100 \rangle$ direction [19]. This type of ordering scheme allows for the electrostatic and elastic energies of the structure to be minimized and is a primary structural property of relaxors. The amount of compositional disorder within the relaxor crystal structure can have a large impact on the ferroelectric properties. In a disordered crystal of PIN it shows relaxor ferroelectric properties but within the ordered state it is an antiferroelectric [19]. This means that throughout research careful consideration to the compositional state of a perovskite should be taken into account by monitoring sintering temperature and looking for different types of compositional disorder.

Another characteristic of relaxor materials is the frequency dependent shift observed in T_m . The total relative permittivity near the temperature of maximum permittivity is shown in equation 13 below

$$\varepsilon = 1 + \chi_e + \chi_{Ph} + \chi_R + \chi_U + \chi_{LF} \quad (13)$$

where χ is the sum total of the susceptibilities from electronic, phonon, conventional relaxor, universal relaxor, and low frequency contributions [19]. The values of χ_R and χ_U are much larger in relaxors than in traditional dielectrics and the constant decrease of χ_R to zero as temperature increases is what causes the shift in T_m with increasing frequency [19].

The temperature coefficient of permittivity ($TC\epsilon$) for relaxors above the maximum permittivity varies with temperature according to equation 14 which is known as the quadratic Curie-Weiss Law [21].

$$\frac{\epsilon'_{r_{max}}}{\epsilon'_{r(f,T)}} = 1 + \frac{(T - T_{max}(f))^{\gamma}}{2\delta^2} \quad (14)$$

Where $\epsilon'_{r_{max}}$ is the dielectric constant at T_{max} and δ represents the diffuseness parameter. The final variable γ is a parameter which indicates if the material behaves like a normal ferroelectric ($\gamma = 1$), or more like a relaxor ferroelectric where ($\gamma > 1$) and close to 2 [21]. The diffuseness parameter indicates the level of diffuseness for the peak in permittivity over temperature. In general, an increase in the diffuseness parameter equates to a decrease in the temperature coefficient of permittivity ($TC\epsilon$) [22].

It has been shown by Raengthon *et al.* that there exists a link between the tolerance factor and diffuseness parameter which is illustrated in figure 11 below. The observed trend suggests that including cations in the composition which result in an imbalance in ion size causes a broader and more diffuse peak in the temperature coefficient of permittivity [22]. To decrease the $TC\epsilon$ close to zero cations of dissimilar charge, electronic structure and size should be selected to increase the level of disorder within the B-site sub lattice [22].

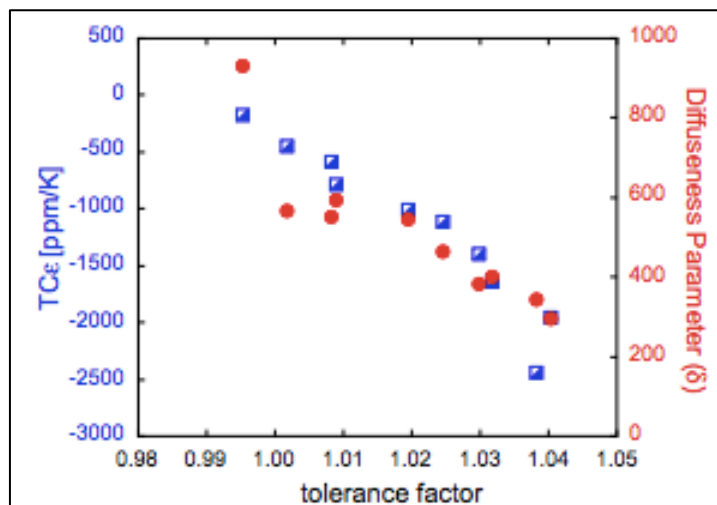


Figure 11: Relationship between the tolerance factor and diffuseness parameter in $BT - BZT - ABO_3$ compositions [22].

2.10 Competitive Materials

Capacitors are classified into three separate categories by the Electronic Industries Alliance (EIA) Standard 198. The categories are known as Class I, Class II or Class III based on their variation in electronic characteristics with temperature. Each Class of materials are differentiated by a three-letter code with the most significant classification known as C0G or by the outdated classification of NP0. The first letter in the Class I code indicates the significant figures of the change in capacitance over temperature ($C = 0$). The second letter is a multiplier of the temperature coefficient ($0 = -1$) and the third letter gives the tolerance from the temperature coefficient ($G = \pm 30 \text{ ppm/K}$). NP0 is an older classification which essentially means the same thing as C0G, that capacitance of these materials will only vary slightly over the specified temperature range of -55°C to 125°C . In considering one current available capacitor material, Mouser electronics formulations of C0G capacitors contain neodymium,

samarium and other rare earth oxides although other company's formulations will be different. Class I COG capacitors offer the lowest TCC along with very low dielectric losses making them ideal for high quality factor filters and oscillators [23]. A Class I dielectric which exhibits excellent electronic properties is $CaZrO_3$ which has a relative permittivity around 30 a very low $\tan\delta \approx 0.01$.

Class II dielectrics have a higher permittivity than Class I and use a different three-letter code system where the X7R is the most relevant designation. The first letter signifies the lower temperature limit ($X = -55^\circ\text{C}$), the second character is the upper temperature limit ($7 = 125^\circ\text{C}$), and the third letter represents the allowable change in capacitance over the specified temperature range ($R = \pm 15\%$). Class II dielectrics are most often made of ferroelectric materials based off of barium titanate. Their higher permittivity values allow for capacitors with higher volumetric efficiencies over Class I dielectrics at the cost of decreased temperature stability and accuracy. Class II dielectrics are used for frequency discrimination, bypass, coupling and decoupling applications within electrical circuits [23].

2.11 Research Objective

The goal of this research is to create a linear Class II capacitor with high volumetric efficiency that can be used for temperature dependent applications. Necessary deliverables for this project are to create a low loss material with a maximum permittivity below room temperature (T_{max}), a temperature coefficient of permittivity as close to zero as possible, and a relative permittivity above 1000.

3. Materials and Methods

This section presents the methods used to synthesize and measure the dielectric and ferroelectric properties for all compositions within this research. All compounds produced were made using the traditional solid-state reaction technique and build off of previous work of BT-BZT [22, 25] and BT-BZT-PNN compositions [26].

Nearly all compositions are some type of modified $BaTiO_3$ dielectric due to its high relative permittivity ($\epsilon_r = 1740$) and substituents ability to affect the shape of the $\epsilon_r - T$ curve [3]. Traditional dielectrics have a Curie temperature which represents a peak in the relative permittivity along with a sudden change in crystal structure from tetragonal to cubic symmetry. For relaxor dielectrics, there should be no Curie temperature but rather a slow change in crystal structure over a large temperature range. This change in crystal structure for BT-BZT compounds is often from tetragonal to a pseudocubic (rhombohedral) phase but this change allows for a very diffuse T_{max} and a decrease in the transition temperature [25]. The goal of this work is to introduce more cations of dissimilar size and electronic structure to further reduce the transition temperature and maintain a low $TC\epsilon$ achieved by other compositions such as 50BT-25BZT-25BS where $TC\epsilon = -182 \text{ ppm/K}$ [22].

3.1 Synthesis of $BaTiO_3 - Bi\left(Zn_{\frac{1}{2}}Ti_{\frac{1}{2}}\right)O_3 - ABO_3$ Compositions

Solid solutions of $BaTiO_3 - Bi\left(Zn_{\frac{1}{2}}Ti_{\frac{1}{2}}\right)O_3 - La\left(Mg_{\frac{1}{2}}Ti_{\frac{1}{2}}\right)O_3$ (BT-BZT-LMT),

$BaTiO_3 - Bi\left(Zn_{\frac{1}{2}}Ti_{\frac{1}{2}}\right)O_3 - SrTiO_3$ (BT-BZT-ST), and

$BaTiO_3 - Bi\left(Zn_{\frac{1}{2}}Ti_{\frac{1}{2}}\right)O_3 - La\left(Zn_{\frac{1}{2}}Ti_{\frac{1}{2}}\right)O_3 - SrTiO_3$ (BT-BZT-LZT-ST) are

synthesized using carbonate and oxide precursor powders which appear in table 3.1.

Before synthesis La_2O_3 , a hygroscopic compound is placed in a desiccant chamber for a minimum of 24 hours to remove water. The appropriate precursors for each composition are then weighed into stoichiometric amounts and placed in a polyethylene bottle and dissolved in an ethanol bath and twelve yttrium-stabilized zirconia (YSZ) grinding media per 10g powder. The powders are then vibratory milled for six hours and dried in an oven at 75°C for eight hours.

The dried powders are then calcined in covered cylindrical alumina crucibles to achieve the desired perovskite phase. The calcination temperature used for these compositions varies between 900 – 1200°C with a heating and cooling rate of 5°C/*min* for 4-5 hours. The calcined powders are then grinded in a mortar and pestle to reduce the particle size for X-ray diffraction. If a composition failed to fully form into the perovskite phase, the calcination temperature and time is adjusted to find the optimum conditions to form the perovskite phase.

After calcination the powder is placed in a polyethylene bottle and milled for 6 hours with 3% RHOPLEX HA-8 Emulsion binder. The solution is then dried again at 75°C for 8 hours before grinding in a mortar and pestle to reduce the material back into a powder. The powder is then formed into disk shaped pellets approximately 12mm in diameter by 1.2mm in thickness by compressing the powder under three metric tons (260 MPa) for two minutes. The pellets are then ready for sintering and are placed

within an alumina crucible and surrounded in green body of the same composition. The pellets are then placed in a furnace where binder burnout takes place at 400°C for 3 hours with a heating and cooling rate of 5°C/min. Typical sintering temperature for these compositions take place anywhere between 1000 – 1300°C for 4-5 hours. Pellet dimensions are recorded before and after sintering to verify densification of the ceramic.

Once the pellets are fully sintered and cooled they are polished with SiC abrasive paper from 180-1000 grit. This creates a uniform composition at the surface and helps with application of the silver electrodes. Silver paste is then painted onto each side of the sintered pellet and dried at 75°C for ten minutes. After the silver paste is dry enough the electrodes are fired in the furnace at 750°C for thirty minutes.

3.2 Synthesis of $Pb\left(Ni_{\frac{1}{3}}Nb_{\frac{2}{3}}\right)O_3$ Based Compositions

Compositions including $BaTiO_3 - Bi\left(Zn_{\frac{1}{2}}Ti_{\frac{1}{2}}\right)O_3 - La\left(Zn_{\frac{1}{2}}Ti_{\frac{1}{2}}\right)O_3 - Pb\left(Ni_{\frac{1}{3}}Nb_{\frac{2}{3}}\right)O_3$ (BT-BZT-LZT-PNN), $PbTiO_3 - Pb\left(Ni_{\frac{1}{3}}Nb_{\frac{2}{3}}\right)O_3 - NaNbO_3$ (PT-PNN-NN), and $PbTiO_3 - Pb\left(Ni_{\frac{1}{3}}Nb_{\frac{2}{3}}\right)O_3 - Bi\left(Zn_{\frac{1}{2}}Ti_{\frac{1}{2}}\right)O_3 - NaNbO_3$ (PT-PNN-BZT-NN) are synthesized using the columbite precursor method as shown by Alberta and Bhalla [27]. For this method NiO and Nb_2O_5 are weighed into stoichiometric amounts and milled in 100% ethanol and YSZ media for 6 hours. The slurry is then dried at 75°C for eight hours and calcined at 1200°C for two hours in a closed

crucible. The finished product is $NiNb_2O_6$ which can then be combined in stoichiometric amounts with the other necessary precursors listed in table 3.1. Calcination temperatures vary for these compositions from 900 – 1100°C for four to five hours. The calcined powder then has 3% RHOPLEX binder added once again and is vibratory milled for six hours. Pellets are formed under three metric tons for two minutes and sintered in a closed crucible between 1150 – 1250°C for five hours.

Table 1 Precursor, purity, and supplier for compositions synthesized in this work.

Compound	Purity	Supplier
$BaCO_3$	99.8%	Alfa Aesar
Bi_2O_3	99.9%	Aldrich
ZnO	99.9%	Alfa Aesar
Nb_2O_5	99.9%	Aldrich
TiO_2	99.9%	Aldrich
PbO	99.9%	Sigma Aldrich
NiO	99.99%	Aldrich
$MgCO_3$		Sigma
La_2O_3	99.9%	Aldrich
Na_2CO_3	99.95%	Alfa Aesar

3.3 Electronic Characterization

After the sample has been prepared in a parallel plate capacitor arrangement it is ready for electronic characterization. To measure the capacitance, relative permittivity and dielectric loss with respect to temperature, the sample is placed in a NorECS Probostat high temperature cell. The Probostat is used to measure the electronic properties of the sample from 20 – 550°C with a heating and cooling rate of 2°C/*min*. The low ramp rate is to allow for the HP 4192A impedance analyzer to scan through frequencies from 25 Hz to 1 MHz and collect capacitance and $\tan \delta$ data along the way. This data is then stored into a text file using a custom-made program in Labview software where the dielectric constant can be calculated.

Low temperature capacitance and $\tan \delta$ data is collected from –150°C *to* 160°C using the liquid nitrogen cooled environmental chamber Delta 9023. Measurements for the low temperature data should begin at a high temperature and cool down at 2°C/*min* to avoid frost melt on the sample holder electrodes. Electronic property data is collected from 25 Hz to 1 MHz using the Agilent 4284A Precision LCR Meter and stored in a text file using the same Labview program.

Polarization vs electric field data is collected on each composition using the Precision Premier II ferroelectric test system. Typically, ferroelectrics have non-linear hysteresis loops similar to figure 2 in polarization vs electric field P(E) measurements. For compositions in this work linear P(E) measurements are desired which indicate the material is a relaxor dielectric.

3.4 Physical Characterization

The structure of each composition was determined after the calcine stage and the sintering stage using X-ray powder diffraction. Each sintered pellet was ground as finely as possible in a mortar and pestle and added to the powder sample holder for analysis. The diffractometer used for this experiment is the Bruker D8 Discover with $CuK\alpha$ radiation. Each composition was scanned from $20 - 90^\circ$ at $5^\circ/min$.

The measured density of each pellet was found by taking diameter and thickness measurements using a Mitutoyo 293-369 digital micrometer which has $\pm 1\mu m$ instrumental error. The diameter and thickness of each sample was measured three times and averaged to account for variations within each pellet. Three different per composition are measured and weighed to minimize errors when measuring the density. The measured density is then compared against the theoretical density which is calculated based off of the lattice parameter obtained from X-ray diffraction data.

The most accurate method for obtaining the theoretical density is a combination of an analytical method proposed by M. U. Cohen and the least-squares principle which minimizes the effect of random observational errors. The method for obtaining the lattice parameter is depicted below.

Recall from equation 10 Bragg's law

$$\lambda = 2d\sin\theta$$

Start by squaring the Bragg equation and taking the logarithm of each side

$$\log \sin^2 \theta = \log \left(\frac{\lambda^2}{4} \right) - 2 \log d$$

Differentiation of this equation gives

$$\frac{\Delta \sin^2 \theta}{\sin^2 \theta} = - \frac{2 \Delta d}{d}$$

Assume the combined systematic errors take the form

$$\frac{\Delta d}{d} = K \cos^2 \theta$$

Combining the previous two equations gives

$$\Delta \sin^2 \theta = -2K \cos^2 \theta \sin^2 \theta = D \sin^2 2\theta$$

where D is a new constant.

If the true value of $\sin^2 \theta$ for a diffraction peak is

$$\sin^2 \theta (true) = \frac{\lambda^2}{4a_0^2} (h^2 + k^2 + l^2)$$

where a_0 is the true value of the lattice parameter which is needed to find the theoretical density

$$\sin^2 \theta (observed) - \sin^2 \theta (true) = \Delta \sin^2 \theta$$

Then

$$\sin^2 \theta (observed) = A\alpha + C\delta$$

Where $A = \frac{\lambda^2}{4a_0^2}$, $\alpha = (h^2 + k^2 + l^2)$, $C = \frac{D}{10}$, and $\delta = 10 \sin^2 2\theta$. The parameter D is

known as the drift constant and should be kept as small as possible for the highest

precision. The equations for the observed reflections can now be solved

simultaneously to calculate A and C , from which the true lattice parameter a_0 can be calculated.

As stated earlier, combining the Cohen analytical method with the least squares principle will reduce the effect of random observational error. The best values for A and C are those which the sum of squares of the random observational error (e) is at a minimum.

$$\sum (e)^2 = a \text{ minimum} = \sum [A\alpha + C\delta - \sin^2 \theta (\text{observed})]^2$$

Differentiating with respect to both A and C gives

$$\begin{aligned} \sum \alpha \sin^2 \theta &= A \sum \alpha^2 + C \sum \alpha\delta \\ \sum \delta \sin^2 \theta &= A \sum \alpha\delta + C \sum \delta^2 \end{aligned}$$

Solving these two equations simultaneously gives the true value of A which can then be used to find the true lattice parameter a_0 [28].

To reduce error in a lattice parameter measurement it is necessary to have as many reflections as possible at as high angles as possible [28]. This is because as θ increases the variation and therefore error within $\sin\theta$ decreases regardless of how accurately θ is measured [28]. Since $\sin\theta$ is what actually appears in the Bragg equation increasing the value of θ will result in the most accurate linear extrapolation of the lattice parameter.

When using Cohen's method to calculate the lattice parameter there is always random and systematic errors within the measurement. Random errors do not vary in a regular manner and can be ignored, however systematic errors do vary in a regular manner

and always have the same sign. A study done by Campos et al. on the contribution of systematic error to the determination of the lattice parameter found that the most significant contribution is from sample displacement from the diffractometer axis. Sample displacement is when the sample is misplaced in relation to the plane normal to the plane of incidence [29]. Even on a well aligned system the displacement of the specimen from the diffractometer axis can result in variations of the lattice parameter by as much as 0.001 \AA [29]. Other contributions to the systematic error include instrument offset, adsorption, and sample curvature however it was found by Campos et al. that all of these sources are minuscule when compared to sample displacement [29]. Instrument misalignment only becomes a dominant factor when the sample displacement is less than $10 \mu\text{m}$ [29].

4. Results

Many of the compositions in this work are based around the $BaTiO_3 - Bi\left(Zn_{\frac{1}{2}}Ti_{\frac{1}{2}}\right)O_3$ system which has been extensively researched for high energy density capacitor applications. This is because of its high relative permittivity (≈ 1000) spread over a broad temperature range. This is created by the substitution of Bi^{3+} atoms onto the A site and Zn^{2+} atoms onto the B site of the perovskite structure [22]. However, the BT-BZT system has a $T_{max} \approx 100^\circ\text{C}$ meaning that the main focus of this work is to shift the T_{max} down below 0°C without causing a detrimental effect on the $TC\epsilon$. The inclusion of $SrTiO_3$ as a constituent is done because its tolerance factor is equal to one, which was shown earlier to be linked to lowering the $TC\epsilon$ [7]. Another constituent that often appears in this work is $Pb\left(Ni_{\frac{1}{3}}Nb_{\frac{2}{3}}\right)O_3$ which is a relaxor type ferroelectric with a diffuse phase transition that occurs at its Curie temperature $T_c = -120^\circ\text{C}$. The goal of including PNN into compositions is to maintain a high relative permittivity while simultaneously lowering the temperature at which T_{max} occurs.

The constituent $La\left(Mg_{\frac{1}{2}}Ti_{\frac{1}{2}}\right)O_3$ was included into the BT-BZT system because of research done by Salak et al. where 2.5% doping of LMT into BT resulted in a transition from ferroelectric to relaxor behavior coupled with a decrease in T_{max} . This decrease is a result of the substitution of La^{3+} atoms onto the A site and Mg^{2+} atoms onto the B site of the perovskite lattice [30]. Further manipulations to these compositions were done as more trends were observed.

4.1 $BaTiO_3 - Bi\left(Zn_{\frac{1}{2}}Ti_{\frac{1}{2}}\right)O_3 - SrTiO_3$ System

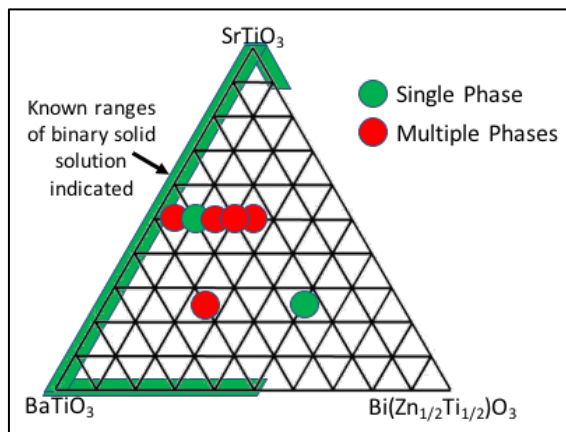


Figure 12: The ternary diagram for BT-BZT-ST compositions with single phase perovskite compositions shown in green.

The X-ray diffraction data for the BT-BZT-ST system are shown in figure 13 with additional scans shown in Appendix A. The results show that it was difficult to obtain the perovskite phase, likely due to problems in maintaining the correct stoichiometry.

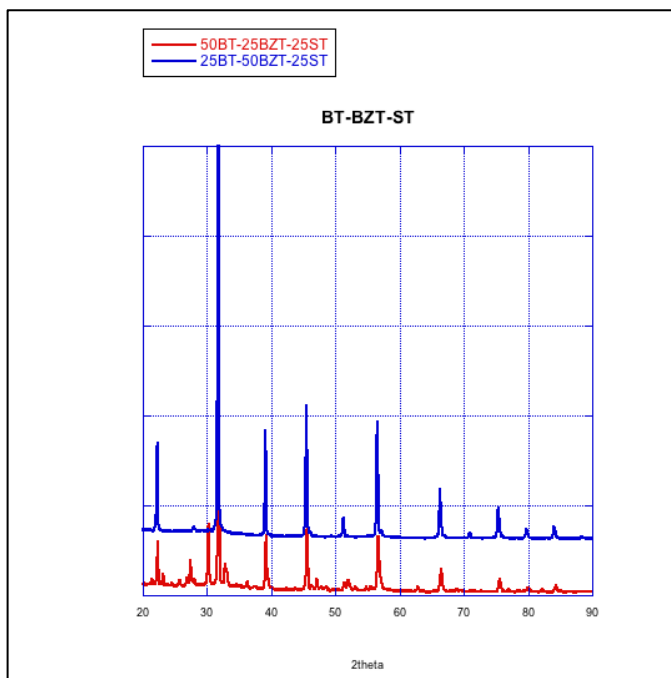


Figure 13: X-ray diffraction data for the two compositions in the BT-BZT-ST system for which dielectric data was measured.

The 25BT-25ST-50BZT composition shows a large dielectric peak just above room temperature along with relatively low dielectric loss. In contrast, the 50BT-25ST-25BZT composition is characterized by a relatively temperature independent dielectric trend, though the dielectric loss values are unacceptably high.

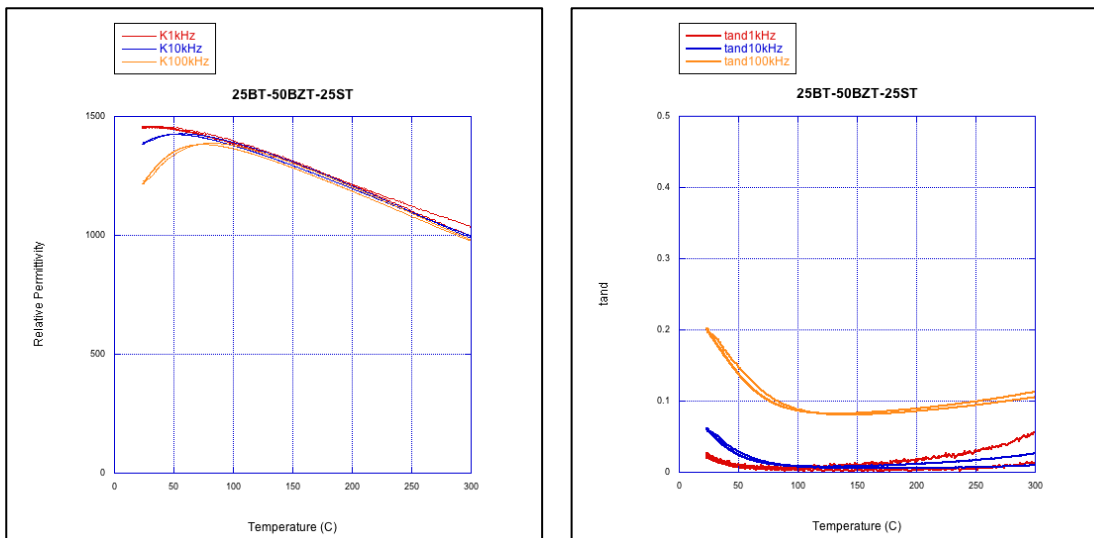


Figure 14: (a) Relative permittivity and (b) dielectric loss versus high temperature of 25BT-50BZT-25ST from 25 – 300°C shows a maximum permittivity above room temperature.

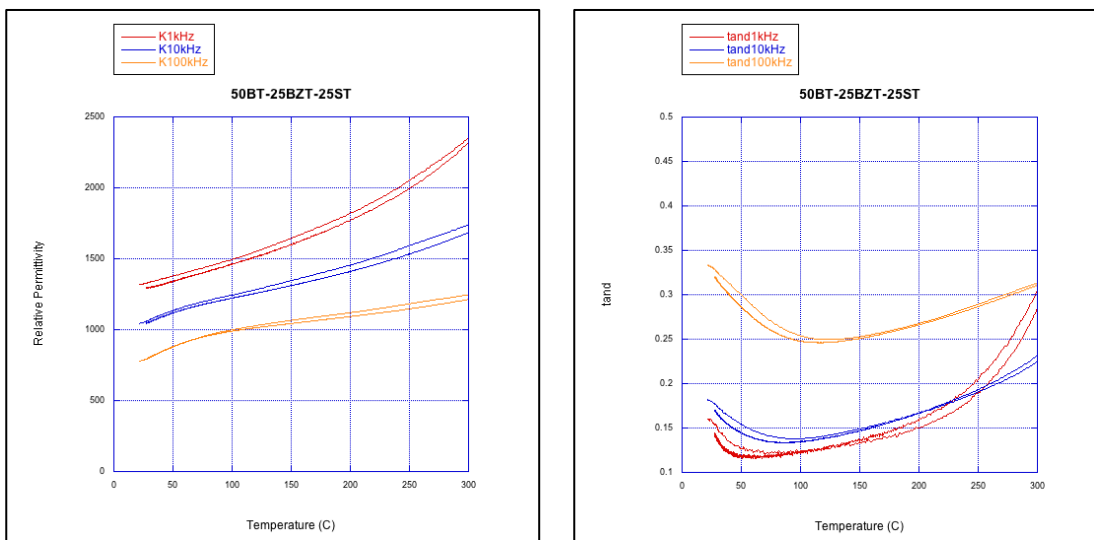


Figure 15: (a) The relative permittivity and (b) dielectric loss versus temperature for 50BT-25BZT-25ST shows a positive $T\epsilon$ and high levels of $\tan\delta$.

After observing the poor dielectric loss values combined with the difficulty in achieving a single phase perovskite this ternary system was abandoned and no additional characterization techniques were performed.

4.2 $BaTiO_3 - Bi\left(Zn_{\frac{1}{2}}Ti_{\frac{1}{2}}\right)O_3 - La\left(Mg_{\frac{1}{2}}Ti_{\frac{1}{2}}\right)O_3$ System

Select compositions in the $BaTiO_3$ - $Bi(Zn_{1/2}Ti_{1/2})O_3$ - $La(Mg_{1/2}Ti_{1/2})O_3$ system were fabricated. The specific compositions are indicated in the ternary diagram below.

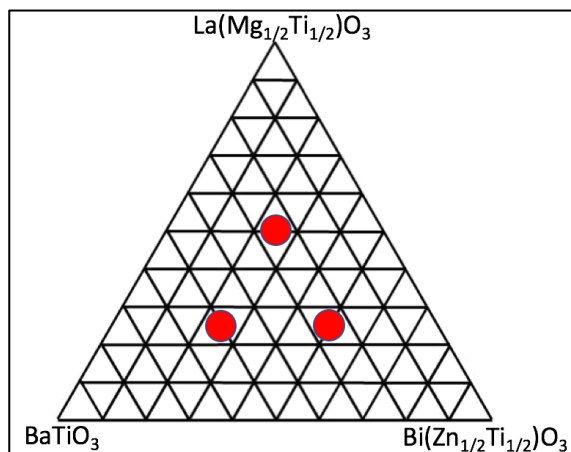


Figure 16: Ternary compositions characterized within the BT-BZT-LMT system. The 25BT-50BZT-25LMT composition was not able to achieve single phase perovskite structure.

The XRD data on these compositions show that single phase or nearly single phase perovskite is stable for the 25BT-25BZT-50LMT and the 50BT-25BZT-25LMT composition. The 25BT-50BZT-25LMT composition exhibited multiple phases – suggesting that the perovskite phase was not stable in this system.

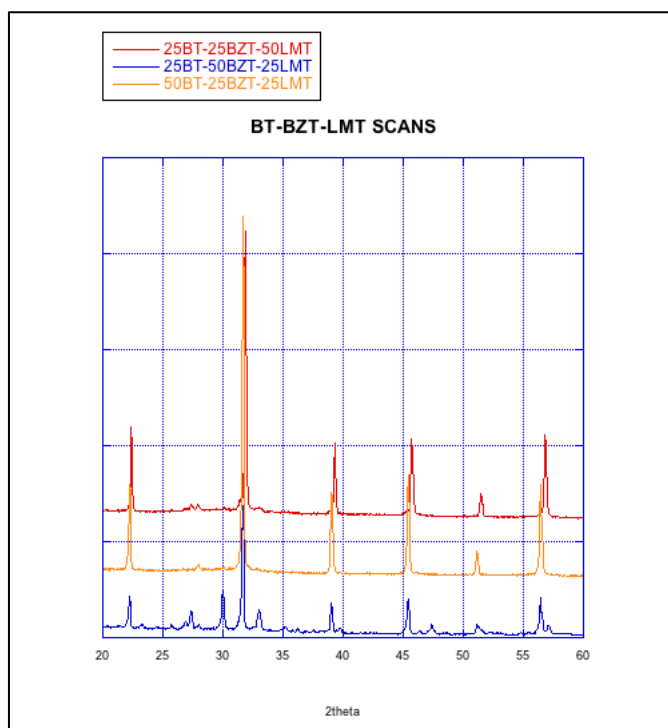


Figure 17: X-ray diffraction data shows single phase perovskite structure for 25BT-25BZT-50LMT and 50BT-25BZT-25LMT compositions.

Table 2: Physical properties of the perovskite materials in the BT-BZT-LMT system.

Composition	Lattice Parameter (Å)	Geometric Density(g/cm ³)	Theoretical Density(g/cm ³)	Tolerance Factor
25BT-25BZT-50LMT	3.98	5.549	6.075	0.972
50BT-25BZT-25LMT	3.99	6.096	6.10	1.001

Compositions with high levels of LMT showed low TC ϵ and low dielectric loss as seen in table 3. However, the low level of BaTiO₃ created a material with very low permittivity that did not meet required specifications. Increasing the levels of Bi(Zn_{1/2}Ti_{1/2})O₃ created an unstable phase and compositions with this high of a level of Bi(Zn_{1/2}Ti_{1/2})O₃ were no longer investigated.

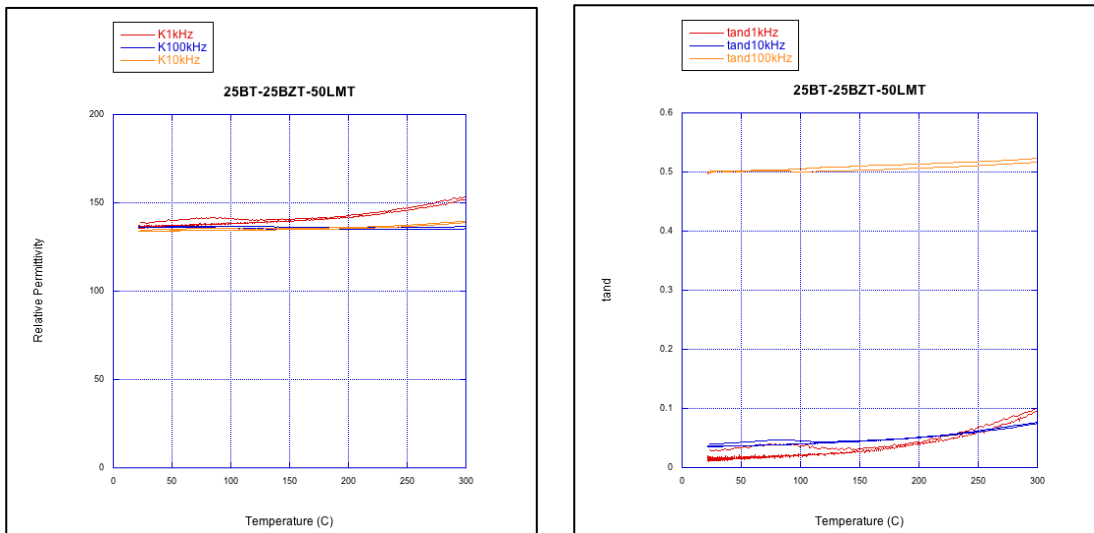


Figure 18: (a) The relative permittivity versus temperature and (b) dielectric loss vs temperature for 25BT-25BZT-50LMT. The dielectric loss is large for 100kHz frequency at all temperatures in this plot which contradicts the low temperature data.

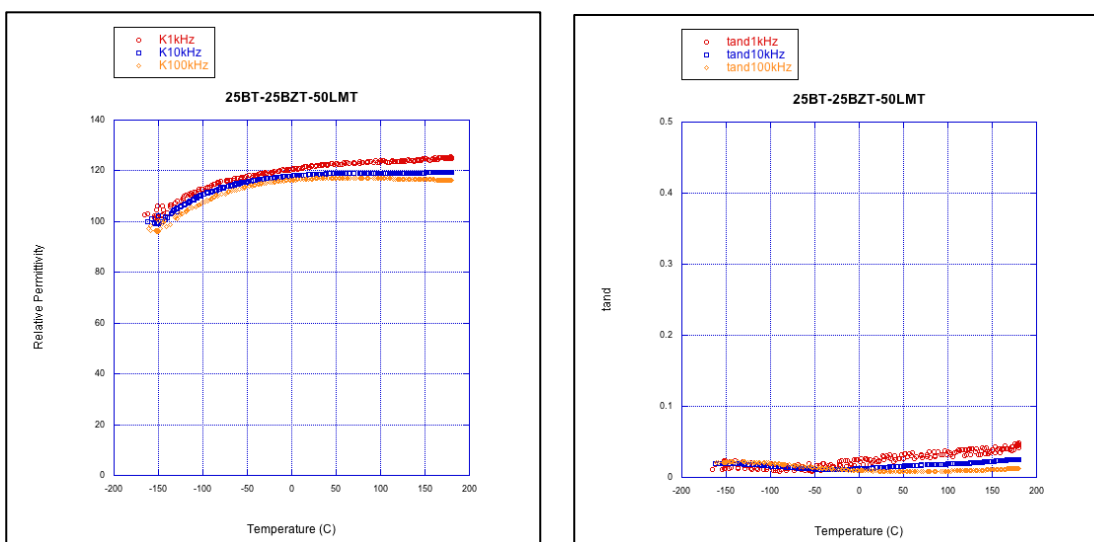


Figure 19: (a) Relative permittivity and (b) dielectric loss versus low temperature of 25BT-25BZT-50LMT from -200 to 200°C shows a low $TC\epsilon$ along with low dielectric loss.

Polarization experiments showed that these materials exhibited a linear dielectric response with very little hysteresis, as expected from the temperature dependent dielectric property data.

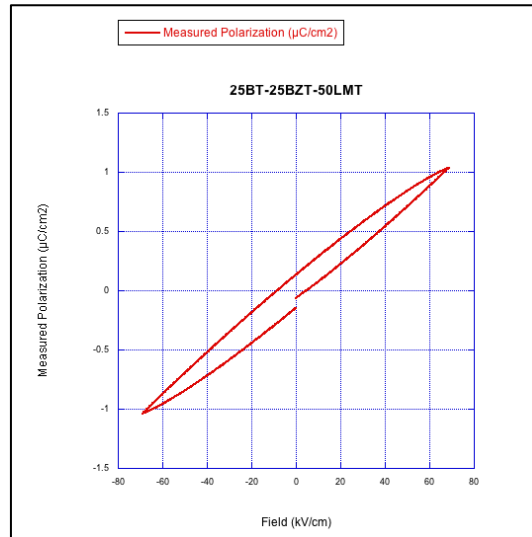


Figure 20: Polarization versus electric field measurement of 25BT-25BZT-50LMT shows a linear dielectric with little to no hysteresis.

Increasing the concentration of BaTiO₃ in this system proved to be unsuccessful as it only slightly increased the overall permittivity while increasing the temperature dependence by a factor of 4. Both of the single-phase compositions meet X7R capacitor specifications which is $\pm 15\% \frac{\Delta C}{C_0}$ from -55°C to 125°C . Where C_0 is the capacitance at ambient temperature.

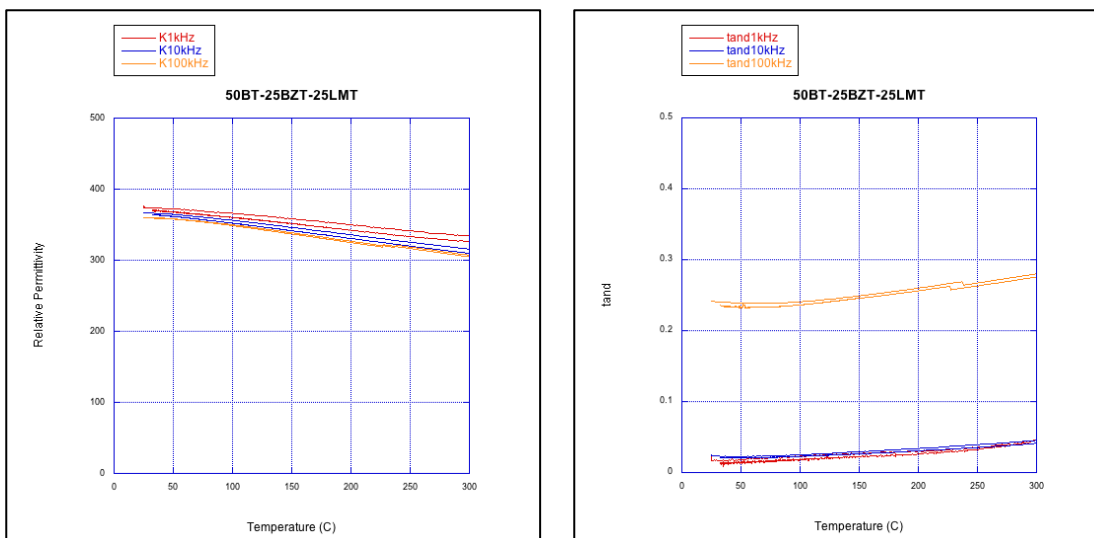


Figure 21: (a) Relative permittivity and (b) dielectric loss versus high temperature of 50BT-25BZT-25LMT shows a low $T C \epsilon$ and low $\tan \delta$ at low frequencies.

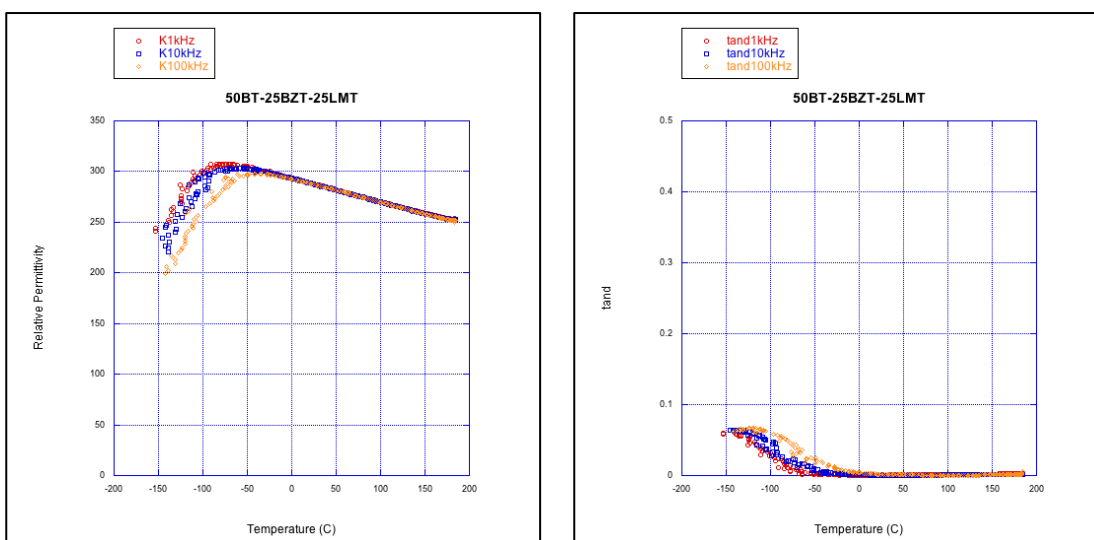


Figure 22: (a) Low temperature relative permittivity and (b) dielectric loss versus temperature of 50BT-25BZT-25LMT from -200 to 200°C shows a T_{max} well below 0°C .

Polarization versus electric field measurements confirm that the 50BT-25BZT-25LMT composition behaves like a linear dielectric.

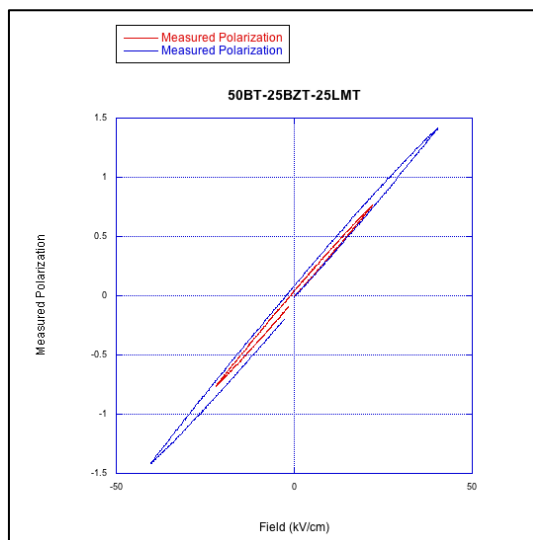
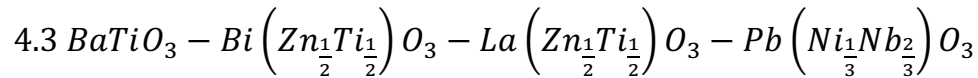


Figure 23: Polarization versus electric field measurement shows the 50BT-25BZT-25LMT composition can withstand electric fields up to 40kV/cm.

Table 3: Dielectric properties for the BT-BZT-LMT system.

Composition	$TC\epsilon_{mid}$ (ppm/°C)	$TC\epsilon_{low}$ (ppm/°C)	T_{max} (°C)	ϵ at T_{max}	X7R Capacitance Variation
25BT-25BZT-50LMT	-136	759	300.3	140	3.10%
50BT-25BZT-25LMT	536	3241	25.2	376	13.30%



After observing the low temperature dependence of samples containing large amounts of $\text{La}\left(\text{Mg}_{\frac{1}{2}}\text{Ti}_{\frac{1}{2}}\right)\text{O}_3$ this finding was applied to a lead based system which had achieved larger permittivity's with the plan to take a small loss in permittivity for an improved temperature dependence. From previous work it was noted that compositions near 50BT-25BZT-25PNN had the best electronic properties and compositions with higher levels of $\text{Bi}(\text{Zn}_{1/2}\text{Ti}_{1/2})\text{O}_3$ became unstable. The goal of this system is to experiment with different levels of La in place of Bi to create higher levels of disorder within the perovskite structure to lower $\text{TC}\epsilon$. The specific compositions studied are indicated in the ternary diagram below.

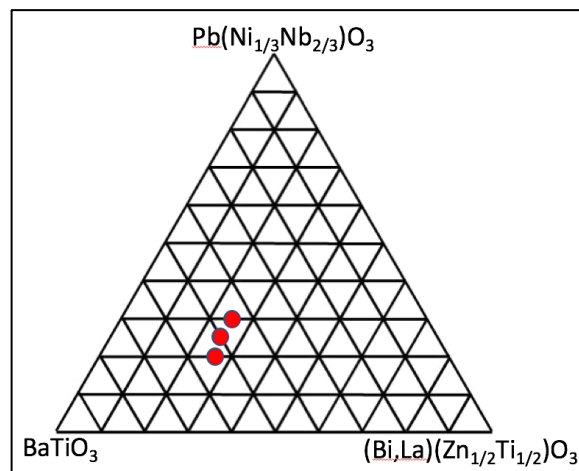


Figure 24: Ternary diagram for compositions within the BT-BZT-LZT-PNN system with 30% PNN.

4.3.1 30% PNN System

Looking first at compositions with 30% PNN and varying the Bi/La ratio, the XRD and dielectric data are shown below.

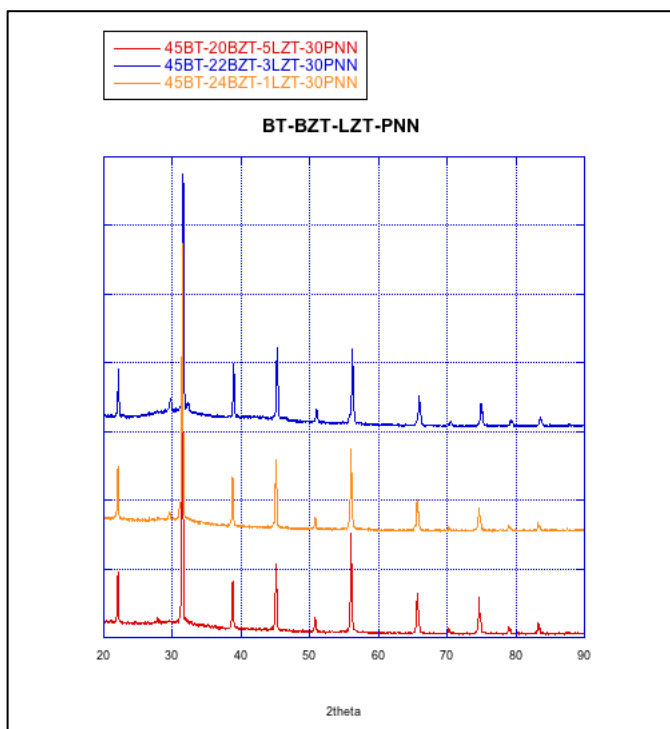


Figure 25: X-ray diffraction data for the BT-BZT-LZT-PNN system shows a single phase perovskite structure for all compositions. There is a slight peak just before the (110) peak.

XRD data on these compositions show that single phase perovskite can be achieved at the optimum calcination and sintering temperatures. Some minor secondary peaks were observed in these compositions which continued to increase in peak intensity with increasing sintering temperature.

Table 4: Physical characteristics of compositions within the BT-BZT-LZT-PNN system.

Composition	Lattice Parameter (Å)	Geometric Density(g/cm ³)	Theoretical Density(g/cm ³)	Tolerance Factor
45BT-20BZT-5LZT-30PNN	4.0179	4.92	7.205	1.006
45BT-22BZT-3LZT-30PNN	4.0184	5.544	7.240	1.006
45BT-24BZT-1LZT-30PNN	4.0145	5.963	7.299	1.006
45BT-24BZT-1LZT-30PNN 3% La	-	5.485	-	-
50BT-15BZT-10LZT-25PNN	-	4.663	-	1.01
50BT-20BZT-5LZT-25PNN	-	5.759	-	1.01
50BT-22BZT-3LZT-25PNN	4.0145	5.319	7.128	1.01
50BT-24BZT-1LZT-25PNN	4.0185	6.151	7.144	1.01
50BT-24BZT-1LZT-25PNN 3% La	4.0222	6.662	7.125	-
53BT-20BZT-7LZT-20PNN	4.0118	6.383	6.977	1.011
55BT-20BZT-5LZT-20PNN	4.013	6.112	6.966	1.014

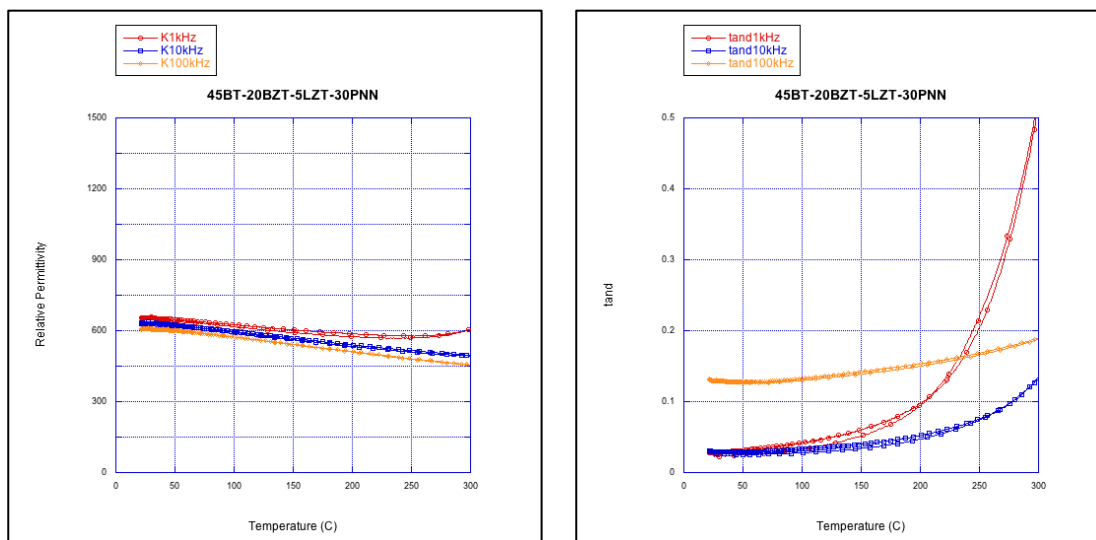


Figure 26: (a) Relative permittivity measurements of 45BT-20BZT-5LZT-30PNN show a linear dependence with temperature while (b) dielectric loss exhibits large values at temperatures above **150°C**.

High temperature permittivity measurements for 45BT-22BZT-3LZT-30PNN show non-linear temperature dependence and high values for dielectric loss. This could be due to poor sample density allowing an increase in charge mobility which causes the dielectric loss to be unacceptably high at high frequencies.

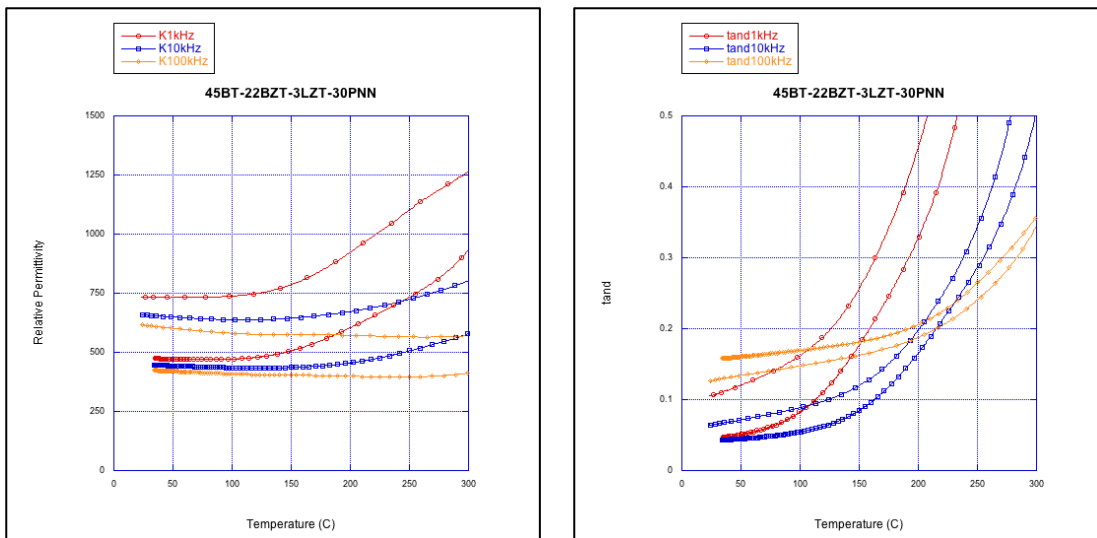


Figure 27 (a) The relative permittivity and (b) dielectric loss show a hysteresis and large $TC\epsilon$ for the 45BT-22BZT-3LZT-30PNN composition.

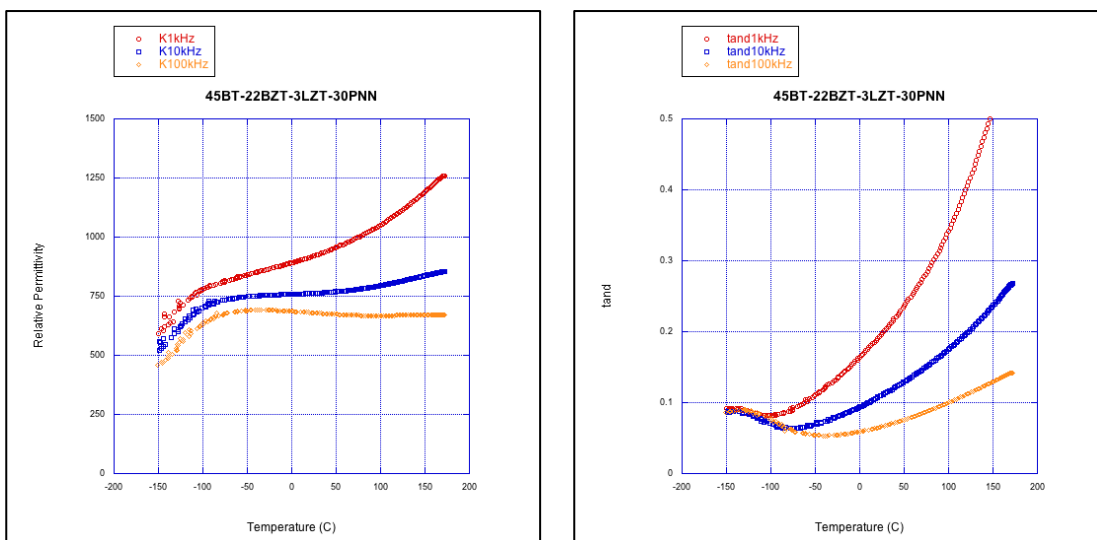


Figure 28 (a) Low temperature measurements for 45BT-22BZT-3LZT-30PNN relative permittivity versus temperature and (b) dielectric loss versus temperature. The dielectric loss for this composition is too large to be considered for electronic device applications.

The 45BT-24BZT-1LZT-30PNN composition has low dielectric loss values at low frequencies but it begins to creep up with higher temperature and frequency to undesirable values. However, this composition does meet X7R specifications as seen in table 5. as it has a maximum change in capacitance of 5.6% over the temperature

range of -55°C to 125°C . Through a polarization versus electric field measurement seen in figure 31, this sample was confirmed to have a linear dielectric response with no hysteresis.

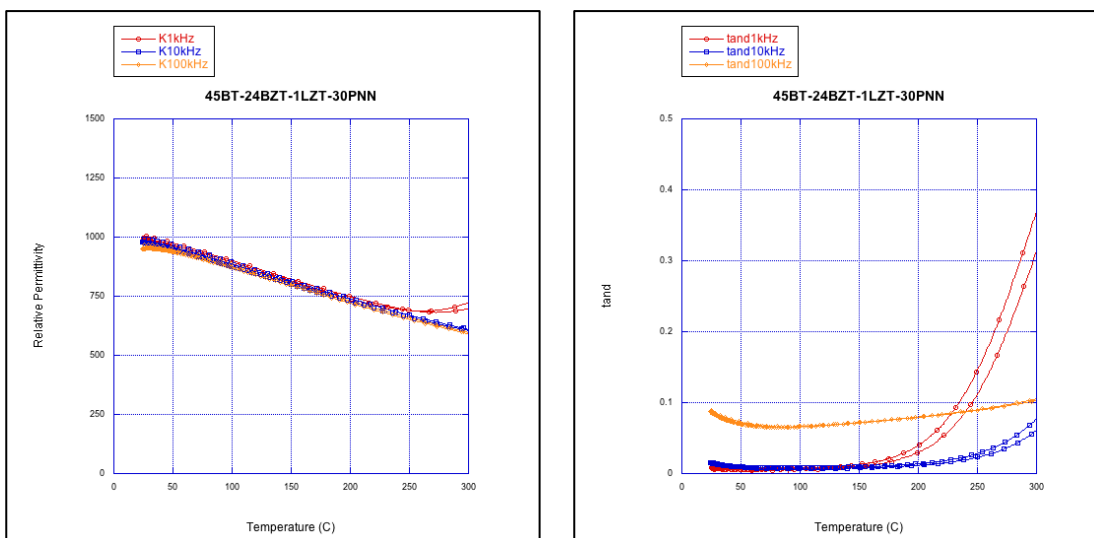


Figure 29: (a) Relative permittivity versus high temperature of 45BT-24BZT-1LZT-30PNN shows a strong linear dependence. (b) The dielectric loss versus temperature plot shows this composition is viable up to 200°C .

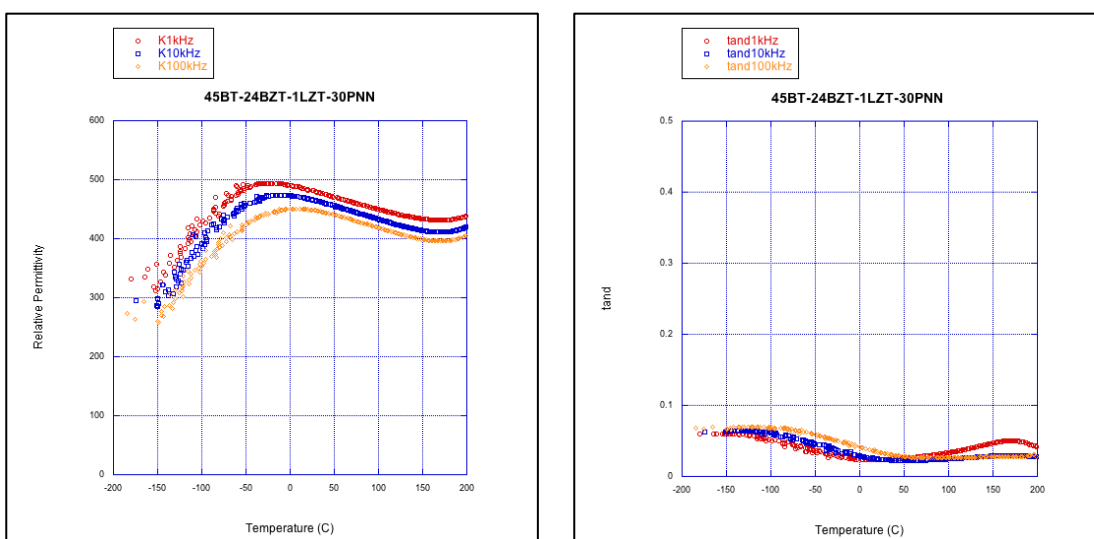


Figure 30: (a) Low temperature permittivity versus temperature measurements of 45BT-24BZT-1LZT-30PNN show a T_{max} below room temperature while the (b) dielectric loss versus temperature graph remains below 0.05 for all temperatures.

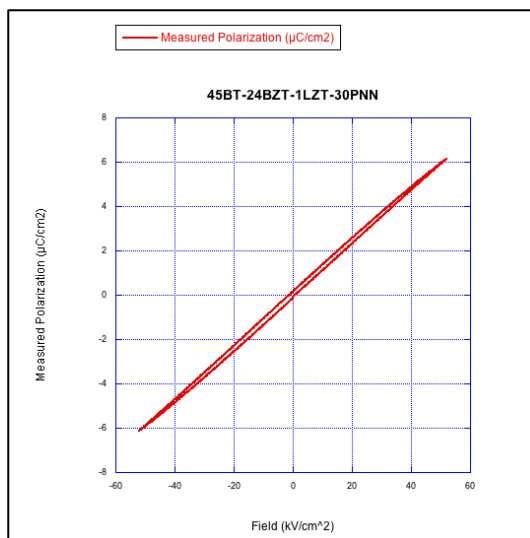


Figure 31: Polarization versus electric field measurements confirm that 45BT-24BZT-1LZT-30PNN is a viable linear dielectric relaxor.

Compositions with some additional La were prepared (though simple modification of the batch stoichiometry) but the results show a deterioration in the dielectric properties, including an increase in the polarization hysteresis which is likely due to an increase in dielectric loss.

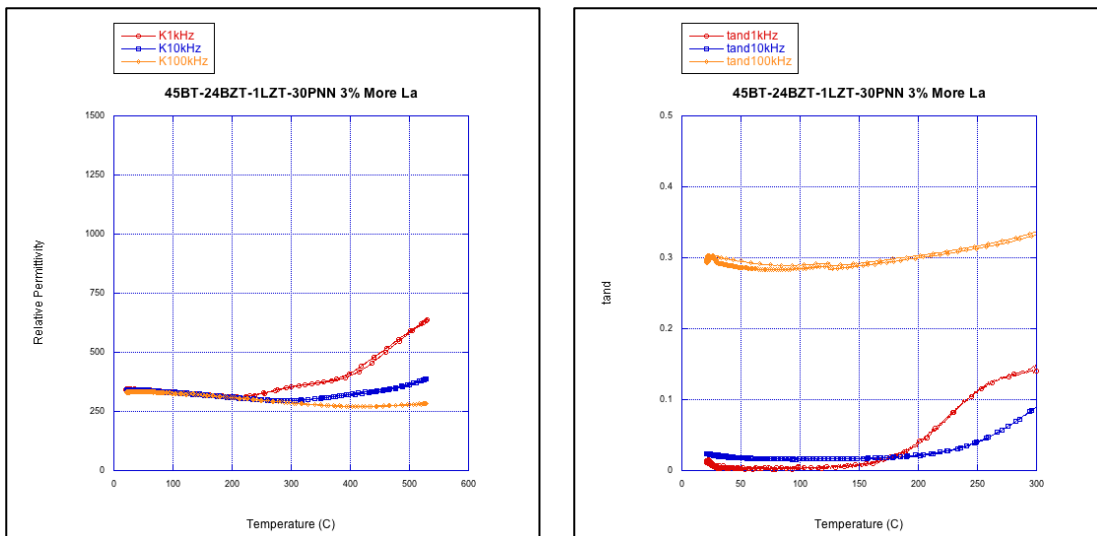


Figure 32: (a) Relative permittivity and (b) dielectric loss versus temperature measurements for 45BT-24BZT-1LZT-30PNN with 3% extra La show an improvement in the TCE while reducing the overall relative permittivity.

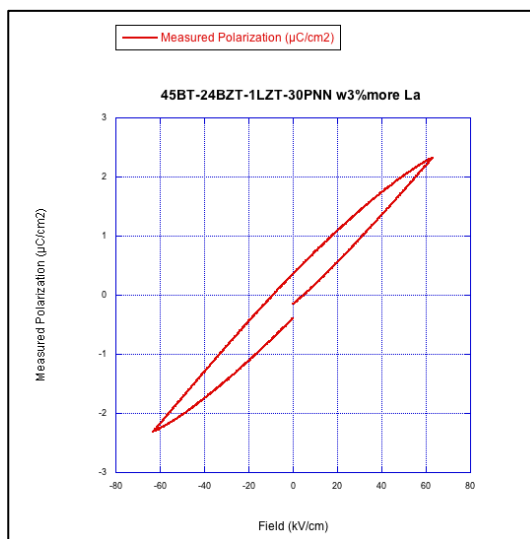


Figure 33: Polarization versus electric field measurements of 45BT-24BZT-1LZT-30PNN with extra La show a linear dielectric material that can withstand fields up to 40kV/cm before shorting.

4.3.2 25% PNN System

XRD data for the 25% PNN compositions indicate that single phase perovskite can be obtained for LZT concentrations up to 10%. At higher LZT concentrations it was not possible to obtain single phase perovskite as secondary phases were present.

Diffraction data for the compositions which contain a secondary phase can be found in Appendix A. The symmetry of the perovskite phase appears to be cubic with no apparent peak splittings.

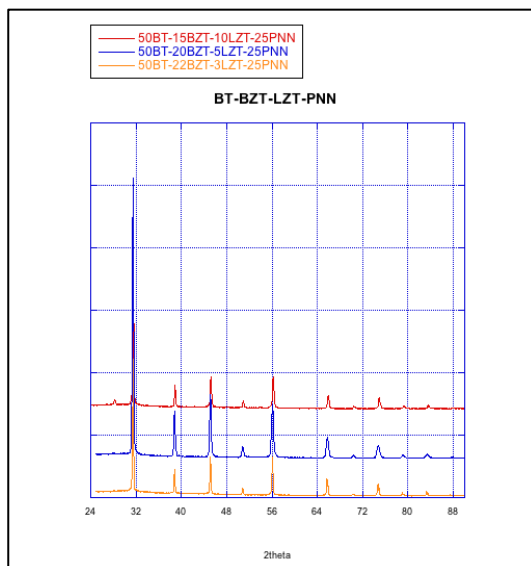


Figure 34 X-ray diffraction data for compositions containing 25% PNN show a cubic perovskite phase with a minor peak just before the (110) plane showing up in the 50BT-15BZT-10LZT-25PNN composition.

Slight modifications were made to the sample composition to help strike a balance between the low T_{max} provided by PNN and the decrease in $TC\epsilon$ from additional LZT in proper stoichiometric amounts. Dielectric measurements for the first composition 50BT-15BZT-10LZT-25PNN show a linear dependence with temperature from around -50°C up to 190°C . The downsides to this composition are the poor density

observed in table 4. along with the non-linear polarization and hysteresis that occurs in PvsE measurements.

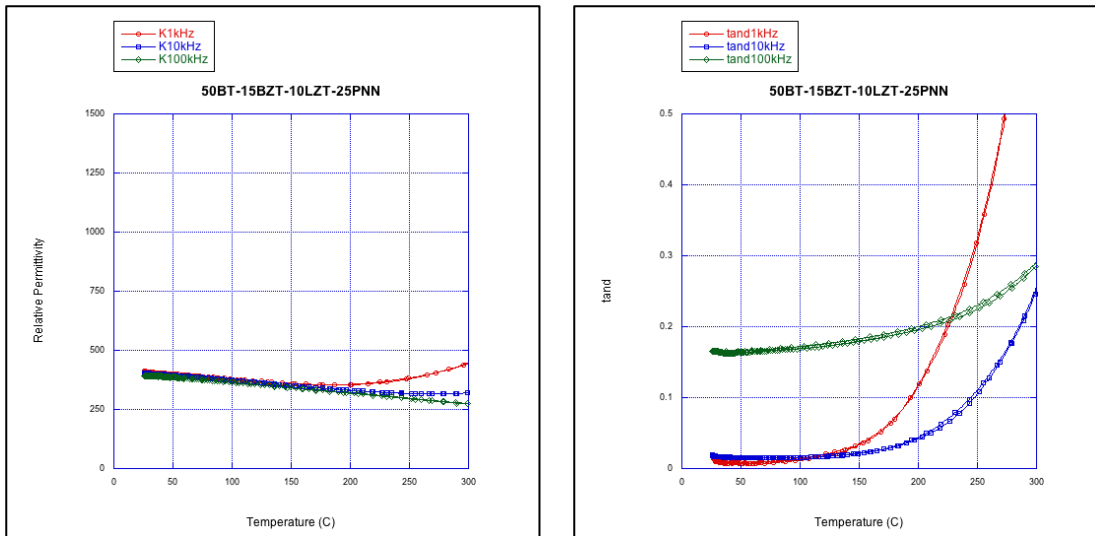


Figure 35: (a) While the 50BT-15BZT-10LZT-25PNN composition has a low TCE the maximum relative permittivity is reduced as well. (b) dielectric loss versus temperature shows large increases in the loss at temperatures above 150°C .

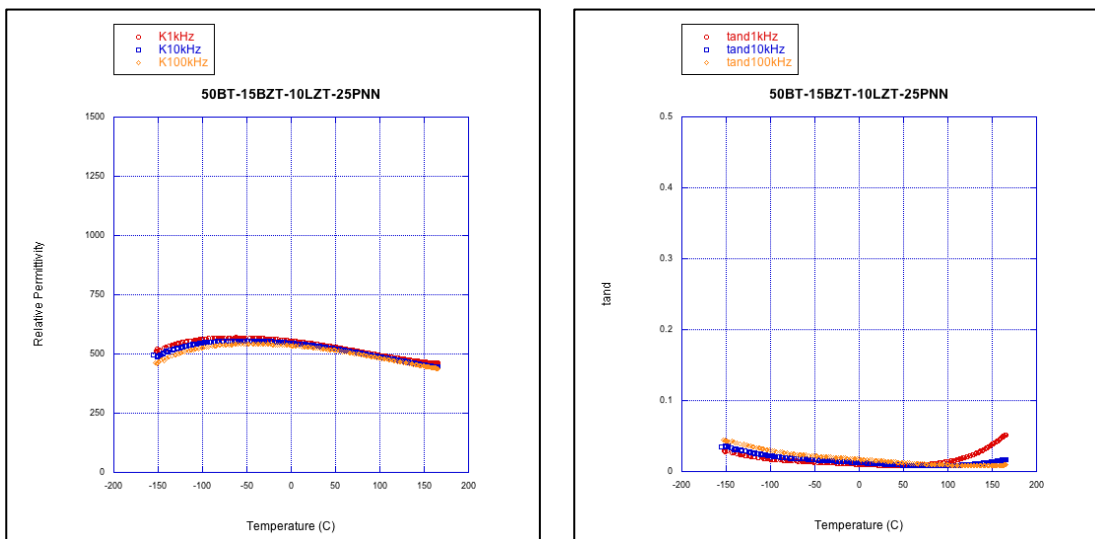


Figure 36: The low temperature measurements for the (a) relative permittivity and (b) dielectric loss of 50BT-15BZT-10LZT-25PNN show a temperature of maximum permittivity well below 0°C with a very low TCE .

Polarization hysteresis measurements show clear evidence of a linear dielectric response, though the dielectric loss (as seen in the hysteresis) increases markedly for compositions with the highest LZT concentration.

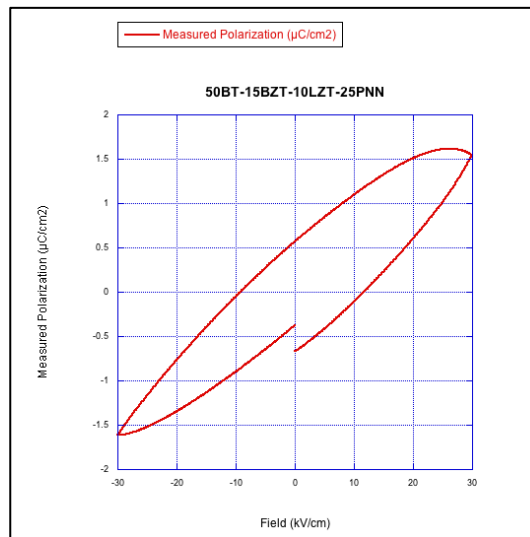


Figure 37: Polarization versus electric field measurements of 50BT-15BZT-10LZT-25PNN shows that this is a linear dielectric but it does have some higher levels of loss and shows some hysteresis.

Modification of the composition stoichiometry to include more BZT proved to decrease the dielectric loss at high frequency up to 300°C. The low temperature permittivity shows a maximum permittivity well below room temperature. Below the maximum permittivity the low temperature $TC\epsilon$ greatly increases.

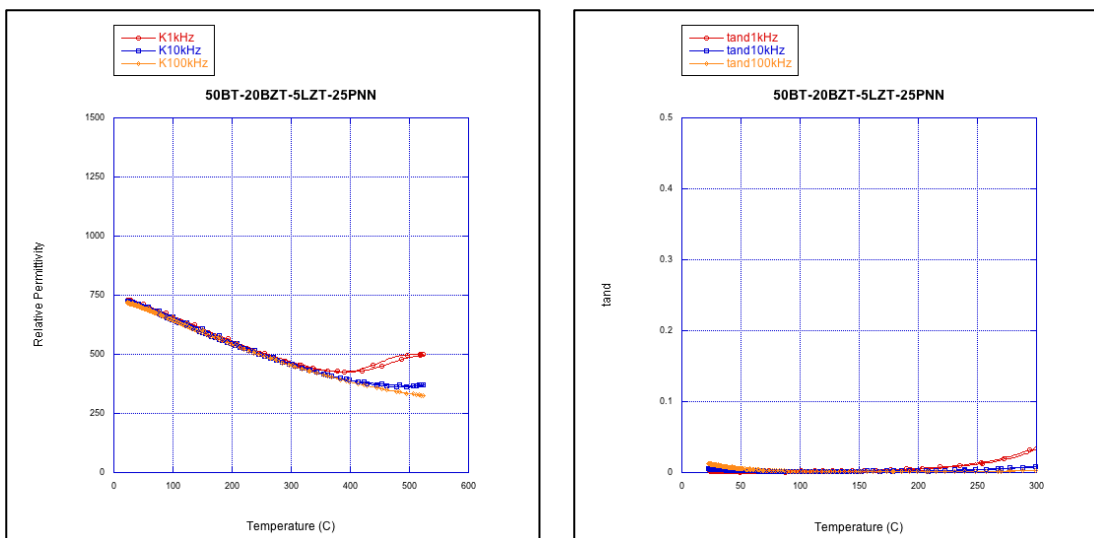


Figure 38: (a) Relative permittivity and (b) dielectric loss versus temperature for 50BT-20BZT-5LZT-25PNN at high temperatures.

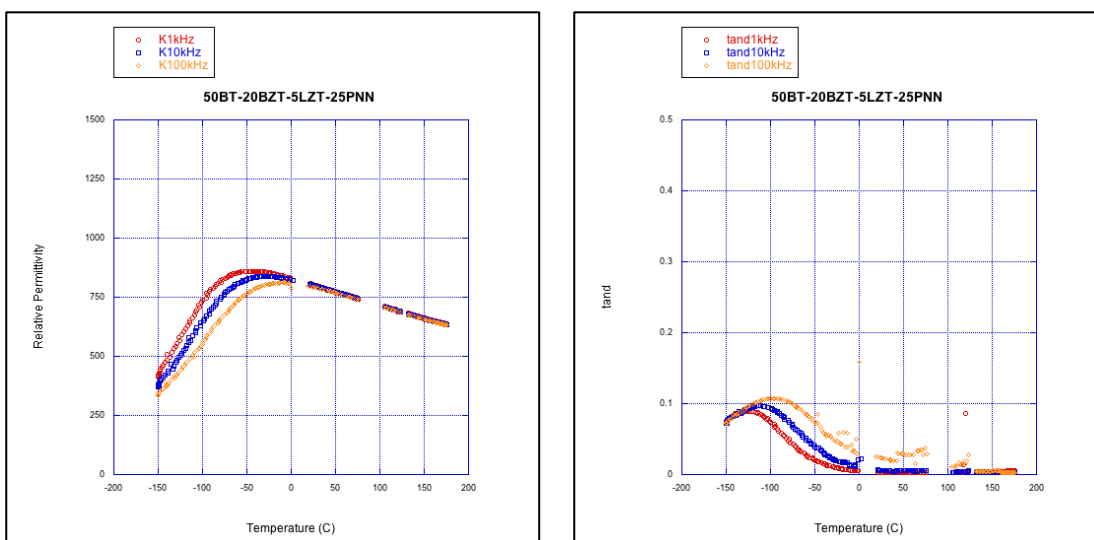


Figure 39: (a) Low temperature relative permittivity and (b) dielectric loss measurements of 50BT-20BZT-5LZT-25PNN show a T_{max} well below 0°C .

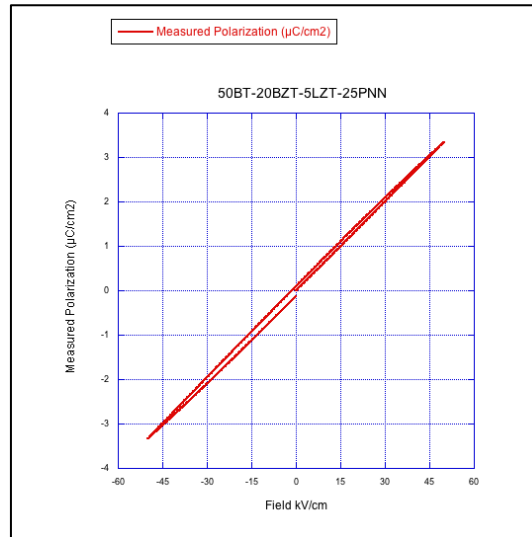


Figure 40: Polarization versus electric field measurements of 50BT-20BZT-5LZT-25PNN show a linear dielectric response.

Other compositions with 25% PNN exhibit similar properties where the maximum permittivity is below room temperature and has a linear polarization versus electric field response. Additional LZT in place of BZT does appear to significantly reduce the temperature coefficient of permittivity as previously anticipated. The 50BT-24BZT-1LZT-25PNN composition has a $TC\epsilon = 1580$ while the 50BT-15BZT-10LZT-25PNN composition has a $TC\epsilon = 1127$ as seen in Table 5.

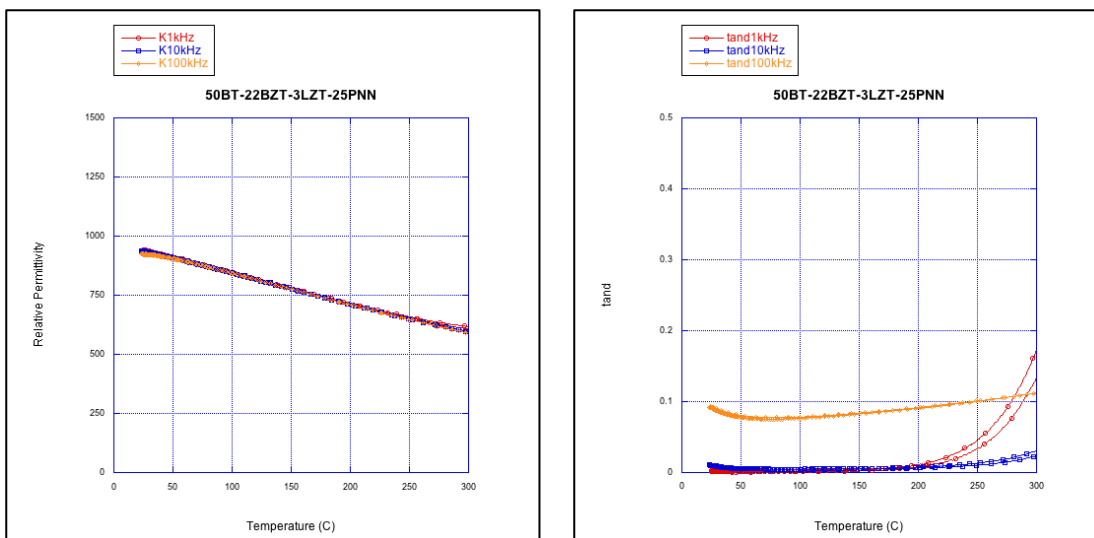


Figure 41 (a) Relative permittivity versus high temperature measurements of 50BT-24BZT-1LZT-25PNN shows a strong linear dependence while (b) dielectric loss measurements remain low at frequencies below 100kHz.

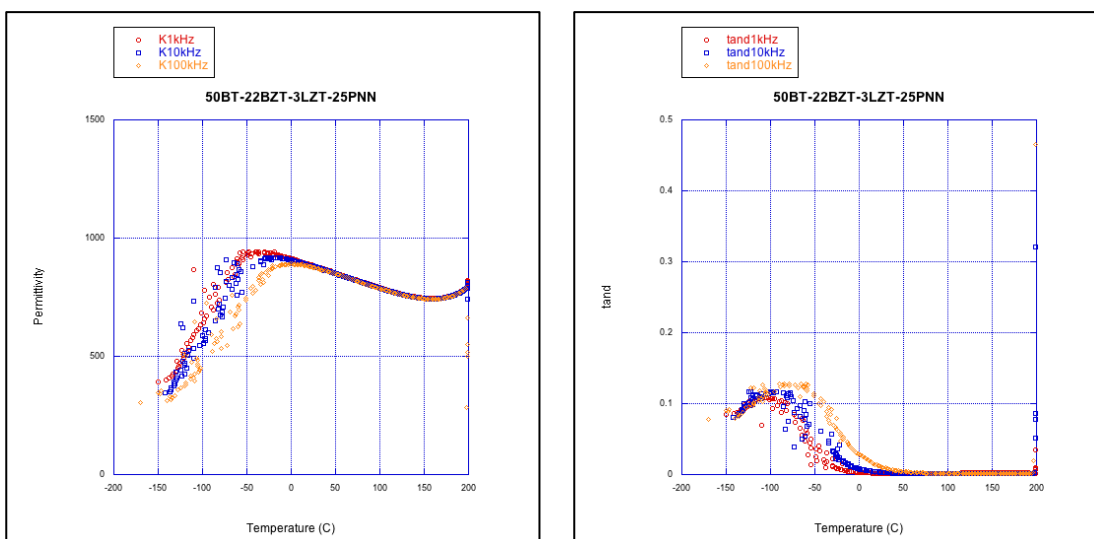


Figure 42 Low temperature (a) relative permittivity measurements of 50BT-24BZT-1LZT-25PNN show a T_{max} below 0°C and (b) low dielectric loss from the T_{max} onward.

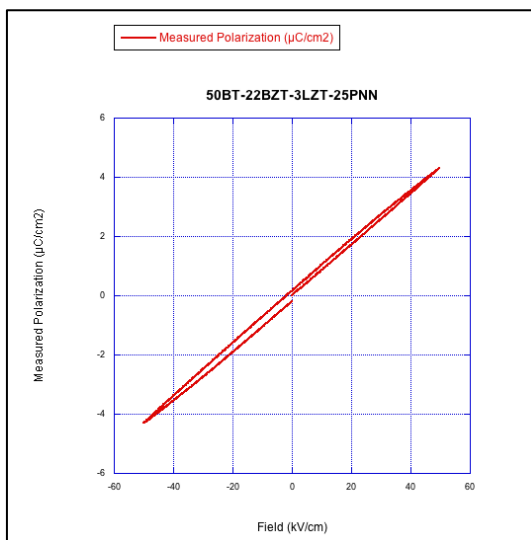


Figure 43 Polarization versus electric field measurements of 50BT-23BZT-3LZT-25PNN confirm a linear dielectric response with a dielectric strength of 50kV/cm.

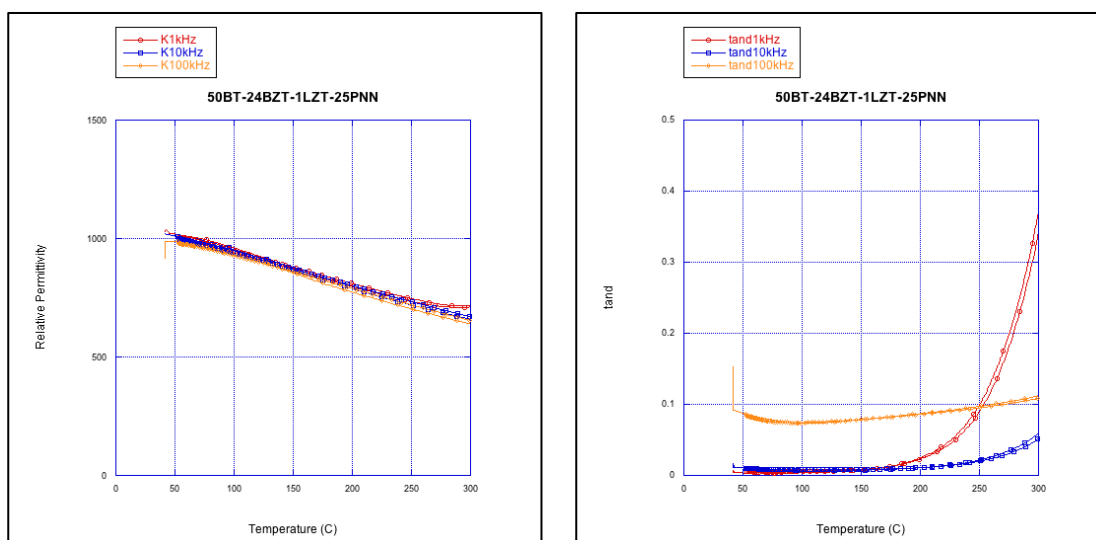


Figure 44: (a) Relative permittivity versus temperature and (b) dielectric loss versus temperature of 50BT-24BZT-1LZT-25PNN show promising results for this composition as a linear dielectric.

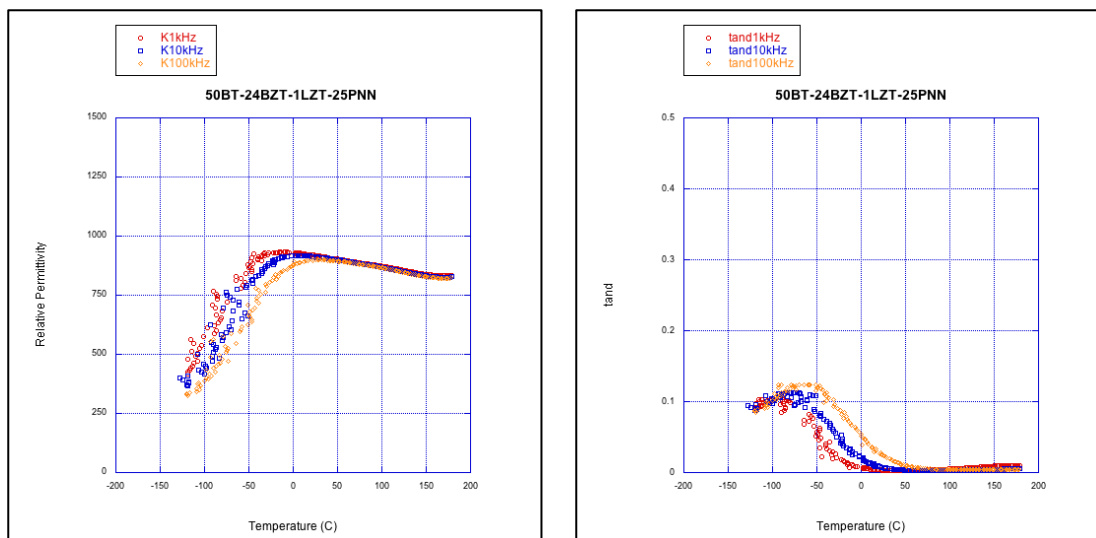


Figure 45 Low temperature permittivity and (b) dielectric loss measurements of 50BT-24BZT-1LZT-25PNN again confirm that this composition has a low TCE , T_{max} below 0°C and low loss.

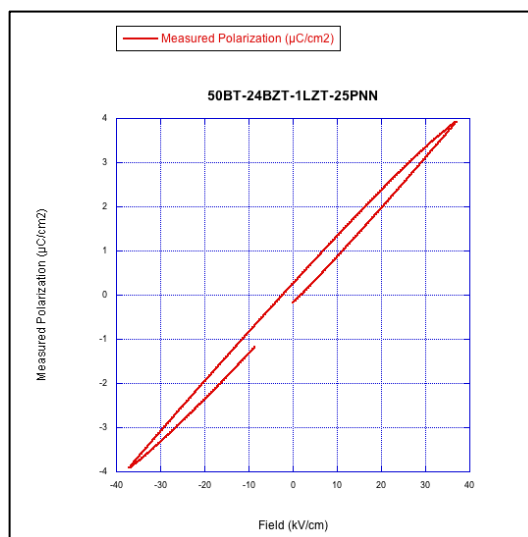


Figure 46 The polarization versus electric field measurement shows 50BT-24BZT-1LZT-25PNN has a linear dielectric response.

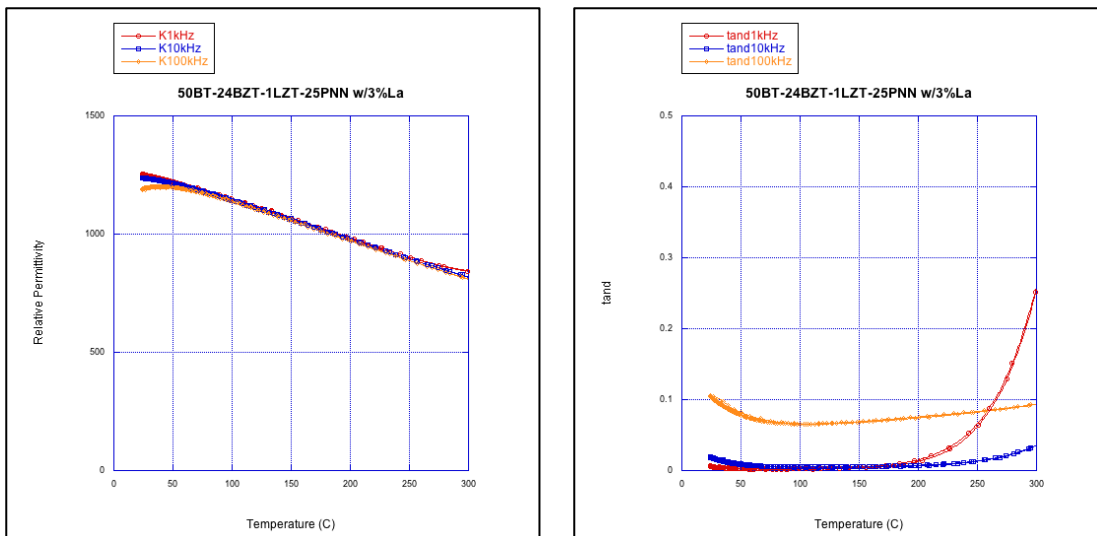


Figure 47 (a) Relative permittivity and (b) dielectric loss versus temperature of 50BT-24BZT-1LZT-25PNN with extra lanthanum shows a slight improvement in the overall relative permittivity.

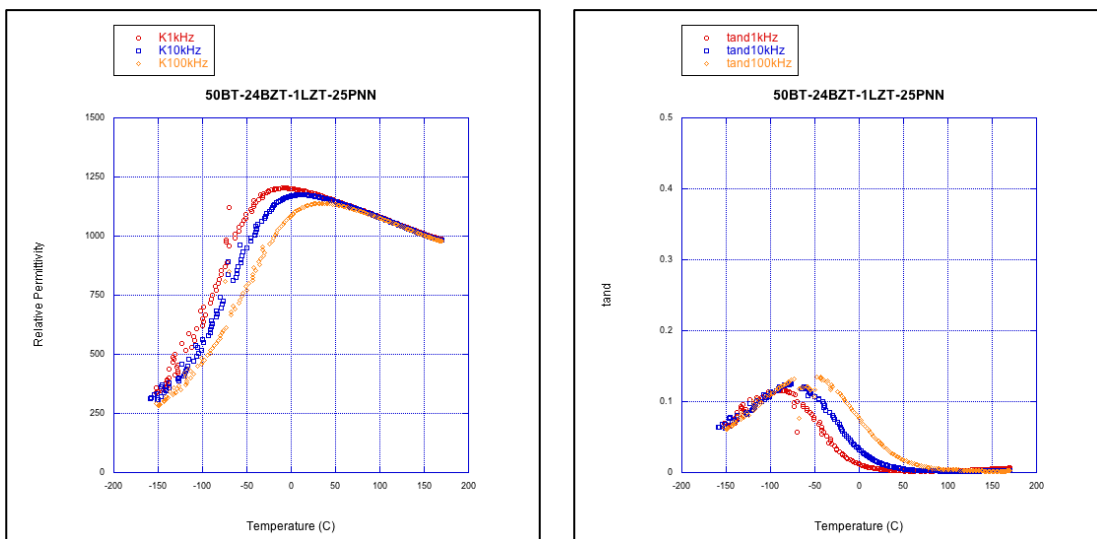


Figure 48 Low temperature measurements for (a) relative permittivity and (b) dielectric loss of 50BT-24BZT-1LZT-25PNN show this material has a T_{max} near 0°C and low loss from T_{max} on.

Similar to the previous data set, the addition of 3% excess La did not improve the overall dielectric properties.

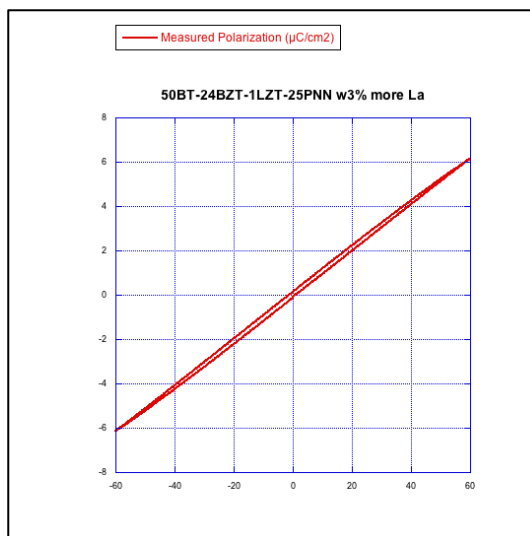


Figure 49: Polarization versus electric field measurements of 50BT-24BZT-1LZT-25PNN show this composition has a dielectric strength of 40kV/cm.

4.3.3 20% PNN System

Two compositions containing 20% PNN were prepared and both are shown to be single-phase perovskite materials through the X-ray diffraction data in figure 50.

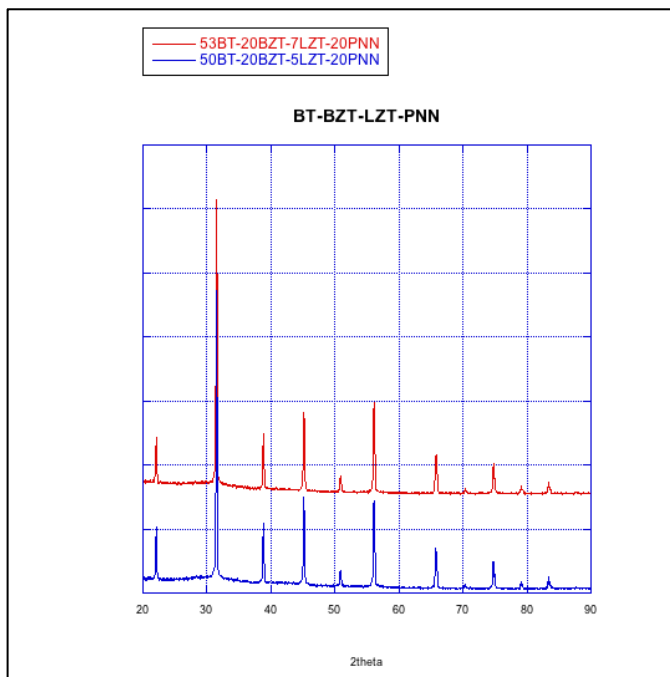


Figure 50: X-ray diffraction data for compositions containing 20% PNN.

Both 53BT-20BZT-7LZT-20PNN and 55BT-20BZT-5LZT-20PNN appear to be good candidates for linear dielectric materials. Both materials have a T_{max} below 0°C and either meet or are very close to meeting X7R capacitance specifications. The maximum permittivity for these materials is listed in table 5. but in general it is too low to justify this materials use when the $TC\epsilon \approx 1500^{\circ}\text{C}/ppm$ for each composition. Further investigation into this system could be justified if synthesis of a single phase perovskite can be achieved with higher levels of BT and LZT present.

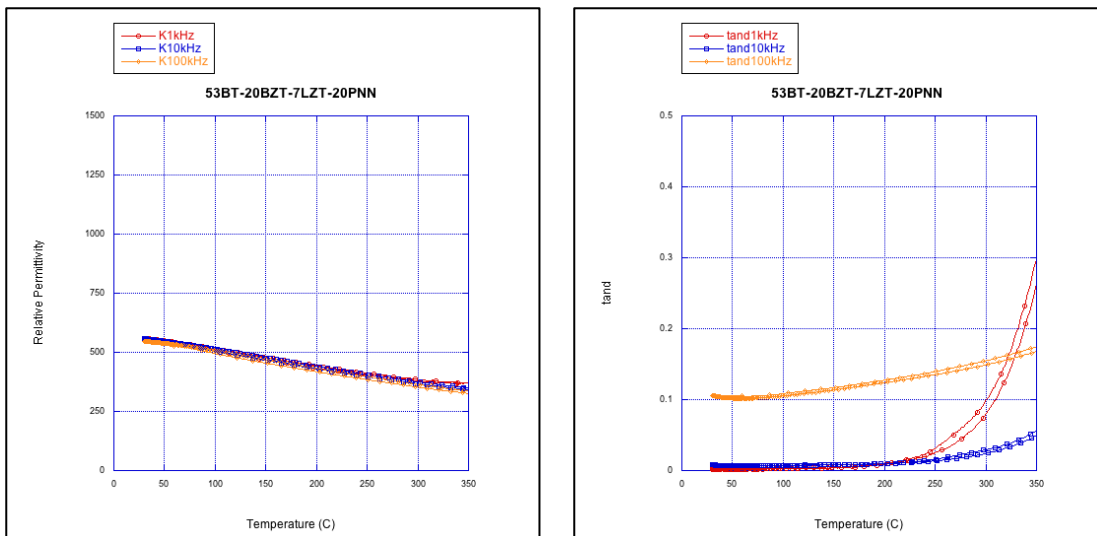


Figure 51: The high temperature (a) permittivity and (b) dielectric loss measurements of 53BT-20BZT-7LZT-20PNN show a linear dependence of permittivity with respect to temperature with low loss up to around **250°C**.

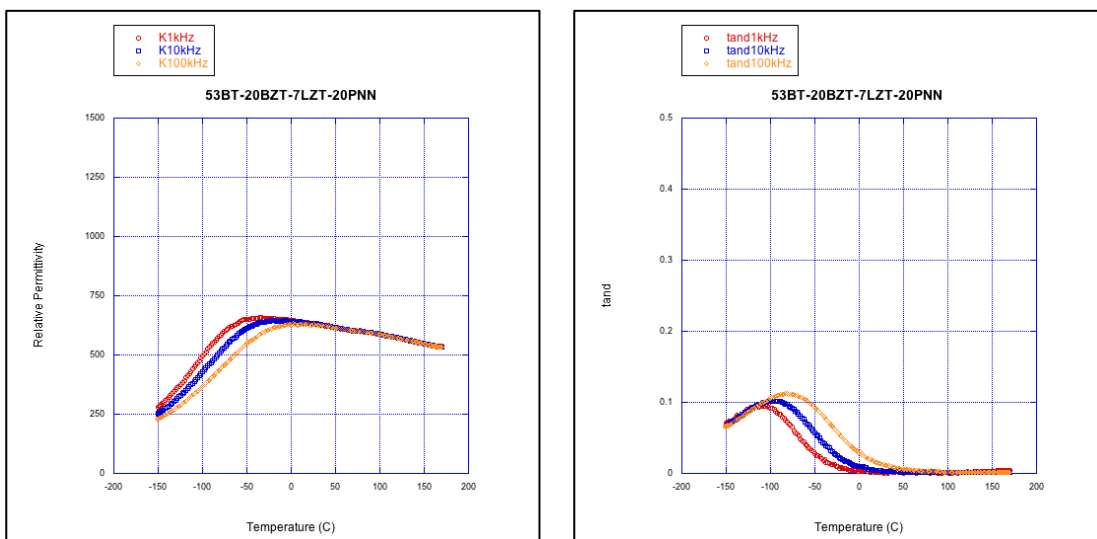


Figure 52: The (a) relative permittivity versus temperature measurement of 53BT-20BZT-7LZT-20PNN shows promising dielectric properties for the desired application while (b) show the loss remains low from around **0°C** on.

Polarization versus electric field measurements seen below in figures X and X

confirm that both compositions are linear dielectrics and can withstand fields up to 50 kV/cm.

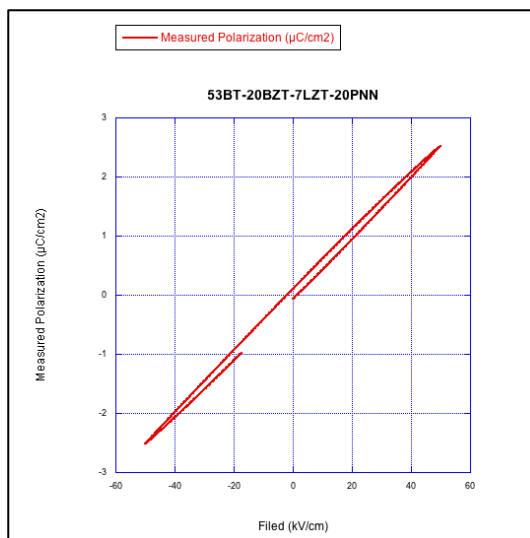


Figure 53 Polarization versus electric field measurements of 53BT-20BZT-7LZT-20PNN confirm a linear dielectric response.

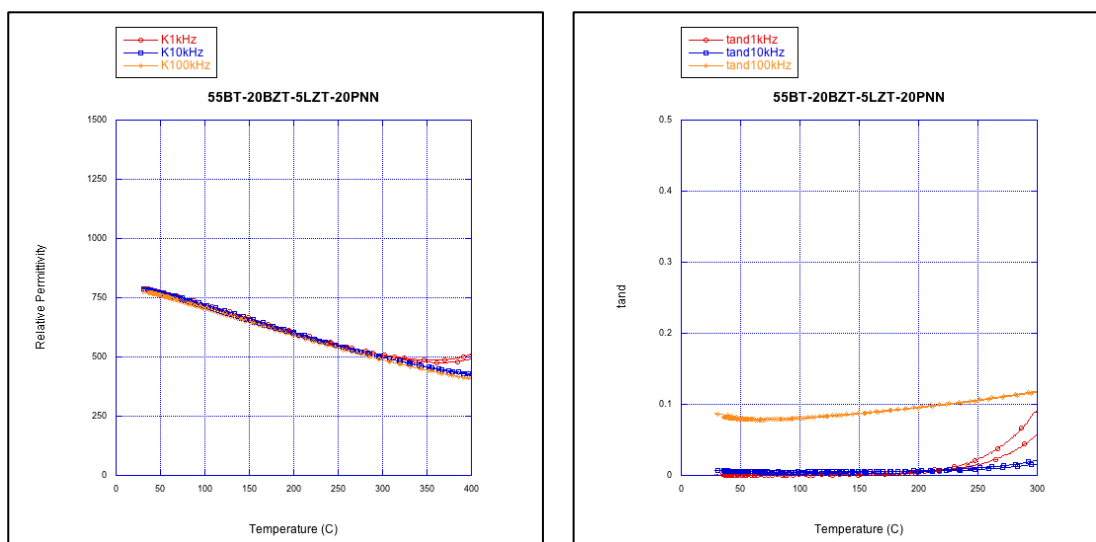


Figure 54 High temperature measurements of 55BT-20BZT-5LZT-20PNN show (a) relative permittivity's linear dependence with temperature and (b) low dielectric loss at frequencies up to 100kHz.

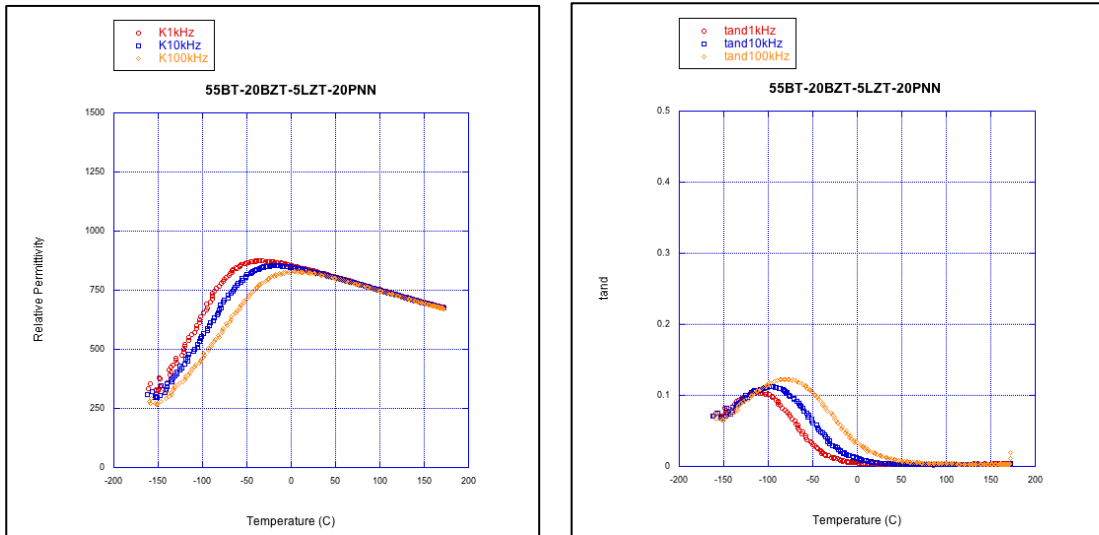


Figure 55: Low temperature measurements of 55BT-20BZT-5LZT-20PNN from -200 to 200°C show (a) a T_{max} below 0°C and (b) dielectric loss that is stable from 0°C on.

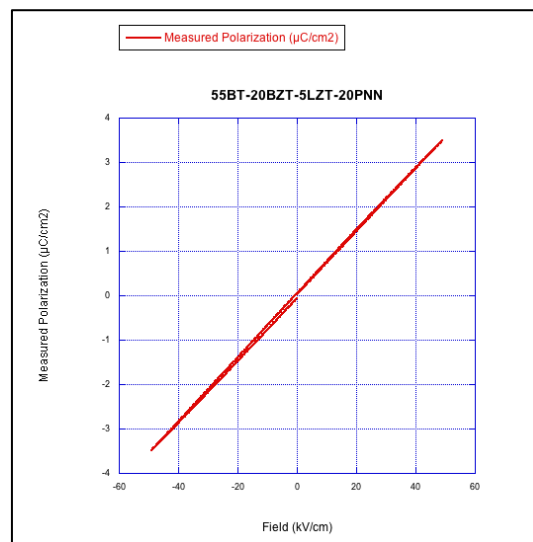


Figure 56: Polarization versus electric field measurements of 55BT-20BZT-5LZT-20PNN show a linear dielectric that can with stand an electric field up to $50\text{ kV}/\text{cm}$.

Table 5: Dielectric properties of the BT-BZT-LZT-PNN system.

Composition	$TC\epsilon_{mid}$ (ppm/°C)	$TC\epsilon_{low}$ (ppm/°C)	T_{max} (°C)	ϵ at T_{max}	X7R Capacitance Variation
45BT-20BZT-5LZT-30PNN	-1007	-	34.3	569	-
45BT-22BZT-3LZT-30PNN	-	-	-	-	-
45BT-24BZT-1LZT-30PNN	-1626	3716	-9.9	473.7	5.60%
45BT-24BZT-1LZT-30PNN 3% La	-614	-	24.5	346	
50BT-15BZT-10LZT-25PNN	-1127	1350	-54.4	556	16.10%
50BT-20BZT-5LZT-25PNN	-1575	5433	-28.8	838	18.70%
50BT-22BZT-3LZT-25PNN	-2272	7643	-27	918	17.80%
50BT-24BZT-1LZT-25PNN	-1580	6950	2.9	918	14.60%
50BT-24BZT-1LZT-25PNN 3% La	-1417	-	24.7	1234	-
53BT-20BZT-7LZT-20PNN	-1445	5344	-7.8	645	12.10%
55BT-20BZT-5LZT-20PNN	-1607	6541	-18.4	853	15.80%

4.4 $PbTiO_3 - Pb\left(Ni_{\frac{1}{3}}Nb_{\frac{2}{3}}\right)O_3 - Bi\left(Zn_{\frac{1}{2}}Ti_{\frac{1}{2}}\right)O_3 - NaNbO_3$ System

X-ray diffraction data on the PT-PNN-BZT-NN system shows peak splitting on all compositions at room temperature. Indicating a unique c/a ratio and tetragonal symmetry for all compositions within this family.

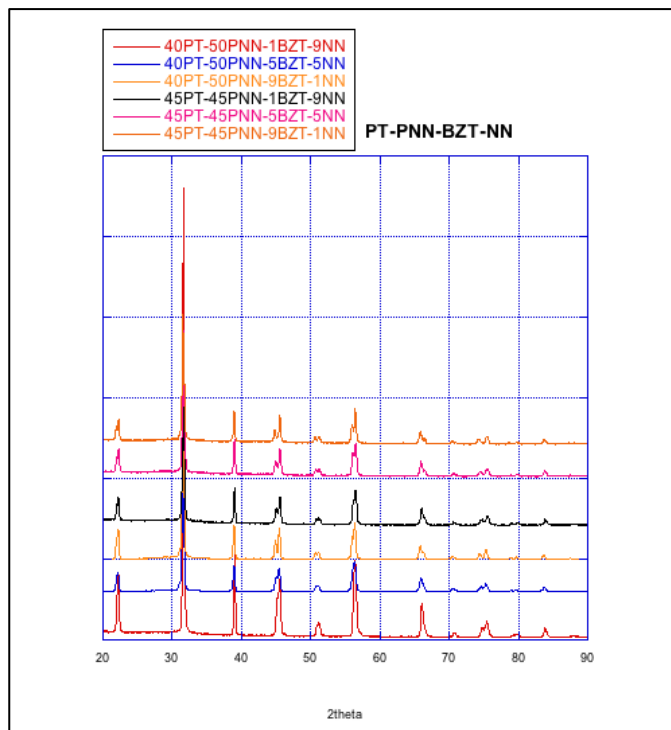


Figure 57: X-ray diffraction data for the PT-PNN-BZT-NN system shows some peak splitting indicating a unique c/a lattice constant ratio.

Table 6: Physical property measurements of the PT-PNN-BZT-NN system.

Composition	Lattice Parameter (Å)	Geometric Density(g/cm ³)	Theoretical Density(g/cm ³)	Tolerance Factor
40PT-50PNN-1BZT-9NN		5.686		0.9925
40PT-50PNN-5BZT-5NN		7.540		0.9919
40PT-50PNN-9BZT-1NN		7.139		0.9913
45PT-45PNN-1BZT-9NN				0.9944
45PT-45PNN-5BZT-5NN		6.124		0.9939
45PT-45PNN-9BZT-1NN		6.914		0.9933

Dielectric characterization on the PT-PNN-BZT-NN family of compositions reveals that the relative permittivity has a strong temperature dependence despite the low dielectric loss from -150°C to 300°C . The 40PT-50PNN-1BZT-9NN composition also has a maximum permittivity at $T_{max} = 119^{\circ}\text{C}$ which is well out of the required specification for this project. This composition shows some frequency dependence with relative permittivity decreasing with increasing frequency.

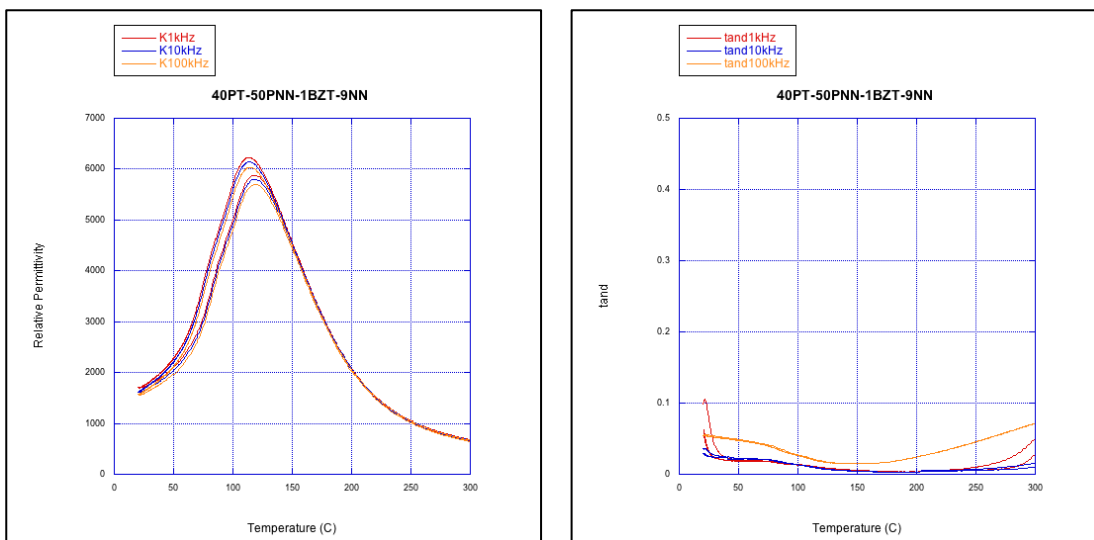


Figure 58 (a) Relative permittivity and (b) dielectric loss versus temperature plots of 40PT-50PNN-5BZT-5NN show a T_{max} well above room temperature with high $TC\epsilon$.

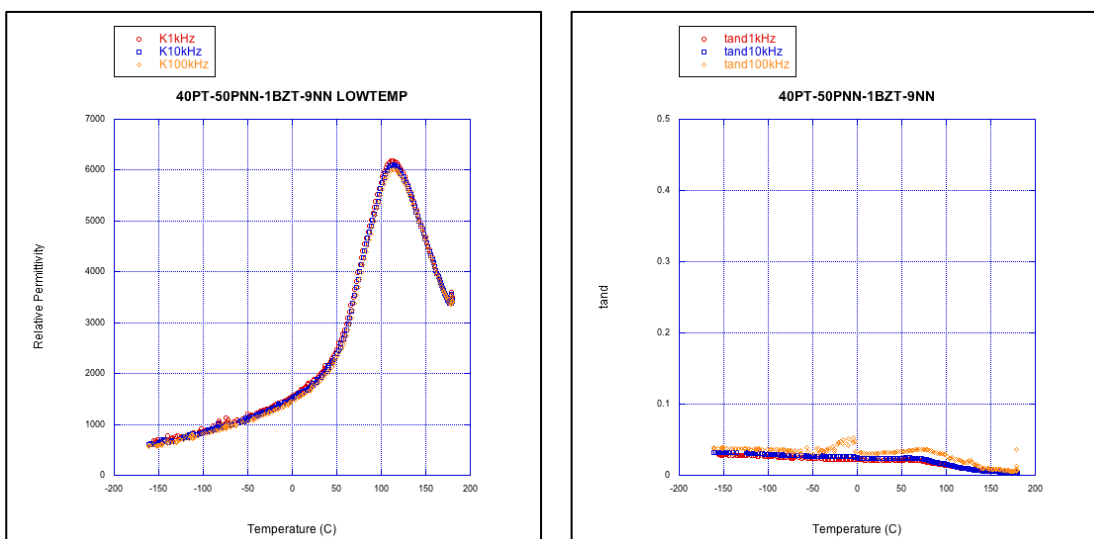


Figure 59: Low temperature data confirms of the 40PT-50PNN-1BZT-9NN compositions confirms (a) the same relative permittivity curve and (b) low dielectric loss across all temperatures.

Polarization versus electric field measurements show that the 40PT-50PNN-1BZT-9NN composition is a ferroelectric which requires a coercive field to be applied to the material to return it to a polarization of zero. Meaning all of the compositions within the PT-PNN-BZT-NN family explored are not relevant for the purposes of this study.

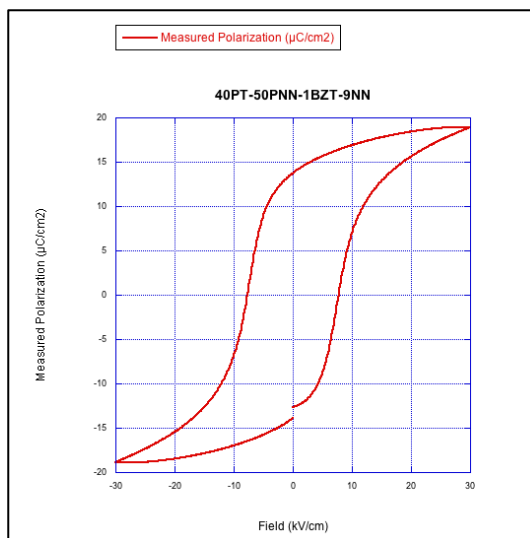


Figure 60: The polarization versus electric field measurement 40PT-50PNN-1BZT-9NN shows this material has a hysteresis and requires a coercive field to return the material to zero polarization.

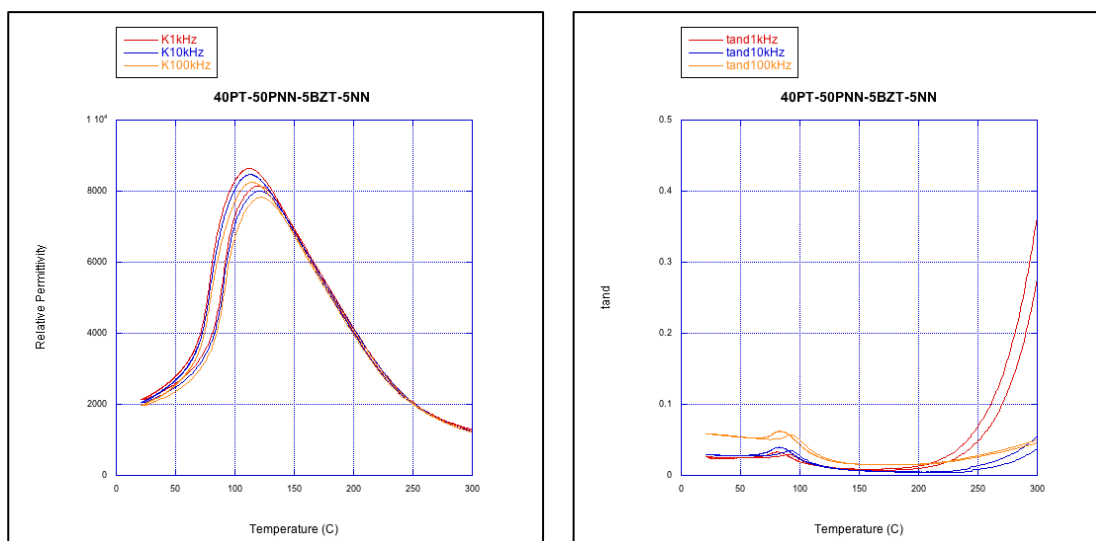


Figure 61: The (a) relative permittivity versus temperature data of 40PT-50PNN-5BZT-5NN shows another T_{max} well above room temperature but also shows a strong dependence on the frequency with lower frequencies having higher permittivity's. (b) shows the dielectric loss versus temperature data for this composition.

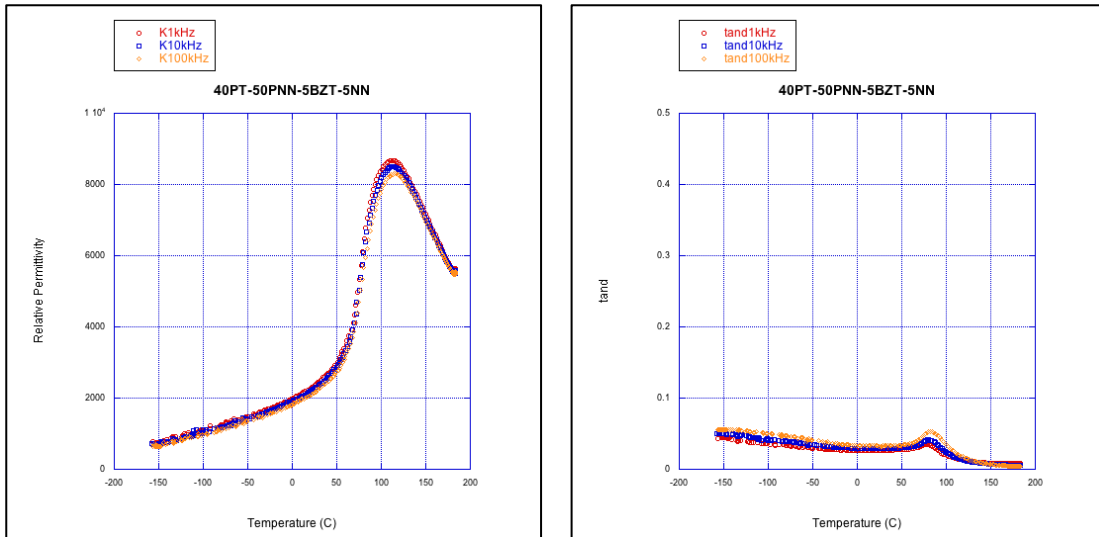


Figure 62: Low temperature measurements of 40PT-50PNN-5BZT-5NN show the frequency dependence of the permittivity exists mostly around the curie temperature.

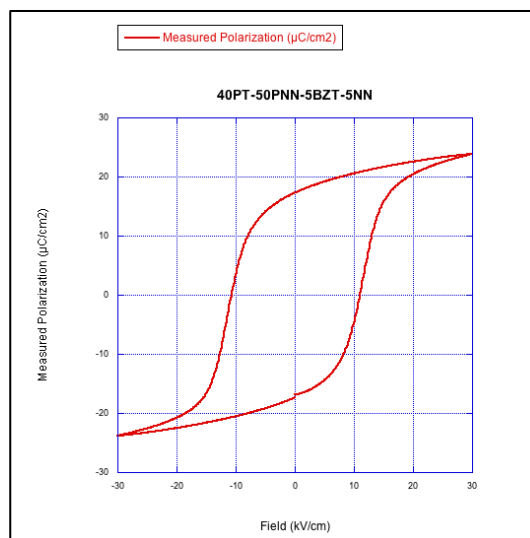


Figure 63: Polarization versus electric field measurements of 40PT-50PNN-5BZT-5NN show another ferroelectric response.

The 40PT-50PNN-9BZT-1NN composition shows similar results to the first two materials presented in this section but with the dielectric loss spiking at a lower temperature of 150°C. This results in a polarization versus electric field loop that begins to round at the corners instead of having a clearly defined saturation polarization value.

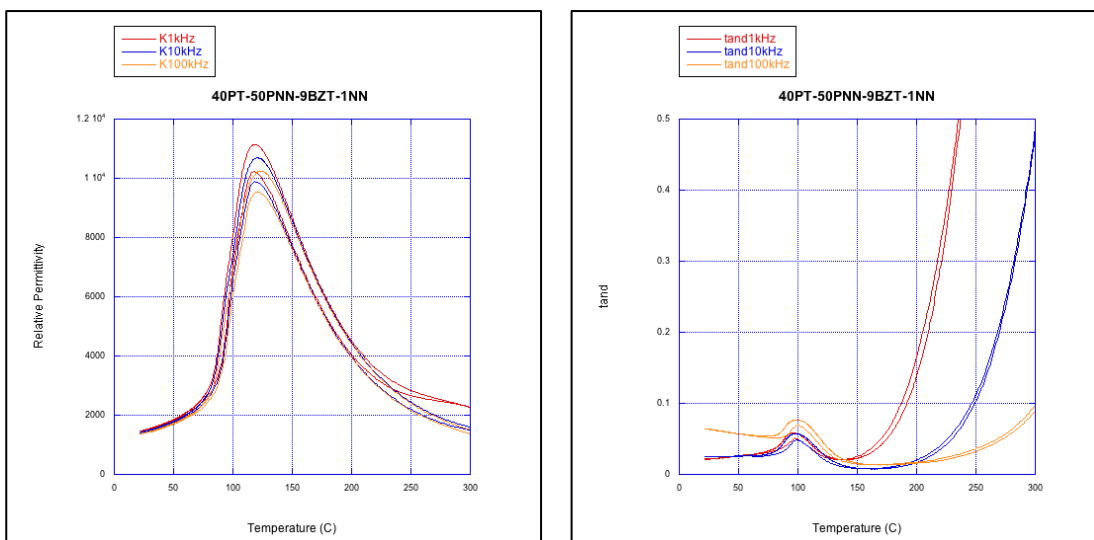


Figure 64 (a) Relative permittivity and (b) dielectric loss plots of 40PT-50PNN-9BZT-1NN.

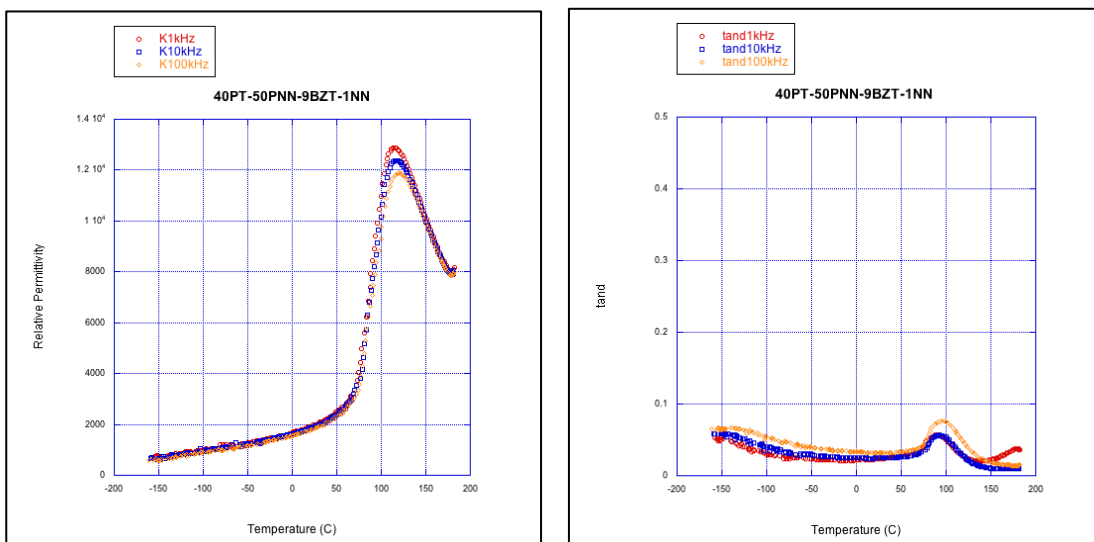


Figure 65: (a) Low temperature permittivity measurements of 40PT-50PNN-9BZT-1NN show the same frequency dependance with lower frequencies having higher permittivity. (b) The dielectric loss remains very close to 0.05 from -150 to 200°C .

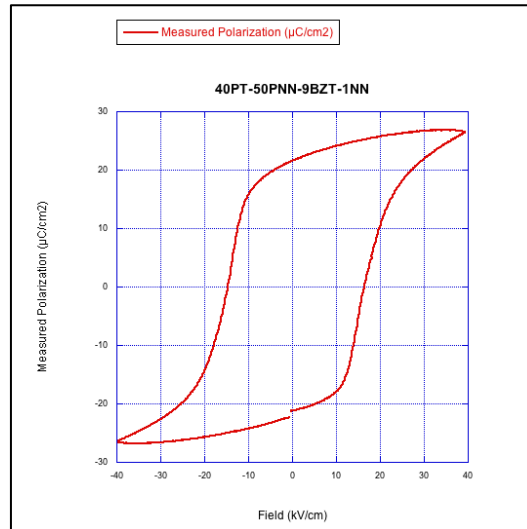


Figure 66: The polarization versus electric field measurement of 40PT-50PNN-9BZT-1NN confirms this material is a ferroelectric.

Increasing the amount of PT in the composition to 45% shows a clear increase in the T_{max} to at least 166°C for all three compositions. Also observed is a small decrease in the relative permittivity at the T_{max} when compared to the similar composition with 40% PT. As the amount of NN decreases with each composition the $TC\epsilon$ increases along with the permittivity at T_{max} . However, the relative amount of lead in all of these compositions is far too much to be anywhere close to a linear dielectric and increasing the amount of NN can result in a lossy dielectric.

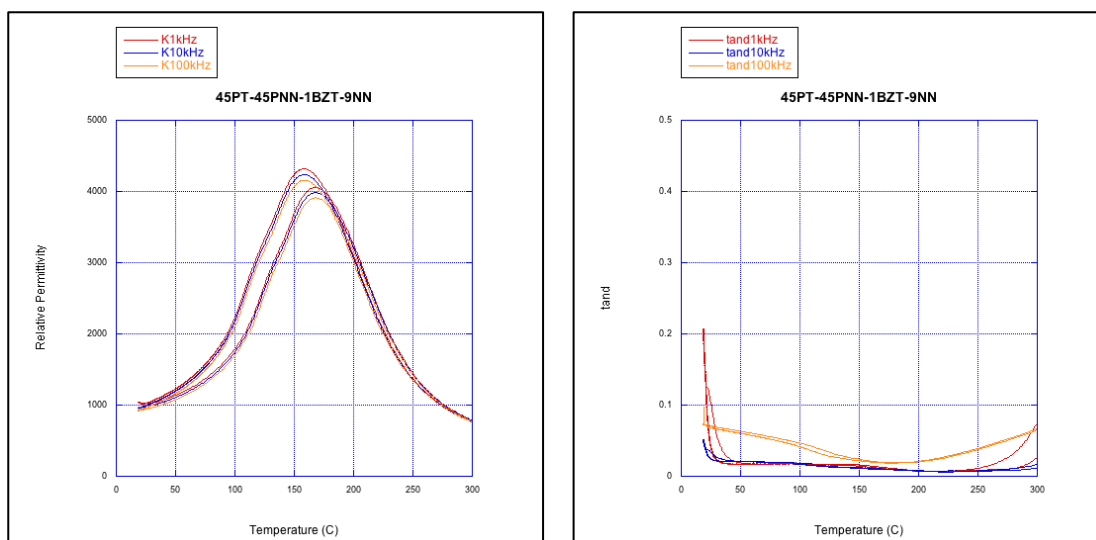


Figure 67: (a) Relative permittivity and (b) dielectric loss plots for 45PT-45PNN-1BZT-9NN from 25 – 300°C.

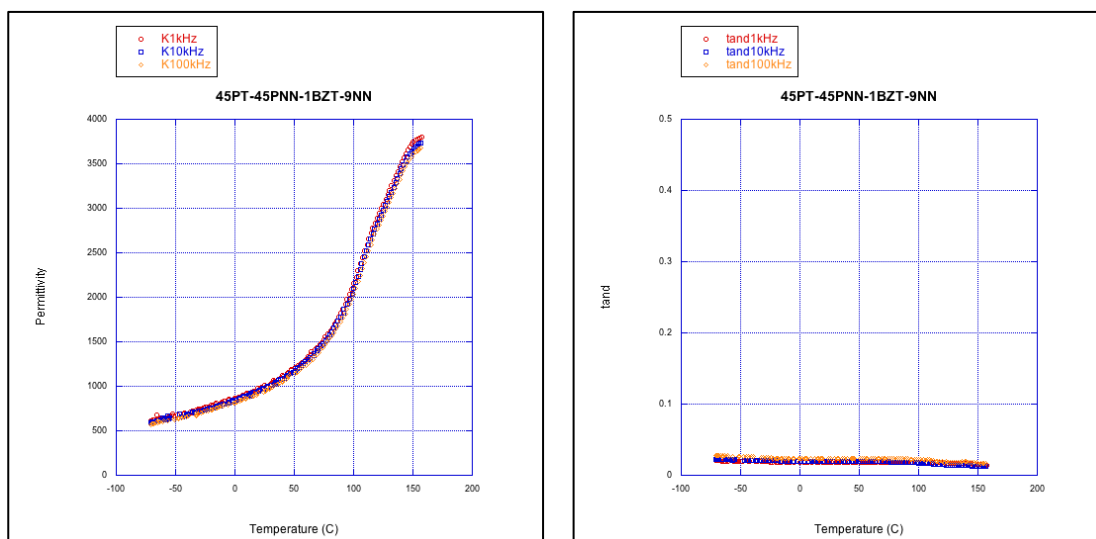


Figure 68: (a) Low temperature permittivity and (b) dielectric loss for 45PT-45PNN-1BZT-9NN.

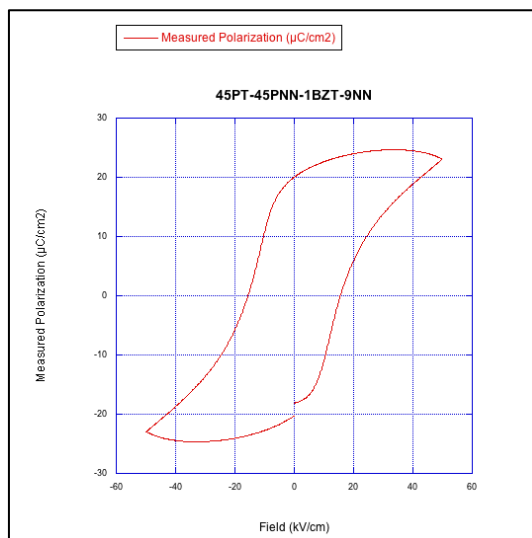


Figure 69 Polarization versus electric field measurement of 45PT-45PNN-1BZT-9NN shows a deteriorated ferroelectric hysteresis loop.

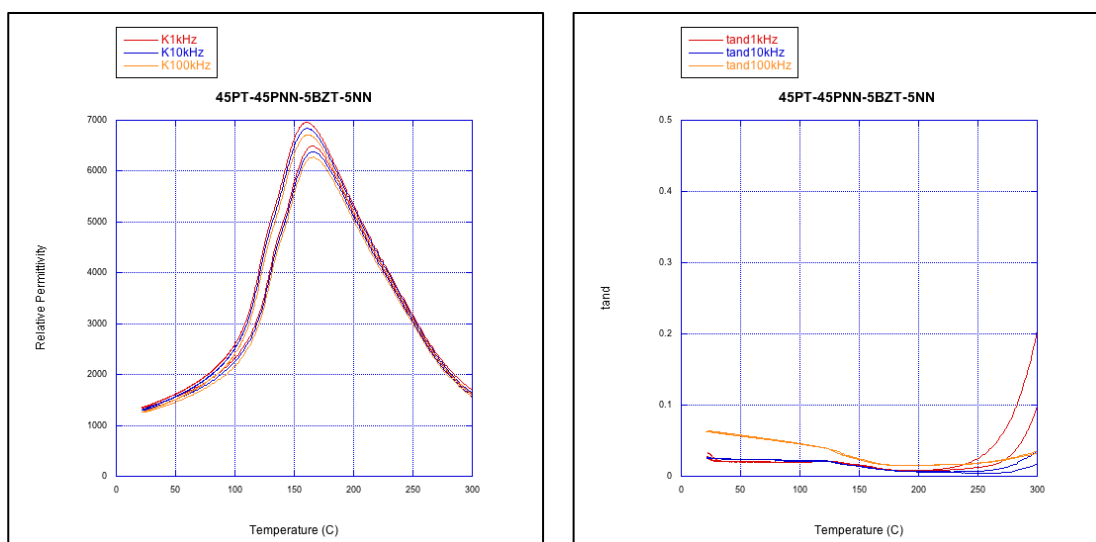


Figure 70: (a) The relative permittivity and (b) dielectric loss of 45PT-45PNN-5BZT-5NN show the same frequency dependency of permittivity as previous compositions.

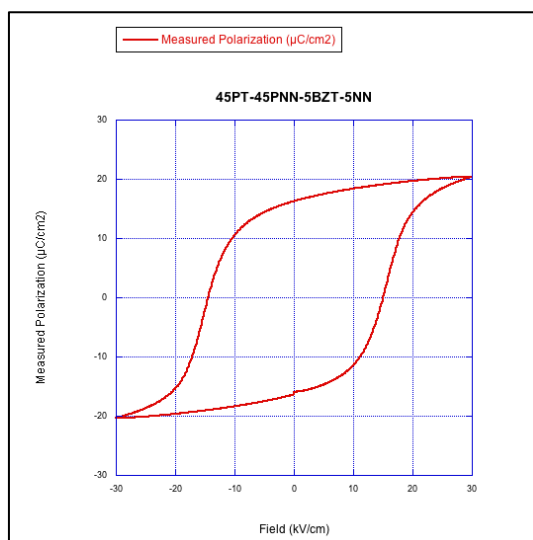


Figure 71 The polarization versus electric field measurements of 45PT-45PNN-5BZT-5NN show a ferroelectric hysteresis loop with poor dielectric strength.

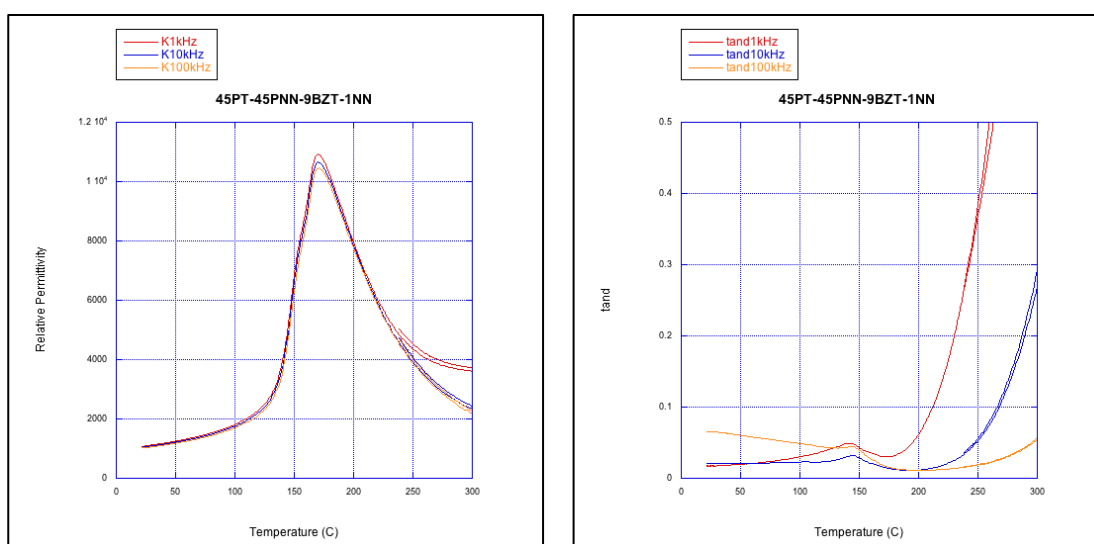


Figure 72: (a) Relative permittivity and (b) dielectric loss of 45PT-45PNN-9BZT-1NN from 25 – 300°C.

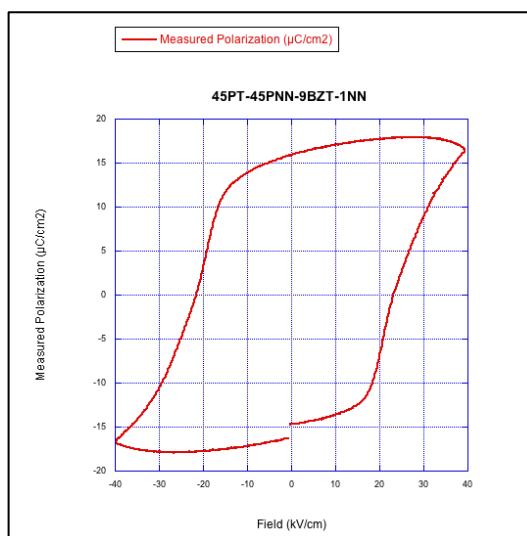


Figure 73: The polarization versus electric field measurement of 45PT-45PNN-9BZT-1NN shows a deteriorated ferroelectric hysteresis loop.

Table 7: Dielectric properties of the PT-PNN-BZT-NN system.

Composition	TCE_{mid} (ppm/°C)	TCE_{low} (ppm/°C)	T_{max} (°C)	ϵ at T_{max}	X7R Capacitance Variation
40PT-50PNN-1BZT-9NN	-10185	15769	119	5800	259%
40PT-50PNN-5BZT-5NN	-7639	8026	120.8	7607	308%
40PT-50PNN-9BZT-1NN	11301	33767	116.3	12386	590%
45PT-45PNN-1BZT-9NN	-9529	11992	168	3984	317%
45PT-45PNN-5BZT-5NN	-8722	15122	166	6384	-
45PT-45PNN-9BZT-1NN	-11301	29517	170	10658	-

4.5 $PbTiO_3 - Pb\left(Ni_{\frac{1}{3}}Nb_{\frac{2}{3}}\right)O_3 - NaNbO_3$ System

X-ray diffraction data for the PT-PNN-NN system shows a pseudo cubic phase with some slight peak splitting on the (100) and (200) planes. The diffraction data for each composition can be seen in figure 74 below.

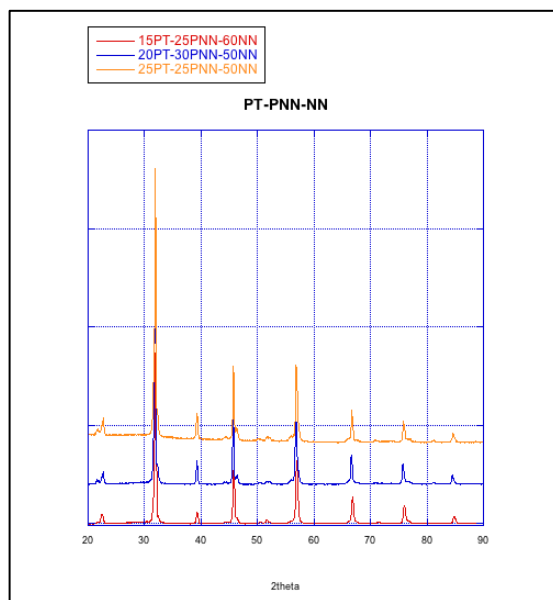


Figure 74: X-ray diffraction data for the PT-PNN-NN system shows some slight peak splitting on the (100) and (200) planes.

Table 8: Physical properties of the PT-PNN-NN system.

Composition	Lattice Parameter (Å)	Geometric Density(g/cm ³)	Theoretical Density(g/cm ³)	Tolerance Factor
15PT-25PNN-60NN		4.910		0.967
20PT-30PNN-50NN		4.767		0.972
25PT-25PNN-50NN		4.888		0.974

High temperature dielectric measurements show the 15PT-25PNN-60NN composition has high dielectric loss at low and high temperatures. While the temperature of maximum permittivity exists below room temperature the temperature

coefficient of capacitance is too large to consider this a possible material for temperature stable capacitor applications.

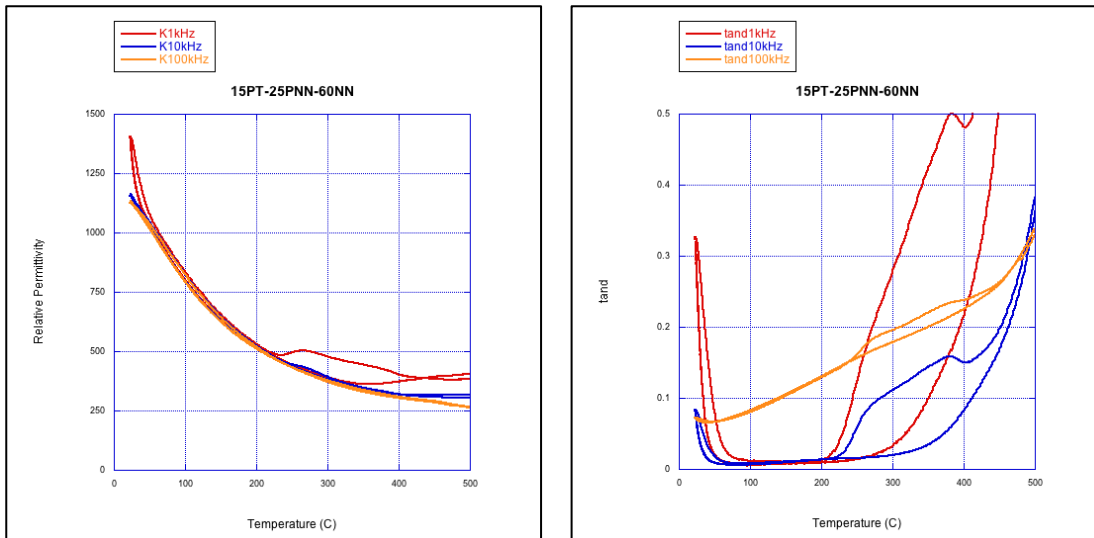


Figure 75: (a) Relative permittivity and (b) dielectric loss of 15PT-25PNN-60NN shows high losses at all temperatures outside of **100 – 200°C**.

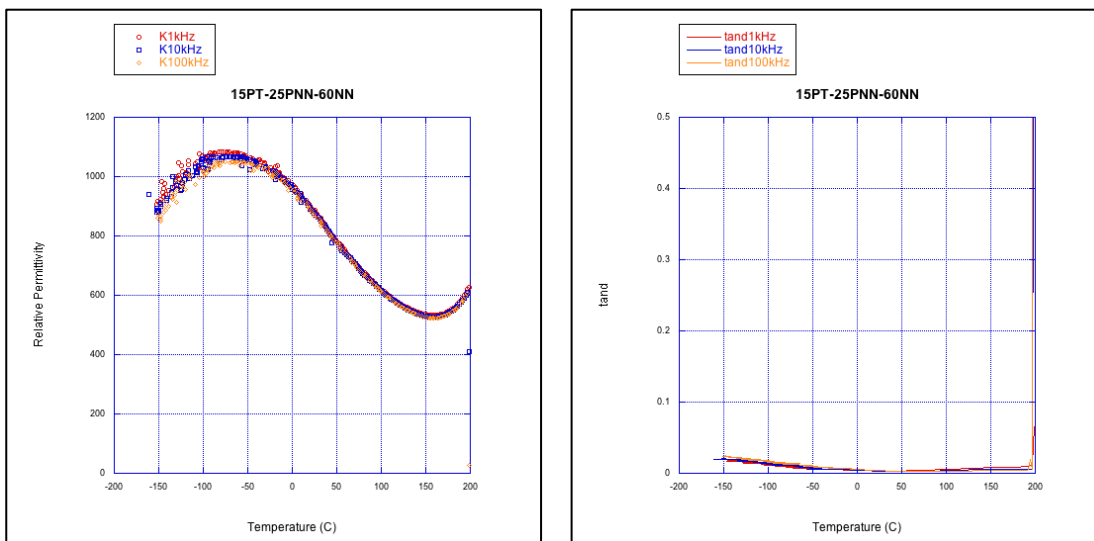


Figure 76: (a) The low temperature permittivity data of 15PT-25PNN-60NN shows a T_{max} below **0°C** and (b) shows low dielectric loss data across **-150 – 200°C**.

As suspected from the high dielectric loss levels the polarization versus electric field measurements show a linear dielectric material with high levels of dielectric loss as was previously depicted in figure 3.

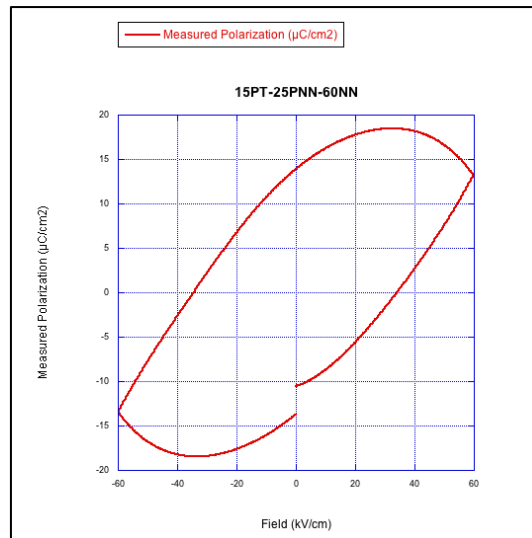


Figure 77: Polarization versus electric field data of 15PT-25PNN-60NN shows a deteriorated linear dielectric response.

Changing the composition to include more PT and PNN curiously decreases the maximum permittivity by a factor of three for the 10 kHz measurement. While the temperature coefficient of permittivity does decrease from the previous composition it is still too high to be considered for any further investigation. The polarization versus electric field measurements once again confirm a linear dielectric with high dielectric loss.

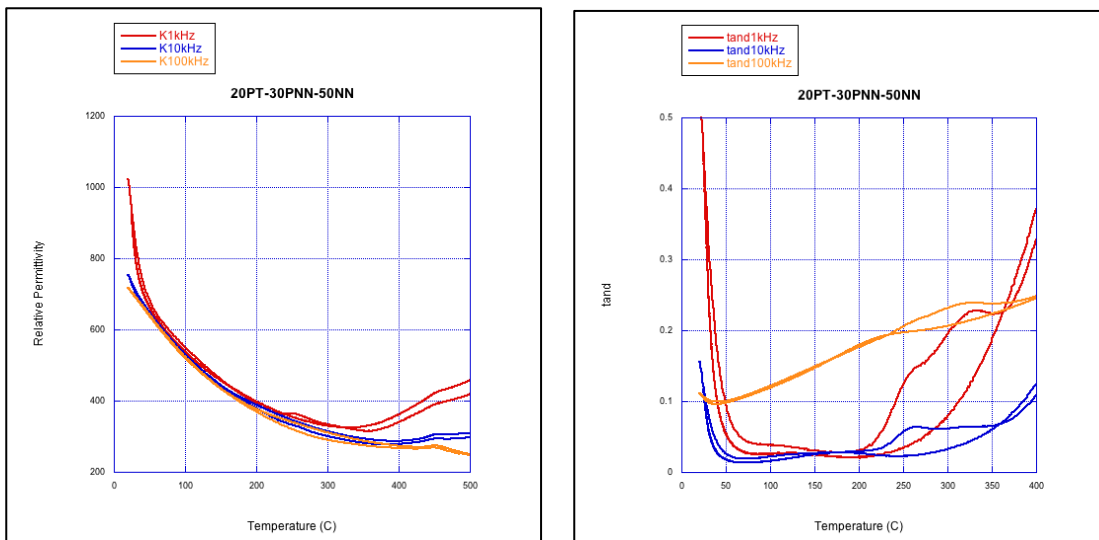


Figure 78: (a) The relative permittivity and (b) dielectric loss of 20PT-30PNN-50NN shows a decrease in the permittivity compared to the 15PT-25PNN-60NN composition.

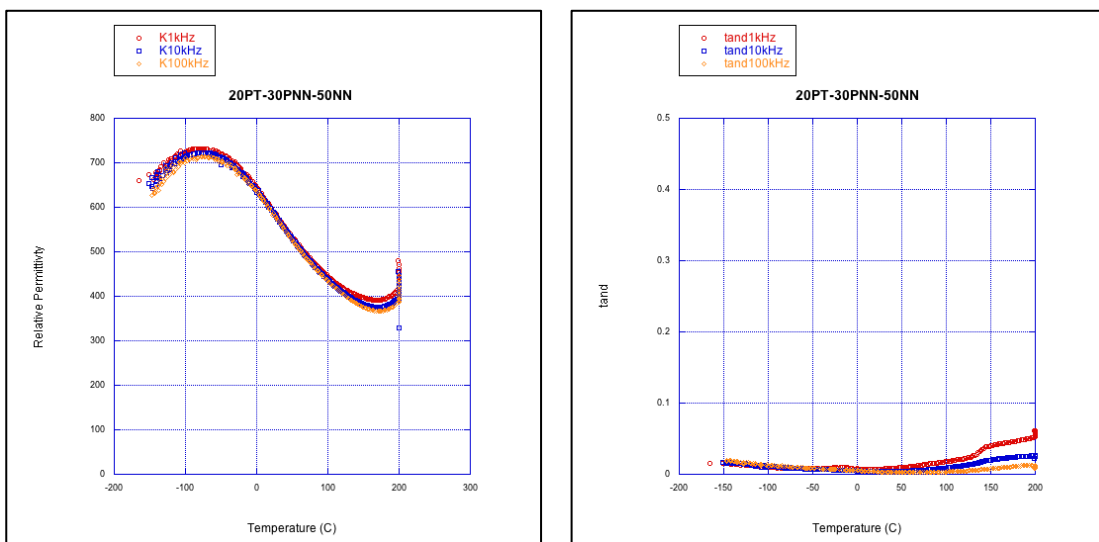


Figure 79: (a) Low temperature relative permittivity and (b) dielectric loss of 20PT-30PNN-50NN shows a T_{max} below room temperature and a stable dielectric loss.

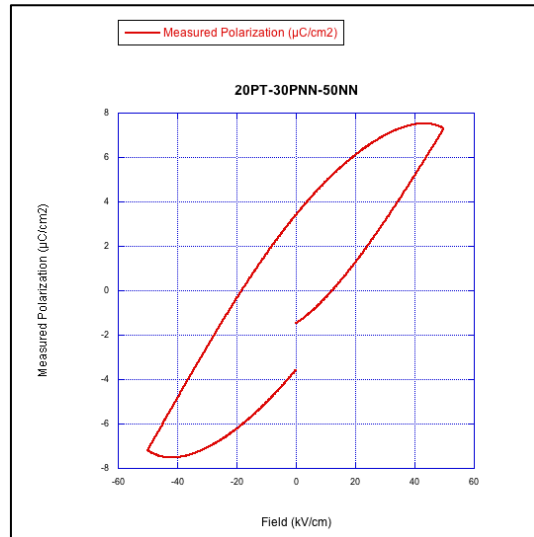


Figure 80: The polarization versus electric field of 20PT-30PNN-50NN shows a deteriorated linear dielectric response.

Evening out the relative amounts of PT and PNN did help to improve the maximum relative permittivity while also decreasing the temperature of maximum permittivity. However, overall this material still has high dielectric loss values and does not come close to meeting X7R capacitor specifications. Further investigation of the PT-PNN-NN compositions is not necessary due to all polarization versus electric field measurements showing signs of linear dielectrics with high loss values.

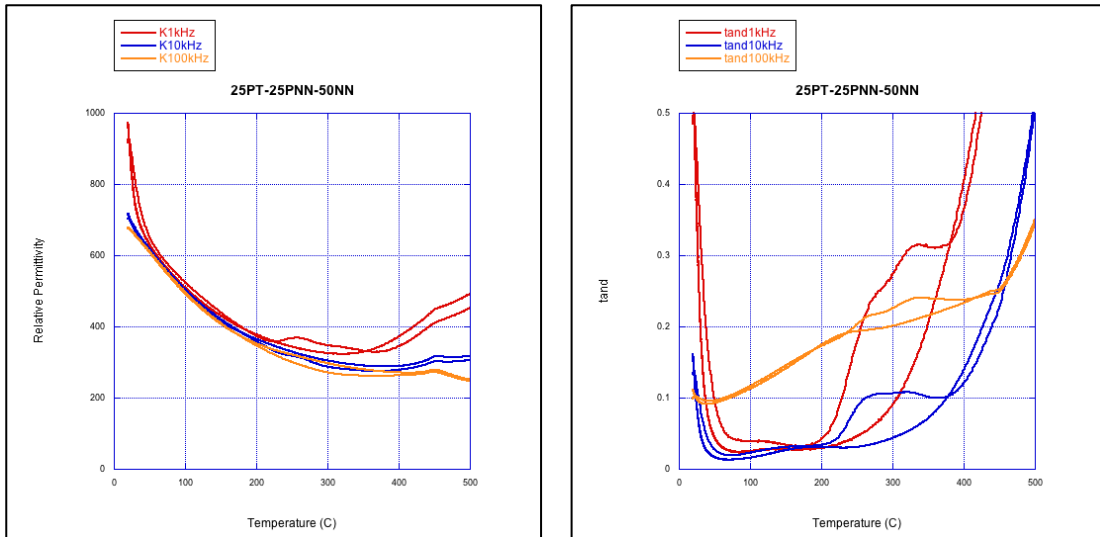


Figure 81: (a) Relative permittivity and (b) dielectric loss measurements of 25PT-25PNN-50NN shows undesirable levels across nearly all temperatures.

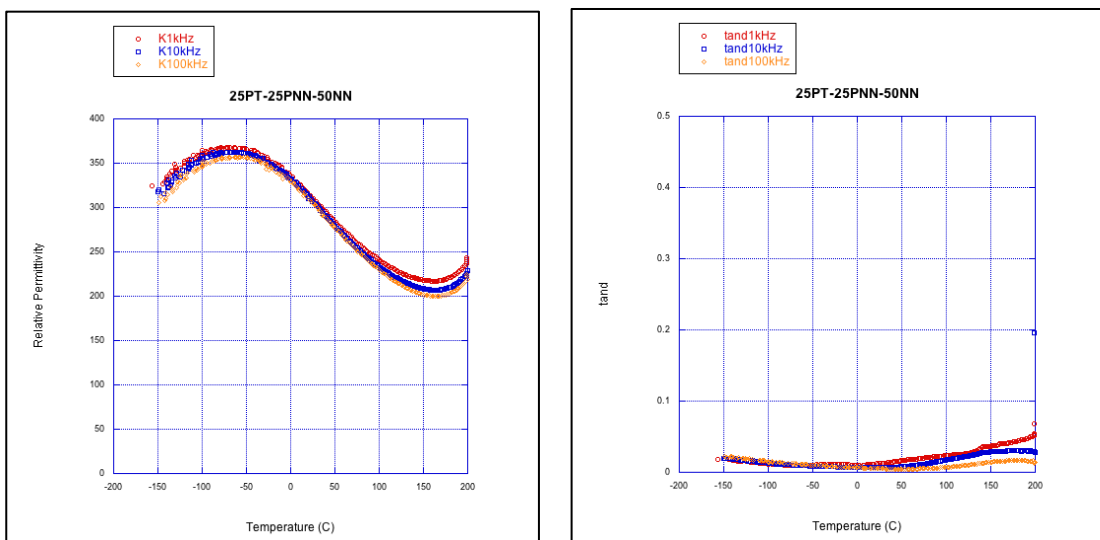


Figure 82: (a) Low temperature relative permittivity measurements of 25PT-25PNN-50NN and (b) dielectric loss measurements show a T_{max} below 0°C acceptable levels of loss.

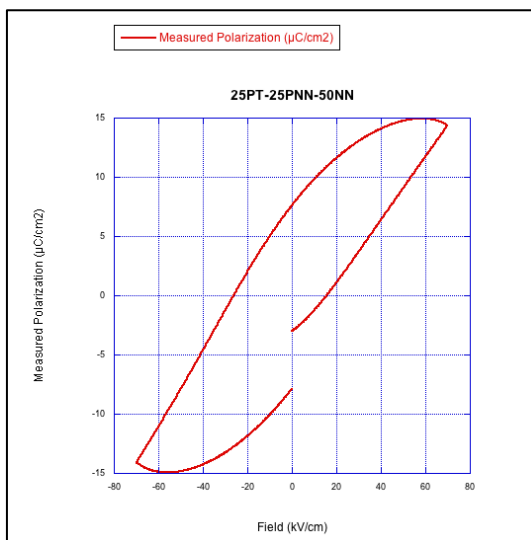
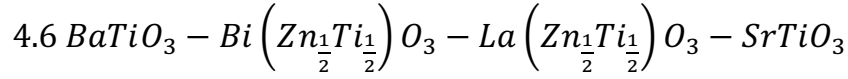


Figure 83: The polarization versus electric field measurement of 25PT-25PNN-50NN show a deteriorated linear dielectric response.

Table 9: Dielectric properties of the PT-PNN-NN system

Composition	TCE_{mid} (ppm/°C)	TCE_{low} (ppm/°C)	T_{max} (°C)	ϵ at T_{max}	X7R Capacitance Variation
15PT-25PNN-60NN	-2858	2355	-71.2	1067.2	57%
20PT-30PNN-50NN	-2399	1470	-63.3	362.4	26%
25PT-25PNN-50NN	-2542	1612	-81.2	722.8	52%



Finally the BT-BZT-LZT-ST system is explored and x-ray diffraction data shows this material has a perovskite phase with small secondary peak right at 30° .

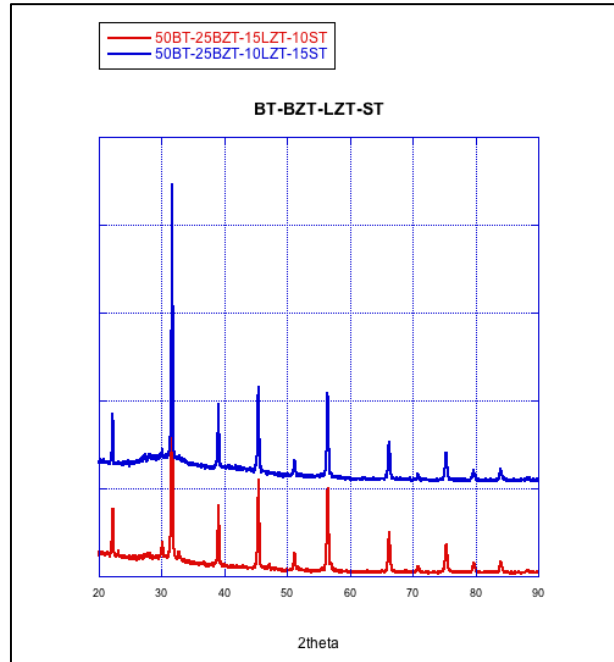


Figure 84: The X-ray diffraction data shows the perovskite structure with a minor additional peak around 30° .

Table 10: The physical properties of the BT-BZT-LZT-ST system.

Composition	Lattice Parameter (\AA)	Geometric Density(g/cm^3)	Theoretical Density(g/cm^3)	Tolerance Factor
50BT-25BZT-15LZT-10ST	3.978	5.265	6.532	1.009
50BT-25BZT-10LZT-15ST	3.988	5.740	6.562	1.006

Dielectric characterization measurements of the 50BT-25BZT-10LZT-15ST composition show a maximum relative permittivity of 667 and a T_{max} below room temperature. The temperature coefficient of permittivity for this material is -885°C/ppm above T_{max} and dielectric loss remains low for all temperatures except at extreme high and low temperatures.

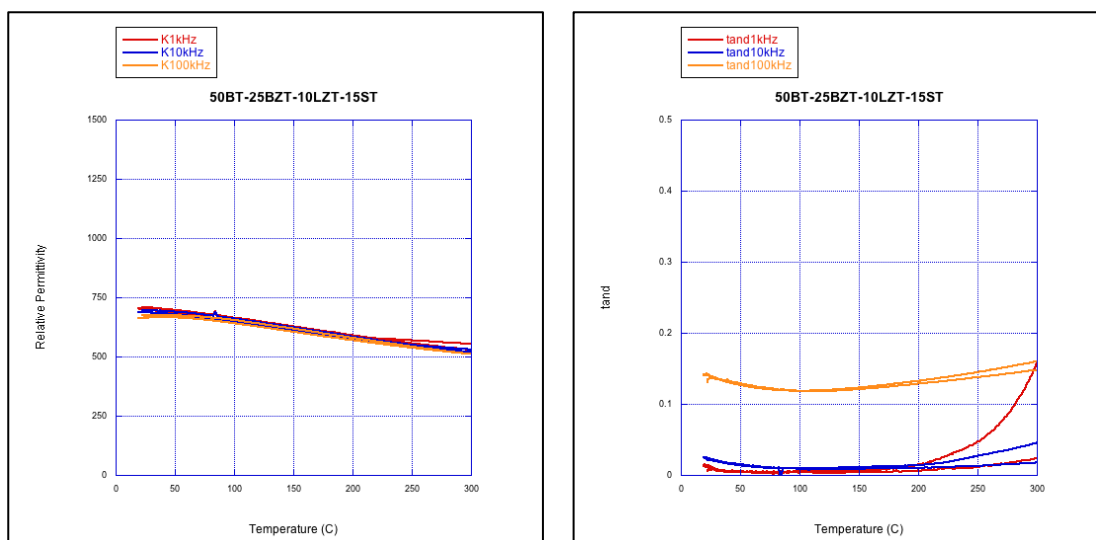


Figure 85: (a) High temperature relative permittivity measurements of 50BT-25BZT-10LZT-15ST and (b) dielectric loss versus high temperature measurements show a low $T\epsilon$ and acceptable loss values up to 100kHz.

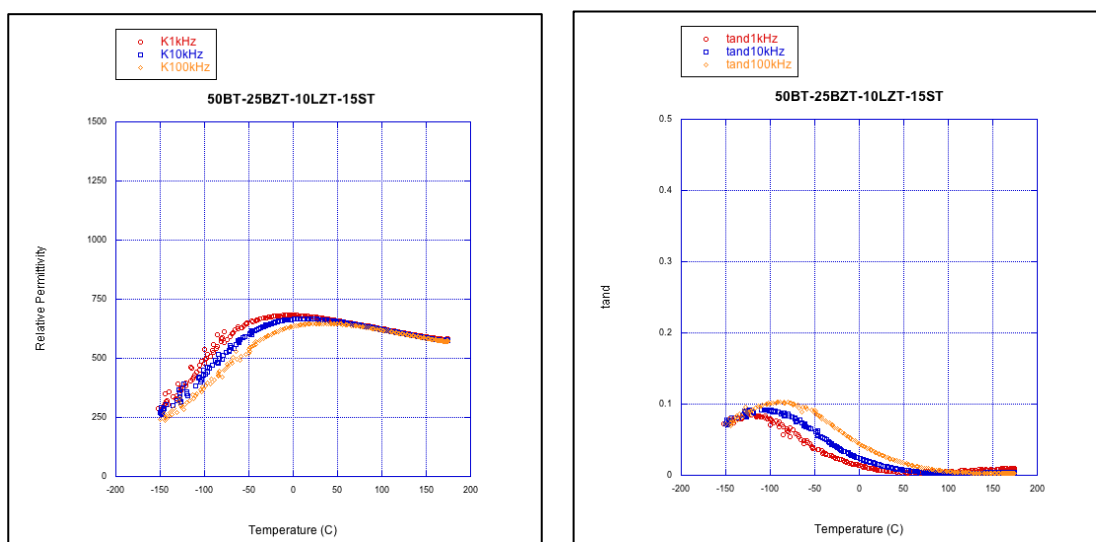


Figure 86: (a) The low temperature permittivity measurements of 50BT-25BZT-10LZT-15ST show a T_{max} right around 0°C while (b) shows low dielectric loss measurements from 0°C on.

Polarization versus electric field measurements along with the low temperature dielectric data confirm this material is a linear dielectric with a diffuse peak in permittivity which is indicative of relaxor dielectrics.

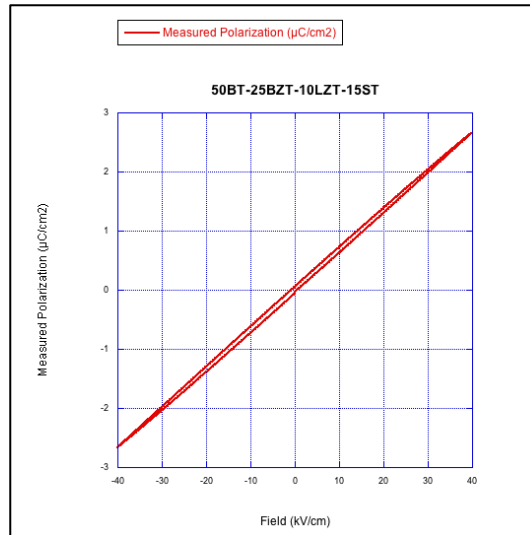


Figure 87: Polarization versus electric field measurements of 50BT-25BZT-10LZT-15ST show a linear dielectric that can withstand an electric field up to 40kV/cm.

Modification of the batch composition to include more LZT in place of ST was done to help create a more diffuse peak in permittivity with a $TC\epsilon$ that is closer to zero when compared to the previous composition. High and low temperature dielectric measurements confirm that this is the case with both the $TC\epsilon_{mid}$ and $TC\epsilon_{low}$ being reduced as seen in table 11. This modification also lowered the T_{max} below 0°C while simultaneously lowering the relative permittivity at T_{max} .

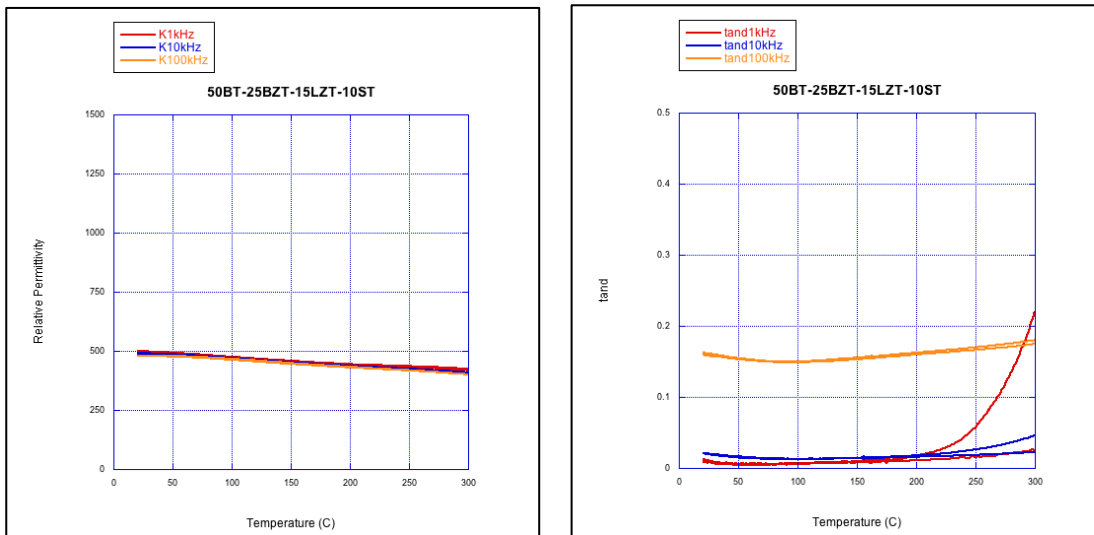


Figure 88: (a) The relative permittivity of 50BT-25BZT-15LZT-10ST shows an even lower $TC\epsilon$ at the sacrifice of a lower overall permittivity. (b) The dielectric loss remains very low under 100kHz and up to **200°C**.

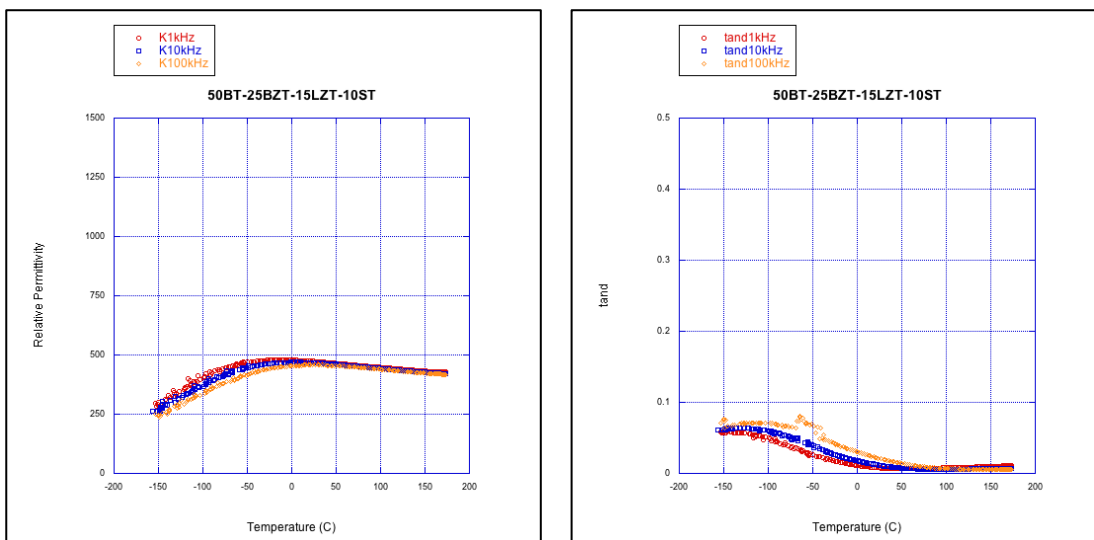


Figure 89: (a) The low temperature permittivity measurement of 50BT-25BZT-15LZT-10ST shows a T_{max} below **0°C** while (b) shows low dielectric loss values at all temperatures and frequencies.

Polarization versus electric field measurements once again show a linear dielectric with a slight deviation from total linearity which could be due to the material withstanding a higher electric field before shorting across the electrodes. The 50BT-

25BZT-15LZT-10ST composition also passes X7R specifications with only a 5% $\frac{\Delta C}{C_0}$ while still maintaining a relative permittivity above 400 for relevant temperatures.

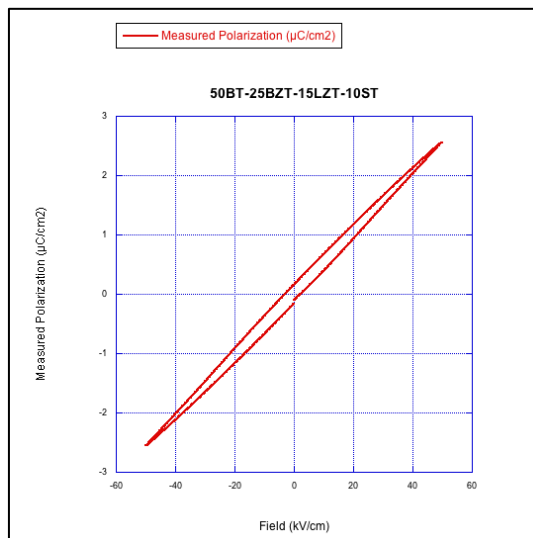


Figure 90: Polarization versus electric field for 50BT-25BZT-15LZT-10ST shows a linear dielectric with a dielectric strength of 50kV/cm.

Table 11: Dielectric Properties of the BT-BZT-LZT-ST system

Composition	TCE_{mid} (ppm/°C)	TCE_{low} (ppm/°C)	T_{max} (°C)	ϵ at T_{max}	X7R Capacitance Variation
50BT-25BZT-10LZT-15ST	-885	4547	12.6	666.9	11%
50BT-25BZT-15LZT-10ST	-601	3339	-1	469	5%

5. Discussion

Possible relaxor dielectric materials with a low temperature dependency are explored to find the material with the best combination of relative permittivity, low dielectric loss, and dielectric strength. The best materials that meet these specifications use the relaxor dielectric mechanism that creates a diffuse peak in relative permittivity. This mechanism operates off of creating a high level of disorder within the B site of a perovskite using ions of different size and valiancy. After finding an ideal synthesis route to create a single phase perovskite structure each material has its dielectric properties characterized with respect to temperature. Finally once the dielectric strength is measured trends can be observed across varying compositions to find the best material created in this work and hint towards future compositions which may lead to even better electronic properties.

The first system explored is $BaTiO_3 - Bi\left(Zn_{\frac{1}{2}}Ti_{\frac{1}{2}}\right)O_3 - SrTiO_3$ which proved difficult to create a single phase perovskite, possibly due to processing difficulties and maintaining batch stoichiometry. These compositions were synthesized into the perovskite structure and exhibited relative permittivity value's above 1000 but had a poor $TC\epsilon$ value and high dielectric loss across a wide range of temperatures. The BT-BZT-ST system also shows a temperature of maximum permittivity that is well above room temperature, meaning further research on this system should not be pursued without some type of compositional modification prepared to significantly reduce the T_{max} .

The next system explored was $BaTiO_3 - Bi\left(Zn_{\frac{1}{2}}Ti_{\frac{1}{2}}\right)O_3 - La\left(Mg_{\frac{1}{2}}Ti_{\frac{1}{2}}\right)O_3$, in which three basic compositions were synthesized to get a general idea of the compositional range in which a single phase perovskite could be achieved in the ternary system. The 25BT-50BZT-25LMT composition was the only one in this system where a single phase perovskite could not be achieved. Both other compositions show some of the lowest $TC\epsilon$ values measured in this work with the 25BT-25BZT-50LMT composition having a $TC\epsilon = -136^\circ\text{C}/\text{ppm}$ at 10kHz. These compositions also have a T_{max} that is well below 0°C which makes it a possibility for temperature stable capacitors. For the applications of this study the relative permittivity was too low and thus the focus shifted towards increasing the relative permittivity at all temperatures. While high dielectric loss was observed at the 100kHz frequency for the high temperature measurements, this was not the case when measuring samples using the low temperature environment which might indicate an issue with the measurement setup on the high temperature Probostat facilitating that to occur. Overall the $\tan\delta \approx 0.01$ for all temperature and frequencies up to around 200°C .

After observing the low $TC\epsilon$ associated with compositions with high levels of LMT some additional modifications were made to the most promising compositions done by McCue in previous work [26]. The constituent $La\left(Mg_{\frac{1}{2}}Ti_{\frac{1}{2}}\right)O_3$ was replaced with $La\left(Zn_{\frac{1}{2}}Ti_{\frac{1}{2}}\right)O_3$ to aid in the creation of single phase perovskites. The LZT was then substituted in small amounts to replace BZT in the BT-BZT-PNN system to try to

reduce the $TC\epsilon$ even closer to zero. The best composition resulting from this substitution appears to be 50BT-20BZT-5LZT-25PNN because it has a $TC\epsilon = -1575 \text{ }^\circ\text{C}/\text{ppm}$ and a $T_{max} = -28^\circ\text{C}$ and a $\epsilon_r = 838$. Overall the addition of LZT proved to be ineffective at significantly reducing the $TC\epsilon$ beyond the original BT-BZT-PNN compositions. Although many of the material in the BT-BZT-LZT-PNN system would still be effective X7R capacitors as seen in table 5.

When looking at the tolerance factor of BT-BZT-LZT-ABO₃ compositions it appears the same trend exists that was discovered by Raengthon et al. As the tolerance factor decreases the $TC\epsilon$ approached 0. This allows compositional modifications to be strategically engineered to specifically skew the $TC\epsilon$ towards $0 \text{ }^\circ\text{C}/\text{ppm}$.

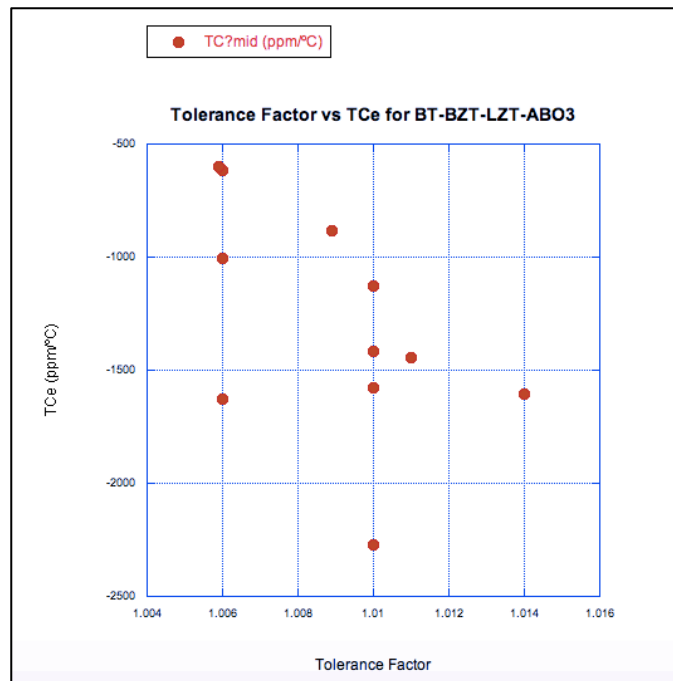


Figure 91 The relationship between the tolerance factor and $TC\epsilon$ for BT-BZT-LZT-ABO₃ compositions. The same trend observed in an earlier study where decreasing the tolerance factor can push the $TC\epsilon$ toward $0^{\circ}\text{C}/\text{ppm}$.

Compositions based around PT-PNN-BZT-NN had incredibly large $TC\epsilon$ and had a ferroelectric polarization versus electric field loops. After observing that this system would be unsuitable for linear dielectric applications the composition was modified to have lower levels of lead containing constituents and the system was reduced to PT-PNN-NN to help achieve a single phase cubic perovskite. While these modifications help to achieve a linear dielectric, all compositions within this system had high dielectric losses making them undesirable for nearly all applications.

The last system looked at was the BT-BZT-LZT-ST system which proved to have incredibly low $TC\epsilon$ while maintaining relative permittivity values around 500. Both compositions within this system can easily achieve X7R capacitor specifications and possess a T_{max} near 0°C . Polarization versus electric field measurements confirm a

linear dielectric material capable of withstanding fields up to 50 kv/cm for the 50BT-25BZT-15LZT-10ST composition. While the relative permittivity is not quite at the necessary level to meet the application requirements of this project, further investigation into this quaternary system could find the right balance of dielectric properties.

6. Future Work

The most successful compositions from this work are from the BT-BZT-LZT-ST family which had a maximum permittivity near 0°C a low $TC\epsilon$, low dielectric loss, and a relative permittivity around 500. Both compositions studied in this family meet X7R specifications but the electronic properties could be improved further if the temperature of maximum permittivity could be lowered below 0°C while simultaneously raising the maximum permittivity. Introducing small amounts of PNN could achieve the desired results although synthesis of a single phase perovskite with the level of cation disorder suggested might be difficult. Further exploration of the quaternary system BT-BZT-LZT-ST should also be pursued considering the success of the few compositions characterized in this work. Interesting compositions to look into could be 55BT-20BZT-15LZT-10ST, or 60BT-17.5BZT-10LZT-12.5ST with the goal being to raise the permittivity while keeping other parameters constant.

The BT-BZT-LZT-PNN system showed some promising results with the temperature of maximum permittivity well below 0°C relative permittivity's around 1000 and a $TC\epsilon \approx 1400$. Future work could explore more compositions with 20% PNN or lower with the goal being to introduce more LZT to reduce the $TC\epsilon$. Another compositional modification that should be attempted is to create a new quaternary system where LZT is replaced by ST to determine if one reduces the $TC\epsilon$ better than the other.

While other compositions characterized in this study proved to be far less successful, additional investigation into a $PT - PNN - ABO_3$ system could still be a viable

linear dielectric. If the levels of PT and PNN are kept low enough with another constituent such as LZT or ST present a low loss linear dielectric could be fabricated with a sufficiently low T_{max} and $TC\epsilon$.

Works Cited

- [1] Kaiser, Cletus J. *The Capacitor Handbook*. CJ Pub., 1995.
- [2] Moulson, A. J., and J. M. Herbert. *Electroceramics: Materials, Properties, Applications*. John Wiley & Sons, 2003.
- [3] Moulson, A. J., and J. M. Herbert. *Electroceramics: Materials, Properties, Applications*. John Wiley & Sons, 2003.
- [4] West, Anthony R. *Basic Solid State Chemistry*. John Wiley & Sons, 1999.
- [5] Bhalla, A. S., R. Guo, and R. Roy. “The Perovskite Structure – a Review of Its Role in Ceramic Science and Technology.” *Material Research Innovations* 4, no. 1 (November 1, 2000): 3–26. <https://doi.org/10.1007/s100190000062>.
- [6] “Ab Initio Investigation of Hybrid Organic-Inorganic Perovskites Based on Tin Halides.” ResearchGate. Accessed April 16, 2018. https://www.researchgate.net/publication/224274090_Ab_initio_investigation_of_hybrid_organic-inorganic_perovskites_based_on_tin_halides.
- [7] Raengthon, Natthaphon, Connor McCue, and David P. Cann. “Relationship between Tolerance Factor and Temperature Coefficient of Permittivity of Temperature-Stable High Permittivity BaTiO₃–Bi(Me)O₃ Compounds.” *Journal of Advanced Dielectrics* 6, no. 1 (February 18, 2016): 1650002. <https://doi.org/10.1142/S2010135X16500028>.
- [8] Damjanovic, Dragan. “Ferroelectric, Dielectric and Piezoelectric Properties of Ferroelectric Thin Films and Ceramics.” *Reports on Progress in Physics* 61, no. 9 (1998): 1267. <https://doi.org/10.1088/0034-4885/61/9/002>.
- [9] Sakayori, Ken-ichi, Yasunori Matsui, Hiroyuki Abe, Eiji Nakamura, Mikihiko Kenmoku, Tomoyuki Hara, Daisuke Ishikawa, Akihiro Kokubu, Ken-ichi Hirota, and Takuro Ikeda. “Curie Temperature of BaTiO₃.” *Japanese Journal of Applied Physics* 34, no. 9S (September 1995): 5443. <https://doi.org/10.1143/JJAP.34.5443>.
- [10] Robinson, D. A., S. B. Jones, J. M. Wraith, D. Or, and S. P. Friedman. “A Review of Advances in Dielectric and Electrical Conductivity Measurement in Soils Using Time Domain Reflectometry.” *Vadose Zone Journal* 2, no. 4 (November 1, 2003): 444–75. <https://doi.org/10.2136/vzj2003.4440>.
- [11] Jin Li, Li Fei, Zhang Shujun, and Green D. J. “Decoding the Fingerprint of Ferroelectric Loops: Comprehension of the Material Properties and Structures.” *Journal of the American Ceramic Society* 97, no. 1 (January 3, 2014): 1–27. <https://doi.org/10.1111/jace.12773>.

- [12] Cockbain, A. G., and P. J. Harrop. "The Temperature Coefficient of Capacitance." *Journal of Physics D: Applied Physics* 1, no. 9 (1968): 1109. <https://doi.org/10.1088/0022-3727/1/9/302>.
- [13] Harrop, P. J. "Temperature Coefficients of Capacitance of Solids." *Journal of Materials Science* 4, no. 4 (April 1, 1969): 370–74. <https://doi.org/10.1007/BF00550407>.
- [14] Bosman, A. J., and E. E. Havinga. "Temperature Dependence of Dielectric Constants of Cubic Ionic Compounds." *Physical Review* 129, no. 4 (February 15, 1963): 1593–1600. <https://doi.org/10.1103/PhysRev.129.1593>.
- [15] Sands, Donald E. *Introduction to Crystallography*. Courier Corporation, 1969.
- [16] Acosta, Matias. *Strain Mechanisms in Lead-Free Ferroelectrics for Actuators*. Springer, 2016.
- [17] "Dielectric Ceramics: Basic Principles, Mechanisms of Polarization." *National Programme on Technology Enhanced Learning* (blog), n.d. http://nptel.ac.in/courses/113104005/lecture18a/18_2.htm.
- [18] Herbert, J. M. *Ceramic Dielectrics and Capacitors*. CRC Press, 1985.
- [19] Bokov, A. A., and Z.-G. Ye. "Recent Progress in Relaxor Ferroelectrics with Perovskite Structure." *Journal of Materials Science* 41, no. 1 (January 2006): 31–52. <https://doi.org/10.1007/s10853-005-5915-7>.
- [20] Prosandeev, S. A., S. B. Vakhrushev, N. M. Okuneva, P. A. Markovin, I. P. Raevski, I. N. Zaharchenko, and M. S. Prosandeeva. "The Significance of the Burns Temperature in Relaxor PMN." *arXiv:cond-Mat/0506132*, June 6, 2005. <http://arxiv.org/abs/cond-mat/0506132>.
- [21] Raengthon, Natthaphon. "Development of complex perovskite dielectric ceramics for high temperature capacitor applications," n.d.
- [22] Cann, David P., Natthaphon Raengthon, Narit Triamnak, Harlan Brown-Shaklee, Ian M. Reaney, and Geoff Brennecke. "BaTiO₃-Bi(Zn_{1/2}Ti_{1/2})O₃ Relaxors for Advanced Capacitor Applications," n.d.
- [23] "Here's What Make MLCC Dielectrics Different | KEMET." Engineering Center, December 14, 2015. <https://ec.kemet.com/mlcc-dielectric-differences>.
- [24] Marinel, S., M. Pollet, and G. Desgardin. "Sintering of CaZrO₃-Based Ceramic Using Mixed Conventional and Microwave Heating." *Journal of Materials Science: Materials in Electronics* 13, no. 3 (March 1, 2002): 149–55. <https://doi.org/10.1023/A:1014381300373>.

- [25] Triamnak, Narit, Rattikorn Yimnirun, Jan Pokorny, and David P. Cann. "Relaxor Characteristics of the Phase Transformation in $(1 - x)\text{BaTiO}_3 - x\text{Bi}(\text{Zn}_{1/2}\text{Ti}_{1/2})\text{O}_3$ Perovskite Ceramics." *Journal of the American Ceramic Society* 96, no. 10 (October 1, 2013): 3176–82. <https://doi.org/10.1111/jace.12495>.
- [26] McCue, Connor. "Development of Temperature-Stable Relaxor Dielectrics for High Energy Density Capacitor Applications," n.d.
- [27] Alberta, Edward F., and Amar S. Bhalla. "Low-Temperature Properties of Lead Nickel-Niobate Ceramics." *Materials Letters* 54, no. 1 (May 1, 2002): 47–54. [https://doi.org/10.1016/S0167-577X\(01\)00538-9](https://doi.org/10.1016/S0167-577X(01)00538-9).
- [28] Suryanarayana, C., and M. Grant Norton. *X-Ray Diffraction: A Practical Approach*. Springer Science & Business Media, 1998.
- [29] Campos, M.F. De., Damasceno, Jailton. Machado R. Achete, C. "Uncertainty Estimation of Lattice Parameters Measured by X-Ray Diffraction." ResearchGate. Accessed June 15, 2018. https://www.researchgate.net/publication/242284045_Uncertainty_estimation_of_lattice_parameters_measured_by_X-Ray_diffraction.
- [30] Salak, A. N., V. V. Shvartsman, M. P. Seabra, A. L. Kholkin, and V. M. Ferreira. "Ferroelectric-to-Relaxor Transition Behaviour of BaTiO_3 Ceramics Doped with $\text{La}(\text{Mg}_{1/2}\text{Ti}_{1/2})\text{O}_3$." *Journal of Physics: Condensed Matter* 16, no. 16 (2004): 2785. <https://doi.org/10.1088/0953-8984/16/16/003>.
- [31] Lei, Chao, Kepi Chen, Xiaowen Zhang, and Jun Wang. "Study of the Structure and Dielectric Relaxation Behavior of $\text{Pb}(\text{Ni}_{1/3}\text{Nb}_{2/3}) - \text{PbTiO}_3$ Ferroelectric Ceramics." *Solid State Communications* 123, no. 10 (August 1, 2002): 445–50. [https://doi.org/10.1016/S0038-1098\(02\)00371-X](https://doi.org/10.1016/S0038-1098(02)00371-X).
- [32] Prasatkhetragarn, A., R. Saenarpa, B. Yotburut, P. Ketsuwan, T. Sareein, S. Ananta, and R. Yimnirun. "Investigations on Morphology and Ferroelectric Properties of $\text{NaNbO}_3 - \text{PbTiO}_3$ Composite Ceramics." *Ferroelectrics* 416, no. 1 (January 1, 2011): 40–46. <https://doi.org/10.1080/00150193.2011.577664>.

Appendix A

